The Pennsylvania State University

The Graduate School

Department of Industrial Engineering

MATHEMATICAL AND COMPUTATIONAL MODELS FOR NANOSTRUCTURED COATING USING ELECTRON BEAM PHYSICAL VAPOR DEPOSITION (EB-PVD)

A Thesis in

Industrial Engineering

by

Seungyup Baek

© 2007 Seungyup Baek

Submitted in Partial Fulfillment
of the Requirements
for the Degree of

Doctor of Philosophy

May 2007

The thesis of Seungyup Baek has been reviewed and approved* by the following:

Vittaldas V. Prabhu
Associate Professor of Industrial Engineering
Thesis Advisor
Chair of Committee

Richard A. Wysk
Professor of Industrial Engineering
Leonhard Chair in Engineering

Robert C. Voigt
Professor of Industrial Engineering

Jogender Singh
Chief Scientist, Applied Research Lab
Professor of Materials Science and Engineering

Richard J. Koubek
Professor of Industrial Engineering
Head of the Harold and Inge Marcus Department of
Industrial and Manufacturing Engineering

*Signatures are on file in the Graduate School

ABSTRACT

Nanostructured coatings offer substantial improvement over conventional coatings in physical and mechanical properties such as hardness, strength, toughness and thermal conductivity. There are numerous applications where nanostructured coatings have been found to beneficial including bio-mechanical implants, semiconductor thin films, propulsion, and power generation. In aircraft and power generation turbines, nanostructured thermal barrier coating (TBC) can significantly reduce fuel costs. There has been an acute need for a science base, such as dynamic models of nanostructured coating processes. Modeling the processes presents significant challenges because the physical variables are highly coupled and interact in a nonlinear manner. Real-time control of this process poses additional challenges because of the high vacuum, high temperature, and generally hostile environment for making in-situ measurements, which further motivates the need for good process models.

This research proposes unified models for controlling nanostructured coating process using electron beam physical vapor deposition (EB-PVD). Specifically, the following three dynamical models have been developed:

1. ***Machine Dynamics Model*** – combines models of various component dynamics in the EB-PVD machine such as cathode heating, ingot melting, and evaporation.
2. ***Deposition Process Model*** – mathematically characterizes the physical relationship between process parameters and the micro/nanostructure of the coating.

3. ***Substrate Kinematics Model –*** geometric models that are computationally efficient for modeling the kinematics of substrate and manipulator motion.

One of the main contributions of this work is the use of partial differential equations for the deposition process model to characterize the evolution of the coated surface. This has been used to characterize surface evolution at the macro-level (1 micrometer), at the meso-level (50 nanometers), and with limited fidelity at the nano-level (1 nanometer). The underlying partial differential equations have been solved using numerical techniques on a cluster of computers, and solutions have been found to agree well with experimental results published by independent researchers.

A multi-criteria technique has also been developed to determine EB-PVD parameters by solving a optimization problem including four criteria: production cost, process efficiency, coating uniformity, and coating life-time. The technique combines a fuzzy-logic approach with a continuous variable control approach to enable interactive optimization. A simplified model of the EB-PVD process has been developed to relate current input to the EB gun to the coating thickness. This model has been used to design and simulate a real-time PID controller. Simulation results indicate that the controller performs well in terms of disturbance-rejection in input power. The controller requires real-time feedback from quartz-crystal microbalance sensors, which makes it practically feasible and serve as a basis for spatial composition control.

Anticipated benefits of this research are the development of a science base for controlling nanostructured coating processes using the EB-PVD through reduced-order mathematical models and efficient computational models. This can be expected to lead to systematically engineered processes with high repeatability and low variance instead of the current “trial and error/recipe-based methods” used in industry. This can be expected to have a significant short-term and long-term impact in several vertical industry sectors including energy, transportation, medical, and semi-conductor.

TABLE OF CONTENTS

LIST OF FIGURES..viii

LIST OF TABLES xii

ACKNOWLEDGEMENTS xiv

Chapter 1 Introduction 1

1.1. Nanostructured coating process using EB-PVD 2
1.2. Modeling of the EB-PVD process 4
1.3. Process parameter selection by solving multiobjective optimization problem 7
1.4. Real-time control of deposition process...11
1.5. Issues addressed in this research...16
1.6. Thesis organization 20

Chapter 2 Finite element model for unified EB-PVD machine dynamics.................23

2.1. Unified model of EB-PVD process..24
2.1.1. Machine dynamic model..26
2.1.1.1. EB gun model 26
2.1.1.2. Ingot heating/melting model...28
2.1.1.3. Evaporation..35
2.1.2 Deposition process model..37
2.2. Unified dynamics computational model 39
2.3. Experiments and Test results 42
2.3.1. Cylinder rod coated with tungsten..47
2.3.2. Flat plate coated with titanium...49
2.4. Summary 52

Chapter 3 Discrete state space model for substrate motion in EB-PVD process........53

3.1. Structure of EB-PVD process 54
3.1.1. Machine dynamics model 56
3.1.2. Deposition process model...59
3.1.3. Substrate kinematics model 60
3.2. Process simulation...68
3.3. Case study 72
3.3.1. One-axis Holder...79
3.3.2. Two-axis Holder 84
3.4. Summary 90

Chapter 4 Simulation of nanostructured coating in EB-PVD using level set approach 92

4.1. Level set method 93
4.2. Speed function F of EB-PVD process 95
4.3. Numerical scheme for level set equation 96
4.4. Simulation and Results 99
4.5. Summary 119

Chapter 5 Parameter selection by solving multiobjective optimization problem 121

5.1 Problem formulation 122
5.2. Heuristic for searching the set of weight factors 124
5.3. New algorithm 128
5.4. Optimization problem formulation for EB-PVD process 131
5.4.1 Production cost 133
5.4.2. Uniformity of coating thickness 135
5.4.3. Collection efficiency of material on substrate 136
5.4.4. Coating lifetime 137
5.4.5. Multi-criteria problem formulation 138
5.5. Case study for Pareto optimal solution of TBC design 141
5.6. Summary 147

Chapter 6 Simulation-based design of EB-PVD process controller 149

6.1. Development of feedback controller 149
6.1.1. Selection of system output and control parameter 150
6.1.2. Process modeling 152
6.1.3. Open-loop response to the change and disturbance of manipulated variable 154
6.1.4. Design of feedback controller 155
6.2. Implementation of spatially distributed QCM sensors 158
6.3. Summary 160

Chapter 7 Conclusion 161

7.1. Summary of conclusions 162
7.2. Future work 163

Bibliography 166

LIST OF FIGURES

Figure 1.1. The relationship between process parameters, properties of coating, and functions of coating 10

Figure 1.2. Schematic diagram of EB-PVD system 17

Figure 1.3. Intelligent processing of EB-PVD 19

Figure 2.1. Schematic block diagram of EB-PVD process 25

Figure 2.2. Example of EB scan pattern 28

Figure 2.3. Example of s_{ij} when n_{mesh} = 10 30

Figure 2.4. The distribution of EB power with the impingement of EB on (i, j) element 31

Figure 2.5. Geometrical relation between vapor source and surface element 37

Figure 2.6. Organization for unified dynamic computational model, where H/M* is the acronym of heating and melting and [·] means the number of a related equation 40

Figure 2.7. The experimental arrangement for a) cylinder rod and b) a disk-shaped plate 43

Figure 2.8. The screenshots of the developed computational models in Matlab 47

Figure 2.9. The coating thicknesses along the longitudinal direction of the cylinder rod against divergence angle (ψ) as time increases from 0.2sec to 20.2sec with the time interval of 2sec 48

Figure 2.10. Ratio of coating thickness: a) in two divergence angle, b) along A-A section 51

Figure 2.11. Coating thickness along A-A section in the flat plate as time increases 52

Figure 3.1. Decomposition of EB-PVD process that consists of three sub processes 54

Figure 3.2. The architecture of EB-PVD process model 55

Figure 3.3. The change of spatial vector by kinematics and deposition 61

Figure 3.4. The flowchart of the EB-PVD computational model 70

Figure 3.5. The turbine blade 72

Figure 3.6. The digitization of the turbine 72

Figure 3.7. Schematic drawing of two substrate holders with their link system: a) One-axis Holder, b) Two-axis Holder..73

Figure 3.8. The screenshot of the simulator using Matlab 79

Figure 3.9. Main effect plots for a) $M(t_{sim})$, b) $v(t_{sim})$, c) $d_{min}(t_{sim})$ in One-axis Holder...80

Figure 3.10. Interaction plot for a) $M(t_{sim})$, b) $v(t_{sim})$, c) $d_{min}(t_{sim})$ in One-axis Holder...82

Figure 3.11. Main effect plots for a) $M(t_{sim})$, b) $v(t_{sim})$, c) $d_{min}(t_{sim})$ in Two-axis Holder...85

Figure 3.12. Interaction plot for $M(t_{sim})$ in Two-axis Holder. 89

Figure 3.13. Interaction plot for $v(t_{sim})$ in Two-axis Holder.......................................89

Figure 3.14. Interaction plot for $d_{min}(t_{sim})$ in Two-axis Holder. 90

Figure 4.1. Flow chart of the EB-PVD simulator implementing the level set method...100

Figure 4.2. Experimental arrangement...102

Figure 4.3. The screenshot of simulation model in Matlab..104

Figure 4.4. Simulation results under various rotation speeds with Δ = 1μm and without the change of rotation direction: a) and b) with 1rpm, c) and d) with 5rpm, e) and f) with 20rpm 106

Figure 4.5. Simulation results under various rotation speeds with Δ = 1μm and the change of rotation direction at 180°: a) and b) with 1rpm, c) and d) with 5rpm, e) and f) with 20rpm 107

Figure 4.6. Experimental results under various rotation speeds (Yamaguchi et al., 2003) 108

Figure 4.7. Bent columns under the rotation speed of 1 rpm (Yamaguchi et al., 2003) 108

Figure 4.8. Bent columns under the rotation speed of 1 rpm (Yamaguchi et al., 2003) 109

Figure 4.9. Time marks with $\Delta = 1\mu m$, 1rpm, and no change of rotation direction 110

Figure 4.10. Time marks at the same with $\Delta = 1\mu m$, 1rpm, and the change of rotation direction at 180° 111

Figure 4.11. Simulation results under various rotation speeds with Δ = 100nm and without the change of rotation direction: a) and b) with 1rpm, c) and d) with 5rpm, e) and f) with 20rpm 113

Figure 4.12. Simulation results under various rotation speeds with Δ = 100nm and the change of rotation direction at 180°: a) and b) with 1rpm, c) and d) with 5rpm, e) and f) with 20rpm 114

Figure 4.13. Simulation results under various rotation speeds with Δ = 50nm and without the change of rotation direction: a) and b) with 1rpm, c) and d) with 5rpm, e) and f) with 20rpm 116

Figure 4.14. Simulation results under various rotation speeds with Δ = 50nm and the change of rotation direction at 180°: a) and b) with 1rpm, c) and d) with 5rpm, e) and f) with 20rpm 117

Figure 4.15. Helical columnar shape from experiment in the low rotation speed (Hawkeye and Brett, 2005) 118

Figure 4.16. Helical columnar shape from simulation in the low rotation speed 119

Figure 5.1. "Closed-loop" structure of the proposed heuristic 127

Figure 5.2. Flowchart for the proposed algorithm 131

Figure 5.3. The results from numerical example of the proposed algorithm 145

Figure 6.1. Block diagram for closed-loop process control 150

Figure 6.2. Step response of first-order process with integration: a) t = 200s, b) t = 1000s 153

Figure 6.3. Response of thickness of coating with respect to step change in input current 155

Figure 6.4. Response of thickness of coating with respect to step disturbance in the three variables of the EB-gun, A, V, and U_B 155

Figure 6.5. A reference trajectory with the thickness set-point of 0.0656mm at t=600s....156

Figure 6.6. Thickness of coating with the thickness set point of 0.0656mm at 600s ..158

Figure 6.7. Schematic description of calculation of the deposition thickness ds_i........159

LIST OF TABLES

Table 2.1. The themophysical properties of titanium and tungsten 45

Table 2.2. Parameters used in the simulation..46

Table 2.3. Machine parameters and time step used in the simulation.........................46

Table 2.4. Comparison of experiment and simulation for a cylinder rod coated with W..48

Table 2.5. Comparison of experiment and simulation for a flat plate coated with Ti 51

Table 3.1. Constant kinematics parameters..74

Table 3.2. Factors and levels for the experimental design..76

Table 3.3. Parameters used in the simulation of YSZ deposition on turbine blade 77

Table 3.4. Analysis of Variance for reduced model of $M(t_{sim})$...................................83

Table 3.5. Analysis of Variance for reduced model of $v(t_{sim})$ 83

Table 3.6. Analysis of Variance for reduced model of $d_{min}(t_{sim})$ 83

Table 3.7. Analysis of Variance for reduced model of $M(t_{sim})$...................................87

Table 3. 8. Analysis of Variance for reduced model of $v(t_{sim})$ 87

Table 3.9. Analysis of Variance for reduced model of $d_{min}(t_{sim})$ 88

Table 4.1. Parameters used in the simulation...103

Table 4.2. Comparison of experiment and simulation for a plate coated with YSZ....110

Table 5.1. Variables of EB-PVD process...132

Table 5.2. Constants for optimization problem of EB-PVD.......................................132

Table 5.3. Approximated linear functions..142

Table 5.4. Conditions of EB-PVD process for the case study of TBC made of YSZ 142

Table 5.5. Limitations of the variables of EB-PVD process.......................................142

Table 5.6. Membership functions selected for the experiment 144

Table 5.7. Best value with respect to interview with DMs 145

Table 5.8. Value of variables for the best value of objective functions.......................147

ACKNOWLEDGEMENTS

I am sincerely appreciative of the help of my committee members, Dr. Richard Wysk, Dr. Robert Voigt, and Dr. Jogender Singh. Above all, I wish to particularly thank my advisor, Dr. Vittaldas Prabhu for his indefatigable encouragement and unfailing support. His technical and intellectual ingenuity contributed prominently to all aspects of this work. I have really, really enjoyed working with him for last three years.

I would also like to give my special thanks to Dr. Hyung-Sang Hahn for the encouragement of pursuing Ph.D. degree in Industrial Engineering in USA. Dr. Hu-Chul Lee and Dr. Sang-Do Noh are gratefully acknowledged for their supporting me in Ph.D. study.

I would like to express my gratitude to my friends and collegues, Michel, Changsu Ok, Dr. Cheol Lee, Yongma Moon, Vamsi, and Nazrul, for helping me finally get here today.

I wish to especially thank my family for their love and support. My elder sister Mi-Jeong, my brother Seung-Seok, and my parents, Ho-Young Baek and Jeong-Ja Hwang, offered unceasing encouragement, consolation, and every kind of assistance. I also have to thank my parents-in-law, Hyung-Seop Shim and Dong-Shim Go, for their constant and never ending support.

Last but certainly not least, I have to heartily thank my wonderful wife, D.D.S. Hyun-Sook Shim for all of the sacrifices that she has made. It is not possible to describe all that she did to make this work possible. Now, it is my turn to support her and our unborn baby, San.

Chapter 1

Introduction

Nanostructured coatings have received a lot of attention in recent years because they offer potential for significant improvements in physical and mechanical properties such as hardness, strength, toughness and thermal conductivity over conventional coarse counterparts, provided by the manipulation of the ultra fine microstructure (Gleiter 1992; Gell 1995a; Suryanarayana 1995). According to Yoshida (2004), the accurate control of structures such as nano-interface, nano-pores, and nano-particles is the key to nanostructured coating technology. Electron beam physical vapor deposition (EB-PVD) has high potential at nano- as well as macro-structured coating fabrication (Singh and Wolfe 2005). The highly coupled, physical variables in this process, however, interact in a nonlinear manner, which has been challenge in modeling this process. The real-time control of the deposition process encounters additional challenges because of the high vacuum, high temperature, and generally hostile environment for making in-situ measurements.

There are numerous applications where nanostructured coatings have been found to be beneficial. In aircraft and power generation turbines, nanostructured thermal barrier coating (TBC) can significantly reduce costs. Nanocomposite thin films such as optically selective absorber coatings in thermal solar collectors can improve the efficiency and viability of alternative energy sources. Nanostructured TiO_2 films have been found to be beneficial in bone implants by improving the osseointegration of implant materials. There

has been an acute need for developing a science base for nanostructured coating processes, especially models and techniques for their real-time control (NRC 1996).

1.1. Nanostructured coating process using EB-PVD

Nanostructured coatings offer substantial improvement over conventional coatings in physical and mechanical properties such as hardness, strength, toughness and thermal conductivity (Gleiter 1992; Gell 1995a; Suryanarayana 1995). The concept of nanostructured coatings has changed even the overall direction of the research and development of coatings (Chung and Sproul 2003). For example, one is deposition of super-hard cubic boron nitride (c-BN), which has proven very difficult to deposit at thicknesses exceeding 0.1μm. Another is new nanometer-scale multilayered (or nanolaminate) and/or nanocomposite coatings that exhibit excellent hardness properties and other high-performance characteristics. In the nanocomposite, small hard nanocrystallites are embedded in an amorphous, metallic matrix resulting in unusual mechanical and structural properties, such us superhardness, enhanced elasticity, and thermal stability (Wolfe 2001; Carvalho et al. 2003).

Among various deposition techniques, electron beam physical deposition (EB-PVD) has shown versatile applications to nanostructured coatings. The reason is that it can simultaneously evaporate multiple materials of different composition (Matsumoto et al. 2004; Singh and Wolfe 2005). The advantage enables engineers to design tailored microstructures, such as functionally graded coatings and nano-laminated coatings, and new materials that could not be produced economically by conventional methods.

Coatings produced by the EB-PVD process usually have a good surface finish and a uniform microstructure. This process readily evaporates even elements with low vapor pressure such as molybdenum, tungsten, rhenium, and carbon. EB-PVD can lay down a variety of metallic and ceramic coating (oxides, carbides, nitrides) at relatively low temperatures. These include oxides of aluminum, yttrium, and zirconium, all of which are used in heavy industry and in microelectronics for insulation buffering and diffusion barriers (Singh and Wolfe 2005). Singh and Wolfe (2003) investigated the application of EB-PVD to the forming of net-shaped rhenium components with the shapes of ball, plate, and tube. EB-PVD successfully showed its cost-effectiveness to manufacture submicron and nano-size microstructure with high hardness and strength as compared with chemical vapor deposition (CVD).

In the EB-PVD process, focused high-energy electron beams are directed to melt and evaporate ingots of the metals or ceramics that will make up the coatings and preheat the target substrate in the vacuum chamber. The vapor from the melted coating materials fills the chamber and condenses on any object in the chamber, thereby covering it. The process takes place at moderate temperatures from 200°C to 1000°C with rapid deposition rates in the range of 100 to 150 micrometers of coating per minute at an ingot evaporation rate of about 10 to 15 kilograms per hour (Singh 1996). Since EB-PVD is primarily a line-of-sight process, uniform coating of complex parts such as turbine airfoils is accomplished by continuous rotation in the vapor cloud during the deposition process (Singh and Wolfe 2005).

TBC with nanostructured components has been explored in recent years in Japan using the EB-PVD (Yamaguchi et al. 2003; Matsumoto, Yamaguchi and Matsubara

2004; Jang et al. 2005; Jang and Matsubara 2005). Yamaguchi et al. (2003) showed the relationship between processing parameters of EB-PVD and the microstructures and textures of partially yttria-stabilized zirconia (YSZ) layers in TBC. Matsumoto et al. (2004) investigated the effects of the small amount of a dopant on the thermal conductivity of TBC coatings while maintaining the high resistance to sintering during deposition. In the multilayered YSZ film, total porosity increases as layer-interface pores increase, resulting in the increase of the phonon scattering and the decrease of thermal conductivity and diffusivity (Jang, Yoshiya and Matsubara 2005). With the YSZ coating, the rotation speed of the substrate showed the correlation with the total porosity and numbers of nano pores of the coating layers (Jang and Matsubara 2005). The basic technology for nanostructure control of ceramic coatings applied to metals was pursued to find novel functions (Yoshida 2004). The effects of various process parameters of the EB-PVD process on the microstructure of YSZ have been investigated (Schulz et al. 1997; Schulz et al. 2002; Schulz et al. 2003). According to them, the process parameters including the substrate rotation speed strongly influenced the microstructures of TBC.

1.2. Modeling of the EB-PVD process

There has been an acute need for developing a science base for nanostructured coating processes, especially models and techniques for their real-time process control (NRC 1996). Theory of evaporation was first established by Hertz in 1882 followed by Langmuir in 1913 and Knudsen in 1915 to model the evaporation rates from free solid surfaces and liquids (Glang 1970). One of the key results in theory of evaporation is the

cosine law of emission which models the directionality of evaporating molecules (Glang 1970). The cosine model and its variants have been used in several evaporation applications to model coating thickness of simple planar substrates (Graper 1973; Pulker 1984).

The kinetics of evaporation and vapor transport as well as deposition rate were simplified in reduced order models, and a macroscopic balance was established between the intermediate process parameters such as ingot temperature and deposition rate and the input parameters like EB and over-source heater power input (Azad 1998). Nastac et al. (2004) employed a computational fluid dynamics (CFD) method to investigate an EB-PVD ceramic-metal coating process. Fuke et al. (2005) extended the deposition model by Schiller et al. (1982) and presented a computational model using finite element method (FEM) to predict coating thickness on complex substrate. Junker et al. (2004) proposed the dynamic model of the deposition process. The model included the shifting mechanism of a substrate, which significantly affects the microstructure and the thickness of a coating in the EB-PVD process. The temperature profile of melt pool produced by EB has been studied for various processes such as welding, deposition, and surface treatment (Dave et al. 1995; Simon and Pal 1999; Qin et al. 2003). Powell et al. (2001) applied Monte Carlo (MC) to compute the vapor flux distribution and showed the effect of vapor source dimension and mean free path of a vapor particle on the power of cosine law n.

Since EB-PVD is primarily a line-of-sight process, the uniform coating of complex parts such as turbine airfoils is accomplished by continuous rotation in the vapor cloud during the deposition process (Schulz, Terry and Levi 2003; Yamaguchi, Wada, Kimura and Matsubara 2003; Singh and Wolfe 2005). Due to the rotation of a part, vapor

incidence angle changes. Consequently, micro/macro shadowing phenomena and in turn, the microstructure of the EB-PVD coating are highly influenced by the variation in the vapor incidence angle (Terry 2001; Yamaguchi, Wada, Kimura and Matsubara 2003). Controlling the coating thickness is of paramount importance, particularly in TiC coating for cutting tools and TBC for turbine blades because over-coating can reduce component life (Bose and DeMasi-Marcin 1997). This can be achieved either by using an automatic control system to control orientation and rotation or by using complex fixturing (Halnan and Lee 1983; Rigney et al. 1997). Although it needs trial-and-error procedures and requires high cost to successfully design the fixturing and to select kinematics parameters, little attention has been given to the development of a computationally efficient model for simulating substrate motion based on the various fixturing and kinematics parameters.

Thin film growth includes three microstructure processes: molecule adsorption, surface migration, and desorption (Maissel and Glang 1970). The three processes, however, can not be modeled using the continuum models for the EB-PVD process, such as the theory of evaporation and the energy balance equation, that are established based on the kinematics or thermophysics of mapping of infinitesimal points. For atomic scale simulation, many studies have relied on the MC technique. This method is well known to describe discrete atoms and their interactions in these microscopic processes without high-dimensional and nonlinear mathematical-models. It can also represent nanometer-scale phenomena on the surface of a substrate (Hass 2000; Gallivan and Murray 2004). While the MC can directly account for the stochastic nature of an individual atom to describe nanometer-scale dynamics, MC models are not available in closed-form so that it is very difficult to use them for system-level analysis. Thus, most researchers integrated

both machine level and micro level simulation to link process parameters and thin film deposition parameters using MC simulation approach (Coronell et al. 1998; Hass 2000; Gallivan and Murray 2004; Ni and Christofides 2005). Hansen et al. (2000) proposed a computationally highly-efficient and accurate method to model the growth of thin films, which . They linked the film growth rate obtained from molecular dynamics techniques in angstrom-scale to the morphology of growing film using a level set method that is a computationally efficient numerical technique for tracking interfaces and shapes (Osher and Sethian 1988). Adalsteinsson and Sethian (1995a; 1995b) extended the level set method to study the film growth and formulated a unified model of surface advancement including the effects of deposition, etching, and lithography. They applied a numerical technique developed for hyperbolic conservation laws to solve the level set formulation in the unified model.

1.3. Process parameter selection by solving multiobjective optimization problem

Decision making problems in highly complex system inevitably involve multiple decision makers (DMs) working in a distributed team structures as well as multiple objectives to be pursued. Multiple objective decision making (MODM) problems inherently have no superior solution which optimizes all the objective functions and only have efficient solutions for which improvement in any one objective is done at the expense of some other objectives. In real life, any DM can not precisely make decision for all objectives in an MODM problem; one DM may have biased preference to only a

part of the objectives because he/she can not fully understand the meaning and importance of other objectives managed by other DMs.

There have been various approaches to find the best compromise and satisfactory solution of the MODM problems. They can be categorized as follows: 1) approaches, like goal programming, that use pre-specified preferences of a DM, in which all the objectives are assigned to associated target values and a relative priority on achieving these levels (Arthur and Ravindran 1980; Ravindran et al. 1987), 2) approaches, like P_λ problem, that do not use any knowledge of DM's preference (Geoffrion 1967a; Geoffrion 1967b), 3) interactive approaches, like ZW method, that use progressively revealed preferences of a DM (Zionts and Wallenius 1976; Malakooti and Ravindran 1985). Every approach has advantages as well as disadvantage with respect to the others. For more details of those approaches, the authors refer to the comprehensive survey work by Shin and Ravindran (1991). In the interactive approaches which have shown good performance for solving the MODM problems (Shin and Ravindran 1991), a DM will be interactively interviewed until the best efficient solution is found. The DM, however, can not choose the solution with same criteria in every interview so that the decisions by the DM show inconsistency. This inconsistency will be more severe as the number of criteria increases. Interestingly, Malakooti and Ravindran (Malakooti and Ravindran 1985) proposed the formalization of the inconsistency of a DM. For the pairwise comparison and trade-off ratio between two objectives, which are main interaction styles to assess the preferences of a DM (Shin and Ravindran 1991), multiple DMs may have different preference, resulting into the inconsistency between DMs over the preference of objective functions. However, to our knowledge there is no published work for determining the best compromise or

satisfactory solution in this situation with multiple DMs and multiple objective functions. There has been another approach, based on the assumption that a DM has fuzzy or imprecise goals for each of the objective functions (Bellman and Zadeh 1970), which can be categorized by: fuzzy goal programming (Narasimhan 1980; Arenas Parra et al. 2001; Lin 2004) and interactive decision making in fuzzy environment (Sakawa et al. 1987; Mahapatra and Maiti 2005). In all studies of the fuzzy approach, the fuzzy goals for objective functions are assumed to be derived from the DM. By the fuzzy goals, the objectives are meant to be characterized as a fuzzy set in an appropriate space. One of the most crucial parts of the MODM problems is the identification of an appropriate utility function that well represents DM's unknown, imprecise preference. Effectively, an additive or weighted sum of the objective functions is assumed as the utility function of the DM (Geoffrion 1967a; Geoffrion 1967b; Zionts and Wallenius 1976).

Global competition in manufacturing makes it important to reduce the lead time from laboratory to market (Hill 1986). One of the key challenges for coating makers and engineers to shorten the lead time to market is to comprehensively understand the relationship between the microstructure and the properties of coating and EB-PVD process parameters. That is, the microstructure (MS) and properties (P) of coating, through the process design, relate to the process parameters (PP). The published work on the EB-PVD process has focused on the process parameters relating the machine dynamics and/or substrate kinematics. The research publications have, however, focused either on the mappings of (PP) → (MS) or on the mappings of (PP) → (P). For example, the process parameters or influence factors for TBC discussed by researchers are summarized in Fig. 1.1. (Wolfe et al. 1996; Schulz, Fritscher, Ratzer-Scheibe, Kaysser

and Peters 1997; Wolfe and Singh 1999; Bernier et al. 2002; Schulz, Munzer and Kaden 2002; Schulz, Terry and Levi 2003; Yamaguchi, Wada, Kimura and Matsubara 2003; Shi et al. 2004). Second approach is to find physical models to represent the dynamics of EB-PVD process (Azad 1998). With the models, he estimated the development of costing with respect to process parameters.

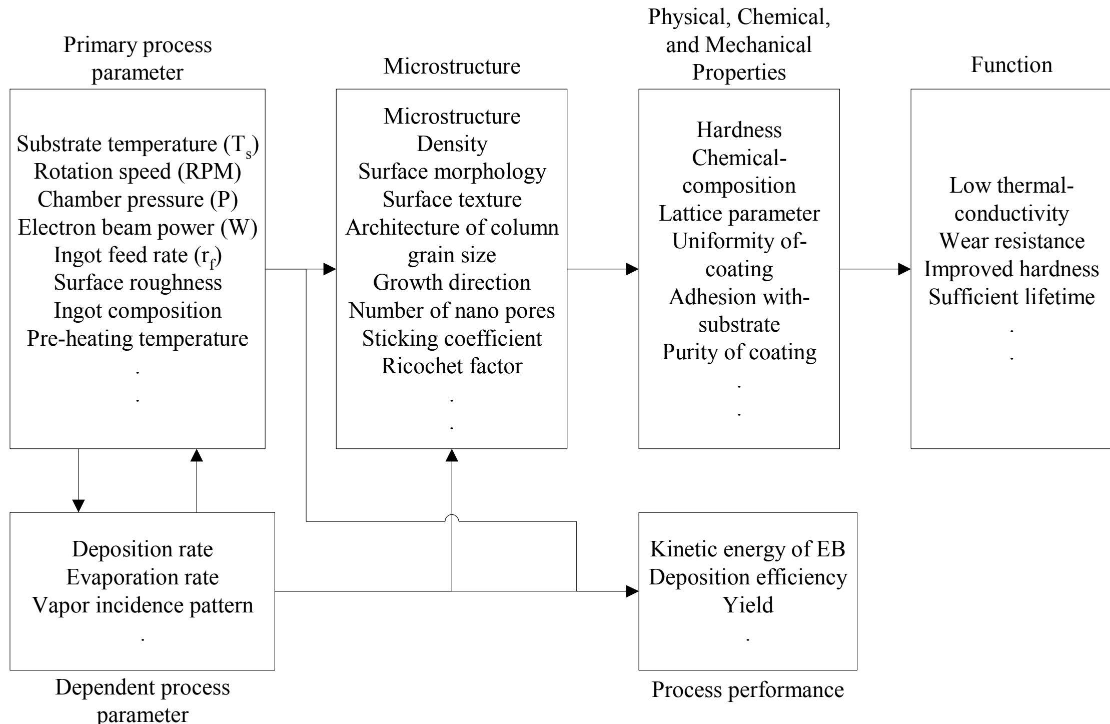

Figure 1.1. The relationship between process parameters, properties of coating, and functions of coating

To establish a PVD system, however, we need to consider production cost as well as engineering itself (Hill 1986). There can be a conflict between minimizing the production cost and maximizing the efficiency of process. That is, in the every step of the

design, process, product as well as maintenance, every decision maker will encounter multi-criteria decision making (MCDM) problems which have no optimal solution and only have efficient solutions. Anand et al. (1998) formulated an optimization problem to determine, several years in advance, various interconnect parameters of very-large-scale integrated circuits (VLSI's) for future, resulting the construction of an interconnect technology roadmap. Li and Palusinski (2003) presented a multiobjective optimization problem to select the number of signal layers in printed wiring board (PWB). They used physical models to develop the multiobjective optimization problem. In these works, standard solving methods such as the weighting method and distance-based methods were used to find the optimal solution for the application.

1.4. Real-time control of deposition process

To realize the potential of the nanostructured coatings with improved device performance and cost reduction simultaneously, reproducibility and reliability of coating growth have needed further development (Gell 1995b; Roco et al. 2000). Improved in situ sensing and feedback control of a deposition process should be developed to guarantee the high reproducibility and high uniformity of the coated structure (NRC 1996). Precisely controlling microstructures of coatings such as nano-scale pores and gaps in the columns can improve the properties of nanostructured coating. To open the road to an approach to tailor the microstructure and texture of coating layers, the effects of processing parameters of EB-PVD on the microstructure and texture of coating layers should be investigated (Yamaguchi, Wada, Kimura and Matsubara 2003). There has been

work on the intelligent automation of the EB-PVD process to achieve high quality and cost-efficient coatings for low-volume part productions using real-time feedback control (Lewis et al. 2000; Cho et al. 2005). They presented the thermocouple-based substrate-temperature control and melt pool control using real-time vision.

The availability of sensors to measure the real time states of the system has been one of the obstacles to the implementation of feedback control system to the nanostructured coatings. Recently, there has been research on process sensors for monitoring the deposition process in real time. They are vapor rate and composition sensors based on laser-adoption spectroscopy (Anklam et al. 1995; Berzins et al. 1995); real-time nonintrusive thin film growth sensor in the nanometer scale using grazing incidence small angle X-ray scattering (GISAXS) and surface differential reflectance spectroscopy (SDRS) measurements (Renaud et al. 2004); and melt pool temperature using image processing (Lewis, Brown and Tutwiler 2000). However, it is often difficult and unfeasible to install these sensors into the EB-PVD production line.

Munz (2003) successfully demonstrated the scale-up of nanoscale multilayered (superlattice) hard coatings to the industrial production using arc bond sputter technology, using large-scale industrial physical vapor deposition (PVD) equipment and a sufficiently high pumping speed. The case studies of the applications of the nanoscale multilayered (superlattice) hard coating to the special niches in advanced manufacturing technology such as metal-forming and cutting die steel, Inconel, stainless steel, and titanium indicates that the field of application is enormous. In these areas, especially the machining of hardened steels at high cutting speed, TiN/BN nanocomposite coatings by industrial size PVD unit also has been shown to be feasible (Holubar et al. 2000). Jones

and Voevodin (2004) used the closed loop feedback control in the deposition of nanocomposite of YSZ/Au films by the magnetron-sputtering pulsed laser deposition (MSPLD) method, where the laser energy and magnetron power settings were simultaneously controlled to regulate the plume emissions, based on the measurement of the intensity of laser ablation vapor plumes and magnetron Au plasma. The resulting thin films showed a uniform stoichiometry throughout their depth.

There has been an interesting work in model-based uniformity control for epitaxial silicon deposition (Gower-Hall et al. 2002). For performing combined run-to-run and lot-to-lot control they introduced new control strategies. They developed a design of experiment (DOE) using selected process inputs, using the result of which process models were generated via a statistically driven polynomial response surface modeling methodology; for process optimization, they introduced cost function built by a multiple response surface (MRS), which included the weighted sum of squared errors from the output targets. For the actual outputs in the cost function, they assumed the linear function with the DOE parameters and the constant terms updated after every run, based on exponentially weighted moving average (EWMA) method.

To control higher statistical moments of the microscopic distributions, such as the surface roughness (the second moment of height distribution on a lattice) or even the microscopic configuration (such as the surface morphology), 2D linear stochastic partial differential equation (PDE) models for thin film growth processes directly based on microscopic process rules was reported by Ni and Christofides (2005). Their models were applied to both multivariable predictive controller and conventional proportional integral (PI) feedback controller; they successfully regulated the thickness of the thin film and the

thickness variance by manipulating the substrate temperature and adsorption rate in long-range interaction dominated growth regime and in short-range interaction growth regime, respectively.

Since the deposition process in any evaporation technique is inherently nonlinear, any linearization or approximation will be carried for success of the control system. Sometimes, it is sufficient to consider only non-linearities in the gain of the process, and to approximate the dynamics by a linear model, resulting in a Wiener model which actually a linear dynamic element is followed by a static nonlinear element (Ikonen and Najim 2001). Norquay et al. (1998) showed that the incorporation of Wiener models into model predictive control (MPC) schemes effectively removed the nonlinearity from the control problem, retaining many of the favorable properties of linear MPC.

Junker et al. (2004) applied the Wiener model for the deposition process. In the manufacture of thin-film solar cells deposited by thermal evaporation, the product specifications on thickness and composition place high request on the tight control of the vapor flow rates from the sources. The multiple elemental sources are considered for the process; the deposition system the shifting flat planar substrate along the axis designated as x. For this process, they suggested two subsystem models. One is deposition model based on the cosine law of emission. It had a cinematic formulation in which the effect of the shifting operation upon the mass accumulation of the sources on the substrate was linearly represented in the state space formulation (i.e. linear dynamic element). The second is sensor model in which the final film thickness and composition were nonlinearly represented as the function of the outputs from the former deposition model (i.e. static non-linear element), resulting in the form of the Wiener model. They tested

two types of controllers, internal model control (IMC) and MPC. With the cinematic formulation, they efficiently formulated the relation of the thickness evolution to the substrate manipulation, which significantly affects the microstructure of coatings as well as the thickness of ones in the EB-PVD process.

Outside of the deposition field, there exists the need of tight control of the thickness and temperature for the thickness uniformity in the nano scale, i.e. in the microlithography in which the photoresist thickness uniformity after the spin-coating and softbake process has been required in the nano scale to ensure the smaller microelectronic devices. Ho et al. (2002) and Ho et al. (2004) used the sliding mode control algorithm and MPC algorithm, respectively, to control resist film uniformity and the temperature of the bakeplate. In the former sliding mode control algorithm, the transfer functions of processes were identified through experiments; in the latter, thermal soft-bake process was expressed as the partial differential equations of heat conduction in the wafer and the photoresist thickness was estimated with reflectance signal from wavelength spectrometers using the least square estimation method.

In early 90's, researchers at Stanford University used model-based control for the wafer temperature in rapid thermal processing of semiconductor wafers (Gyugyi et al. 1992). Interestingly, they implemented subspace-fitting technique for an identification of a state space model, resulting in an empirical model; instead of the PID controller common in the manufacturing world, they introduced a linear quadratic gaussian (LQG) controller to optimize the control system in terms of cost and performance.

Vancheeswaran et al. (1997) used the MPC concepts with the given process models for the high temperature consolidation of fiber reinforced metal matrix composite

preforms. They presented the cascade control strategy in which the plant model had the two subparts for a machine and a material; the outputs of the former machine model were inserted to the latter material model as inputs. Their method could provide the near optimal process schedules that evolve performance defining microstructural parameters (relative density, fiber fracture density and fiber-matrix reaction thickness) to pre-chosen microstructural goal states that result in composites of acceptable mechanical performance.

1.5. Issues addressed in this research

The focus of this research is on the development of reduced-order mathematical models and efficient computational models for controlling nanostructured coating processes using the EB-PVD process instead of the current “trial and error/recipe-based methods” used in industry. The schematic diagram of EB-PVD system is shown in Fig. 1.2 in which components correspond to rectangular blocks and the actions occurred in the components circle blocks.

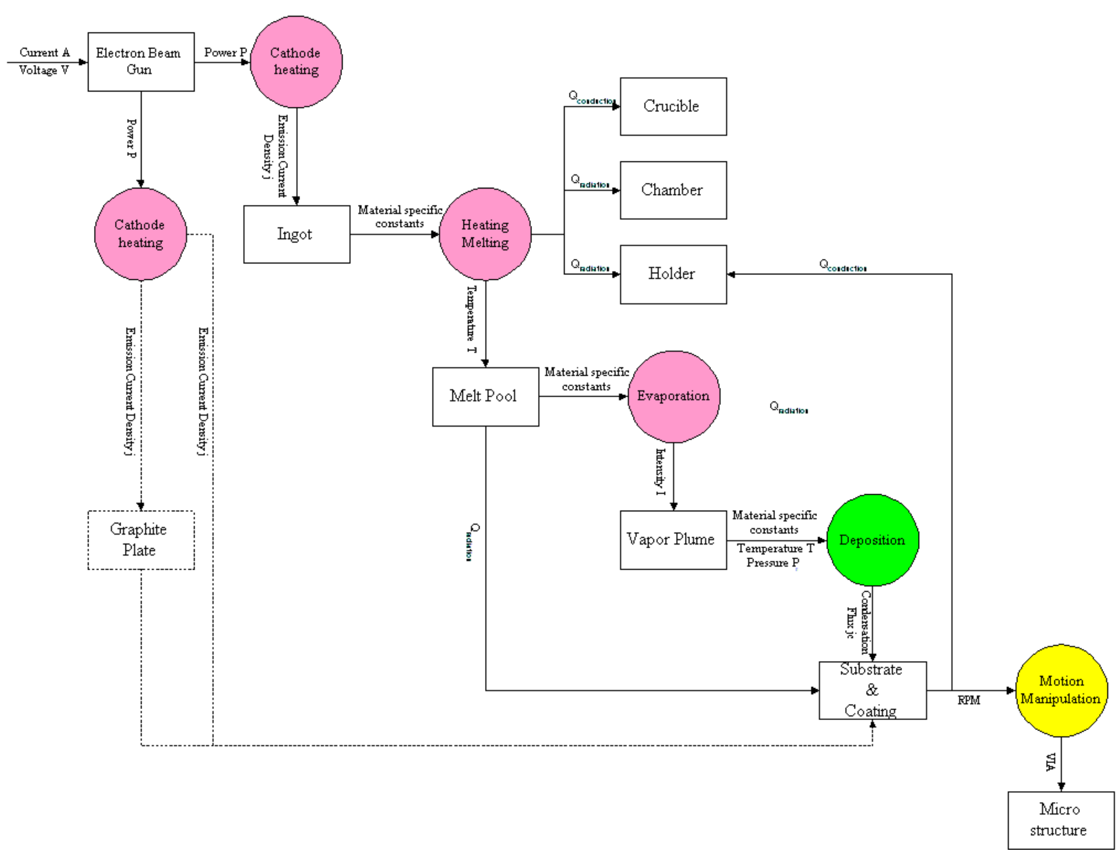

Figure 1.2. Schematic diagram of EB-PVD system

The first three actions in the circles such as cathode heating, heating and melting, and evaporation, will be included in machine dynamic model (MDM), the fourth action in the circle of deposition included in deposition process model (DPM), and the last action in the circle of motion manipulation included in substrate kinematics model (SKM). Arrows in Fig. 1.2 represent the inputs to and output from the components and actions. Dashed lines in one component and two arrows mean that only one of the two flows will be chosen in corresponding to the kind of EBPVD coater. The MDM needs to accomplish two objectives: the representation of key dynamics in the physical

phenomena and the economy of required resource; the DPM needs to characterize the physical relationship between the process parameters and the micro/nanostructure of the coating; the SKM needs to be computationally efficient for emulating various substrate motions.

For a spatial distribution-based analysis, the surface of the substrate is constructed by using finite elements method (FEM) generated from computer-aided design (CAD) model. The physical models for the EB-PVD process will be unified with the MDM, DPM and SKM. For computer aided engineering (CAE) of the EB-PVD process, a digital simulation tool will can enable to investigate the relationship between process parameters and the microstructure of coating based on requirements for the coating. It can also optimize the process planning of motion planning. There are always conflicting objectives for the EB-PVD such as cost, material collection efficiency, uniformity of coating, and lifetime. For example, substrate manipulation in the high intensity region of vapor plume can potentially improve the coating uniformity, the coating time, and the amount of material evaporated. However, this may reduce the total amount of the evaporated material that is deposited on the work-piece. The efficient multi-criteria decision making (MCDM) optimization method can generate the guide maps for process planning. Properly modeling the system and adequate real-time feedback control strategy incorporating available sensor technologies like quart crystal microbalance (QCM) has huge potential benefits at the nanostructured coating process using the EB-PVD technology. Figure 1.3 illustrates the intelligent process of the EB-PVD.

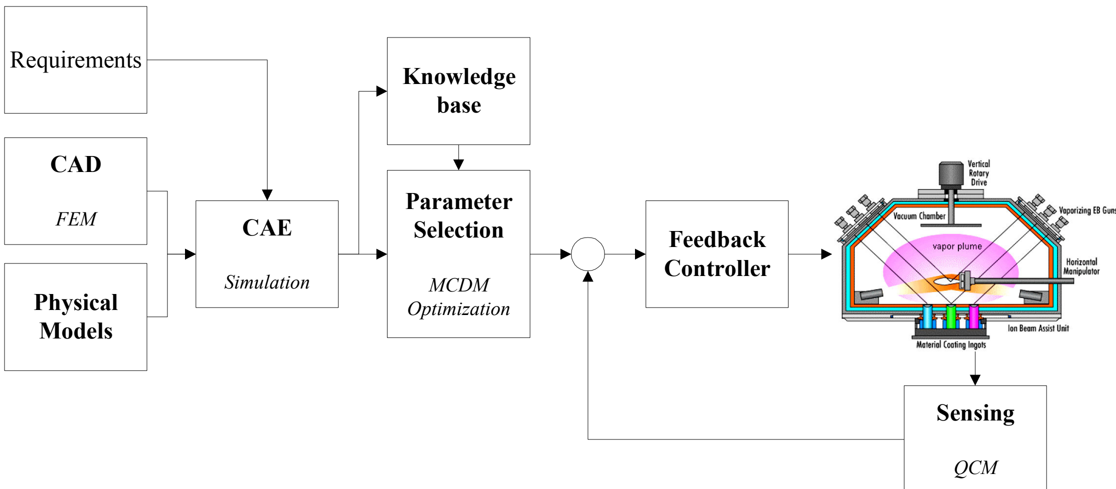

Figure 1.3. Intelligent processing of EB-PVD

The research issues that need to be investigated to accomplish the intelligent processing of nanostructured coating can be summarized as follows.

- Development of the MDM based on the scientific theories
- Development of the DPM to describes the coating evolution by relating the microstructures of coatings and process parameters in both macro- and micro-level
- Unification of the MDM and DPM with the SKM to develop a digital simulator of the EB-PVD process
- Evaluation of the digital simulator by the comparison with experiment results
- Development of automatic searching algorithm of the weight factors to solve MCDM problem and implementation of the developed heuristic to the EB-PVD process planning

- Development of the simplified model of the EB-PVD as single-input-single-output (SISO) using the digital simulator and determination of feedback control architecture that can be applied to the EB-PVD process using QCM

1.6. Thesis organization

Chapter 2 presents finite element models to describe machine dynamics, such as electron beam (EB) generation in an EB gun, EB scanning on the surface of an ingot, melting process of the ingot, and vaporization, and deposition on the surface of a substrate during EB-PVD process. Based on physical models, the finite element models relate the input power to the EB gun and the temperature profile of the ingot surface, the temperature profile to the shape of vapor plume, and the vapor distribution to the coating thickness. The two deposition-process models have been investigated for predicting the coating thickness and compared to experiments performed for simple shaped substrates.

In Chapter 3, the kinematics model of a substrate will be formulated using techniques commonly used in robotics, and a discrete state space model will be proposed for the unified dynamic models of EB-PVD, which combine the substrate kinematics with machine dynamics and deposition process. Substrate motion significantly affects the microstructure and texture of coating produced using EB-PVD and results in various kinematic modes by the design of a substrate holder. The proposed model is implemented in Matlab and tested on 3^n full factorial design of experiment that includes two represented kinematics modes for the YSZ coating on the turbine blade.

Chapter 4 covers a comprehensive modeling approach to link machine dynamics, substrate kinematics and resulting evolution of deposition in the EB-PVD. The evolution of coating is modeled using the level set approach, where the evolution of the surface is calculated by solving a Hamilton-Jacobi equation on a three-dimensional computational grid. The surface is given by the zero level set of the time-dependent level set function ϕ so that the value of level set of the surface is set to be zero at any time. The evolution speed for EB-PVD process is driven, which can relate the machine process parameters to the deposition process. YSZ deposition on the flat work-piece with rotation is investigated with the developed simulator that implements the proposed model in Matlab. The simulation results are provided to demonstrate that the proposed modeling approach can be applied to predict the evolution of coating of EB-PVD process in nano-level.

In Chapter 5, a new interactive fuzzy approach for solving multiple objective linear programming problems is presented. Decision makers' preference can be quantified with a membership function and a reference value, or threshold, of the membership function. A weighted sum of objective functions is assumed as a utility function, resulting in P_λ problem. Using the deviation of membership function from the threshold, a heuristic, called distributed arrival time control (DATC), which uses feed back control theory is applied to automatically search a set of weights factors in their space. The algorithm by combining the interactive fuzzy approach and DATC is implemented in Matlab and GAMS. The case study for manufacturing TBC made of YSZ using the EB-PVD process is provided to show the feasibility of the proposed algorithm. The formulation of an optimization problem is developed for the EB-PVD process, including four criteria (cost, uniformity of coating thickness, collection efficiency of

material on substrate, and lifetime). The physical models and statistical technique are used to develop the formulation and physical constraints also are included. To apply a heuristic developed for the distributed environment where multiple decision makers are in different location, the proposed problem is simplified with the given data and solved. The computational results are provided to show the process planning of the EB-PVD process with the multi-criteria optimization algorithm.

Chapter 6 covers a simplified model of the EB-PVD process to relate current input to the EB gun and the coating thickness. This model has been used to design and simulate a real-time PID controller. Simulation results indicate that the controller performs well in terms of disturbance-rejection in input power. The controller requires real-time feedback from quartz-crystal microbalance sensors, which makes it practically feasible and serve as a basis for spatial composition control.

In Chapter 7, finally, conclusions and recommendations for future work are presented.

Chapter 2

Finite element model for unified EB-PVD machine dynamics*

Most EB-PVD studies have tended to focus on an ideal vapor source with constant temperature over the whole area of melt pool. Many mathematical models assume that the temperature is from a point source to simplify the models. However, during the operation of the EB-PVD, it is very difficult to uniformly maintain the melt pool (Lewis et al. 2000). One of the reasons is impurities in the melt pool, which cause a non-uniformly distributed vapor plume. Moreover, there is little research which combines various dynamic aspects of EB-PVD, such as beam scanning pattern and temperature profile of a melt pool with macroscopic models of machine equipment and deposition process.

In this Chapter, finite element models are developed based on physical models to describe machine dynamics. These models include electron beam (EB) generation in an EB gun, EB scanning on the surface of an ingot, melting process of the ingot, vaporization of a source material, and deposition on the surface of a substrate during EB-PVD process. The finite element models relate the input power to the EB gun and the temperature profile of the ingot surface, the temperature profile to the shape of vapor plume, and the vapor distribution to the coating thickness. The two deposition process models are investigated for predicting the coating thickness. The implementation of the proposed models in Matlab is illustrated. The proposed FEM-based unified models of the

---

* Accepted for publication in Surface engineering (2006)

EB-PVD process are applied to predict coating thicknesses of simple geometric shaped substrates with various coating materials. The computational results are compared with experimental results. The comparison results indicate that the proposed models in this Chapter are feasible for the prediction of coating thickness.

2.1. Unified model of EB-PVD process

Due to the complexity of the EB-PVD process, to develop fully detailed process models of the system requires the complete understanding of the mechanisms of electron-beam melting, vaporization, and deposition. The non-linearity, multivariable, and uncertainty of an individual vapor particle in EB-PVD exacerbate the complexity of the EB-PVD process modeling. For example, radiation and conduction are both occurring when evaporants are being heated, melted, and evaporated to form a vapor plume by the emission current from an electron beam (EB) gun; once the evaporation of a source material starts, the pressure inside of the EB-PVD coater fluctuates. Thus, the input power to an EB gun results in a time-varying temperature within a chamber and a substrate, and a time-varying chamber pressure. The schematic diagram shown in Fig. 2.1 illustrates the complex EB-PVD process which includes sub-procedures such as machine dynamic process, deposition process, and substrate rotation.

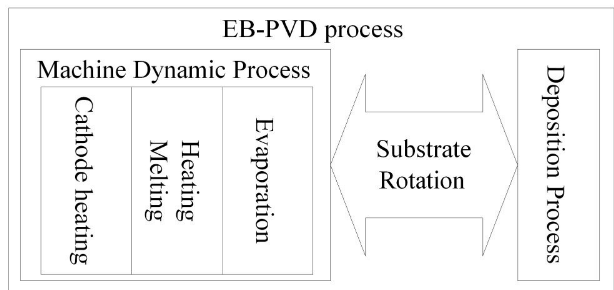

Figure 2.1. Schematic block diagram of EB-PVD process

Three blocks in the machine dynamic process correspond to the main phenomena which occur in the machine or EB-PVD coater during deposition process as follows.

- Cathode heating, resulting in the emission of EB
- Heating and melting of an ingot
- Evaporation of coating materials to generate a vapor plume.

The cathode heating inside of an EB gun is to generate the stream of free electrons which is accelerated and shaped into a beam in an electrostatic field and guided into the work chamber through a portal. Beam focusing and deflection is achieved by electric and magnetic fields. The EB becomes the energy source to heat, melt, and evaporate material ingots which are fed through crucibles at the bottom of the chamber, which also act as collectibles for the molten material as cooling water maintains the temperature around the designated temperature. As the high-powered EBs are focused on the material ingots, the heating/melting in the material ingots is to change the solid state of the material ingots to liquid phase before they are evaporated to form a vapor plume in the chamber. As the molten material receives enough energy input from the incoming EB, the phase changes from liquid to gas occurs on the surface of the melt pool, resulting in the formation of the vapor plume. Inside the vapor plume, the evaporants would move

straight from the surface of melt to the chamber in upward direction according to the energy which they received from the EB. As the evaporants propagate to the remote substrates, as well as chamber wall, they will condense on the surface of the substrates. The condensation of the evaporants on the surface, namely the deposition process in the Fig. 2.1, can be modeled as the deposition process. The proposed process models of the EB-PVD process will consist of empirical coefficients. When the needed empirical coefficients are not available, it is needed to make engineering assumptions to develop equations to assume the value of empirical coefficients. This Chapter will focus on determining the coating thickness for given conditions including machine dynamics, substrate geometry, and substrate rotation using the proposed united model of the EB-PVD process.

2.1.1. Machine dynamic model

2.1.1.1. EB gun model

As the first part in the machine dynamic model, a mathematical model is needed to describe the transformation of the input power into the output, emission current, by the cathode heating in an EB gun, called as EB gun model. The instantaneous electrical power P_{CH} delivered to a cathode in an EB gun is given by

$$P_{CH}(t) = A(t) \cdot V(t) \tag{2.1}$$

where $P_{CH}(t)$ is the instantaneous power, measured in watts, $A(t)$ is the current flowing through the cathode, measured in amperes, and $V(t)$ is the potential difference across it,

measured in volts (Schiller et al., 1982). Considering cathode heating efficiency, namely, the ratio of the emitted current I_e to the cathode heating input power $P_{CH}(t)$, the emitted current $I_e(t)$ is given by

$$I_e(t)=\eta_A \cdot P_{CH}(t) \tag{2.2}$$

where $I_e(t)$ is the emitted current, measured in amperes, and η_A refers to the cathode heating efficiency, measured in milli-amperes/watts (Schiller et al., 1982). Using the emitted current $I_e(t)$ in Eq. 2.2 and acceleration voltage $U_B(t)$ applied to the EB gun, the beam power, $p_0(t)$, measured in watts, can be expressed as follows (Schiller et al., 1982)

$$p_0(t) = U_B(t) \cdot I_e(t). \tag{2.3}$$

In this Chapter, to emulate the real world, a white noise term is added to three input variables, such as $A(t)$, $V(t)$, and $U_B(t)$, so that the beam power fluctuates around a mean value.

In addition to the emitted current, an EB scan pattern also needs to be considered because it influences the distribution of the emission current on the surface of material ingots and affects the resulting melt uniformity. In practice the EB scan pattern is one of the means used by operators to maintain a uniform melt which is critical for producing a uniformly distributed vapor plume (Lewis et al. 2000). There are many shapes of the EB scan pattern such as circle, swirl, and zigzag, etc. In this Chapter, a constant swirl shape is selected as the EB scan pattern used in the unified model since it is used in Penn State's Applied Research Lab. In addition, any impurity will be ignored in the melt pool. The swirl-shape pattern is shown in Fig. 2.2.

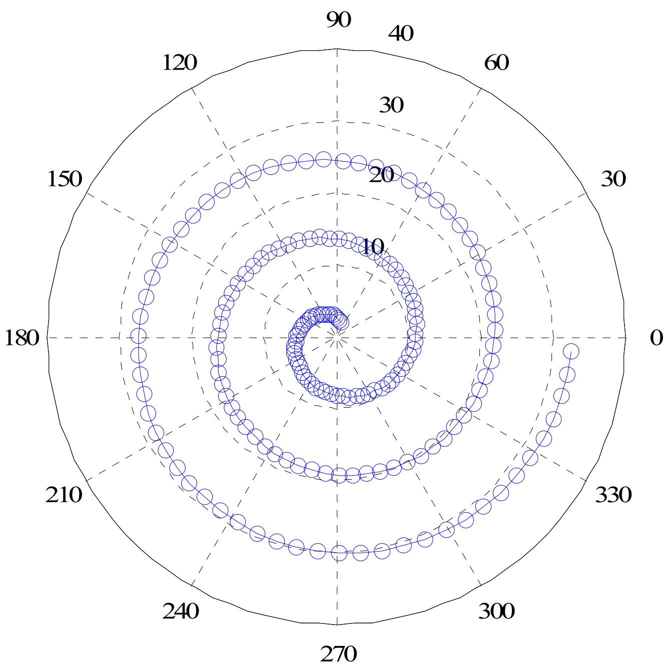

Figure 2.2. Example of EB scan pattern

The set of elements with the impingement of EB is determined by the EB scan pattern and the number of circulation of beam scan. The beam diameter is set to be 3mm as used at Penn State's Applied Research Lab.

2.1.1.2. Ingot heating/melting model

Ingots usually have a cylinder shape as they are held in water-cooling crucible. The surface of each ingot is modeled as a square mesh with square shaped elements based on two parameters: the diameter (ϕ_{ing}) and center (x_{org}, y_{org}) of the surface of the ingot. Let n_{mesh} be the number of the square mesh along a diameter of ingot, resulting in a square mesh of $n_{mesh} \times n_{mesh}$. The length of square elements is approximately equal to the beam diameter. The location of every element is represented by its centroid. To

determine the approximated circle from a square mesh, the ingot random variable s_{ij} is determined by

$$s_{ij} = \begin{cases} 1 & \begin{bmatrix} \alpha \le i \le \beta, \alpha \le j \le \beta & (c) \\ 1 \le i \le \alpha - 1, \begin{cases} j \le r_m, (r_m - j)/i < \theta & (u1) \\ r_m < j, (j - r_m - 1)/i < \theta & (u2) \end{cases} \\ \beta + 1 \le i \le n_{mesh}, \begin{cases} j \le r_m, (r_m - j)/(n_{mesh} - i + 1) < \theta & (b1) \\ r_m < j, (j - r_m - 1)/(n_{mesh} - i + 1) < \theta & (b2) \end{cases} \\ 1 \le j \le \alpha - 1, \begin{cases} i \le r_m, (r_m - i)/j < \theta & (l1) \\ r_m < i, (i - r_m - 1)/j < \theta & (l2) \end{cases} \\ \beta + 1 \le j \le n_{mesh}, \begin{cases} i \le r_m, (r_m - i)/(n_{mesh} - j + 1) < \theta & (r1) \\ r_m < i, (i - r_m - 1)/(n_{mesh} - j + 1) < \theta & (r2) \end{cases} \end{bmatrix} \\ 0 & \text{otherwise} \end{cases} \quad (2.4)$$

where i, j = 1,…, n_{mesh}, $r_m = n_{mesh}/2$ which corresponds to the radius of an approximated circle from a square mesh, $p_r = \lceil \sin(45) \cdot r_m \rceil$ which refers to the projection of a radius slanted with 45o onto the horizontal line, where $\lceil \cdot \rceil$ means the nearest integers towards infinity, $\alpha = r_m - p_r + 1$ and $\beta = r_m + p_r$, both of which refer to the index of sides of a square inscribed in a circle with the radius of r_m, and $\theta = (r_m - \alpha - 2)/(\alpha - 1)$ which refers to the slope of a reference line. First, when $\alpha \le i, j \le \beta$, $s_{ij} = 1$ as (c) in Eq. 2.4, which constructs the square inscribed in a circle with the radius of rm. Next, consider both of the half regions of the upper part with $1 \le i \le \alpha - 1$ in the square mesh, respectively. For the half region with $j \le r_m$, if the slope calculated by $(r_m - j)/i$ is smaller than θ, $s_{ij} = 1$, otherwise, $s_{ij} = 0$ as (u1) in Eq. 2.4. For the other half region with $r_m < j$, if the slope calculated by $(j - r_m - 1)/i$ is smaller than θ, $s_{ij} = 1$, otherwise, $s_{ij} = 0$ as (u2) in Eq. 2.4. For the other regions such as the bottom one with $\beta + 1 \le i \le n_{mesh}$, the left one

with $1 \le j \le \alpha - 1$, and the right one with $\beta + 1 \le j \le n_{mesh}$, the same approach for the upper region can be applied as shown in from (b1) and (r2) in Eq. 2.4. An example using Eq. 2.4 is shown in Fig. 2.3, where n_{mesh} = 10 and the element with an asterisk has 1 for s_{ij}.

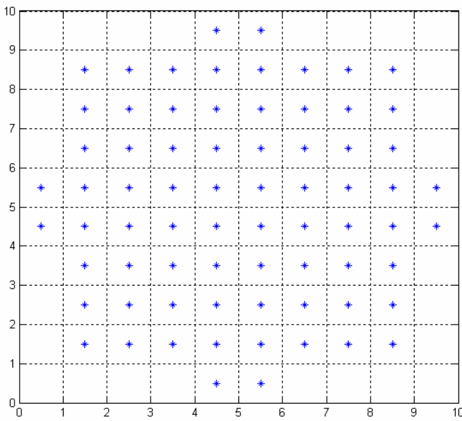

Figure 2.3. Example of s_{ij} when n_{mesh} = 10

Only elements with 1 for s_{ij} will be considered. The reason that the s_{ij} in Eq. 2.4 is used instead of calculating the distance from the center of ingot is to construct the finite element of a circle to improve accuracy when n_{mesh} is small and to keep the computation at a reduced level as n_{mesh} increases. Using the EB scan pattern shown in Fig. 2.2, the sequence with which the EB impinges on the elements of the mesh is determined.

As the emitted EB impinges on the surface of ingot, the energy of the beam will be transferred to the ingot, resulting in heating and melting of the ingot. Since all the impinging beam power is not absorbed, the portion of the absorbed impinging beam power is represented by η_B in the range 0 to 1. Thus, the power absorbed by an ingot, $p_A(t)$, can be obtained as follows (Schiller et al., 1982)

$$p_A(t) = \eta_B \cdot p_0(t) = \eta_B \cdot U_B(t) \cdot I_e(t). \quad (2.5)$$

The incident EB under the condition of the normal direction to the ingot surface shows the Gaussian rotationally symmetrical power density distribution (Lugscheider et al. 1998). To simplify this distribution in the mesh, the transfer of EB power to the eight surrounding elements of an (i, j) element where the EB impinges is only considered. Therefore, the ratio of the EB power can be defined, which will be transferred to nine elements including the (i, j) element and its eight surrounding elements, to the total absorbed EB power $p_A(t)$. First, most of input energy is absorbed by the (i, j) element and designated as α. The surrounding elements are classified into side-to-side and corner-to-corner and assign β and γ into four side-to-side elements and four corner-to-corner element, respectively. The relationships among α, β, and γ are:

$$\begin{aligned} &\alpha > \beta > \gamma \\ &\alpha + 4\beta + 4\gamma = 1 \end{aligned} \quad (2.6)$$

Figure 2.4 depicts the distribution of EB power with the impingement of EB on the (i, j) element. In this Chapter, the three values are set to be α=0.9, β=0.02, and γ=0.005, respectively, to focus 90% of the input energy to the element on which the EB impinges.

	j-1	j	j+1
i-1	γ	β	γ
i	β	α	β
i+1	γ	β	γ

Figure 2.4. The distribution of EB power with the impingement of EB on (i, j) element

The energy balance of the ingot and molten pool for the EB-PVD process is expressed in terms of the EB power absorbed by an ingot, the heating power, p_h, which heats evaporants to evaporation temperature, heat losses in the molten pool due to radiation and conduction, that is, p_{rad} and p_{cond}, respectively, melting power p_m, and evaporating power p_v. It is assumed that heat losses due to convection in the melt can be ignored. Therefore, the absorbed power by the ingot, $p_A(t)$, corresponds to the sum of the useful power p_{useful} which composes p_h, p_m, and p_v, and the loss power p_{loss} to the environment through radiation and conduction as following (Schiller et al., 1982):

$$
\begin{aligned}
p_A &= p_{useful} + p_{loss} = (p_h + p_m + p_v) + (p_{rad} + p_{cond}) \\
p_h &= \frac{d}{dt}(mc(T)T) \\
p_m &= a_v(T)q_m \\
p_v &= a_v(T)q_v \\
p_{rad} &= \int_{F_S} \varepsilon\sigma T(x,y)^4 \, dF \\
p_{cond} &= \int_{F_l} \lambda(T)\frac{dT(x,y)}{dl} \, dF
\end{aligned}
\tag{2.7}
$$

where m is mass of the evaporant, $c(T)$ is the specific heat, T is the temperature of the ingot or melt pool in K, $a_v(T)$ is the evaporation rate in $g \cdot s^{-1}$, q_m is the latent heat of melting, q_v is the latent heat of evaporation, F_s is the radiant surface, ε is the emissivity, σ is the Stefan-Boltzmann constant, F_l is the surface through which heat transfer takes places, and $\lambda(T)$ is the thermal conductivity. For reasons of simplification, let us assume that the EB current density is uniform over the entire element area, that the temperature over the surface of each element in the square mesh with $s_{ij} = 1$ is constant, that both the radiant surface F_s and the vapor-emitting surface F_v are alike and are same with the surface of an element in the square mesh, and that there is only an one-dimensional

thermal conduction along longitudinal direction of an ingot. The energy balance expressed by Eq. 2.7 is considered at every individual element of the square mesh with the area F_p (mm^2) and the side length R_p (mm). For the calculation of the heat exchange by radiation, the temperature of environment is calculated using isentropic expansion equation as following (Azad 1998):

$$T'_{ij} = T_{ij}\left(\frac{P'_{ij}}{P_{ij}}\right)^{\frac{\gamma_{ij}-1}{\gamma_{ij}}} \quad (2.8)$$

where T'_{ij} and P'_{ij} refer to the temperature and pressure of environment for an (i, j) element, respectively, T_{ij} and P_{ij} the temperature and pressure of the (i, j) element, respectively, and γ_{ij} the heat capacity ration of the (i, j) element. For the calculation of the heat exchange by conduction, only one-dimensional conduction between the element itself and imaginary element just below the interested element is considered. The temperature of imaginary element is calculated based on the work by Simon and Pal (1999), which provided the temperature field below the surface of the ingot and molten pool. The surface of the ingot is divided into five regions along the radius, resulting in the shape like target diagram with one center circle and four rings. Each region had its specified ratio of the decrease of the temperature along the axis direction of the ingot.

After time space is discretized in small interval τ and a forward difference operator is applied for the time variable (Smith 1985), Eq. 2.7 yields

$$T_{ij}^{k+1} - T_{ij}^{k} = \frac{\tau}{mc(T_{ij}^{k})}\left[\begin{array}{l} p_A - a_{vij}\left(T_{ij}^{k}\right)\cdot F_p \cdot q_m - a_{vij}\left(T_{ij}^{k}\right)\cdot F_p \cdot q_v \\ -\varepsilon\sigma F_p\left(\left(T_{ij}^{k}\right)^4 - \left(T'_{ij}\right)^4\right) - \dfrac{\lambda}{R_p}F_p\left(T_{ij}^{k} - T_{ij}^{b}\right) \end{array}\right] \quad (2.9)$$

where k is the integer ranging from 0 to $+\infty$, illustrating the time $t = k\tau$, i, j = 1,…,n_{mesh}, T_{ij}^{k} is the temperature of (i, j) element at time k, and T_{ij}' and T_{ij}^{b} are the temperature of the chamber environment and the imaginary element just below the interested element, respectively, in the (i, j) element.

According to Langmuir (1913), the specific evaporation rate a_{v1} in g·cm^{-2}s^{-1} that is the amount evaporated per unit time per unit area for vaporization of a substance in a high vacuum is given by

$$a_{v1} = \alpha_v \cdot 4.4 \cdot 10^{-4} \cdot p_S \cdot \left(\frac{M_D}{T_v} \right)^{1/2} \qquad (2.10)$$

where α_v is the evaporation coefficient which becomes 1 for idealized evaporation, p_s in Pa is the saturated vapor pressure at a temperature T_v, M_D is the molecular weight of the evaporant, and T_v is the absolute temperature of the evaporant. Instead of the saturated vapor pressure approximated given from the empirical data, here the vapor pressure is given by the Clausius-Clapeyron formula (Wark 1966)

$$\log_{10} p_s = -\frac{A}{T_v} + B + C \log_{10} T_v + DT_v . \qquad (2.11)$$

Substituting Eq. 2.11 into Eq. 2.10, the specific evaporation rate a_{v1} becomes the function of the temperature T_v which is computed from T_{ij} in Eq. 2.9. Assuming that the specific evaporation rate a_{v1} is constant over the surface of an individual element of the mesh, the relation between the evaporated mass a_v per unit time and the specific evaporation rate a_{v1} is

$$a_v = F_p \cdot a_{v1} . \qquad (2.12)$$

The initial temperature of ingots is assumed as the room temperature and the temperature of the boundary of the ingots also is assumed to be the room temperature because the water cooled crucible maintains boundary condition. When the surface temperature rises above a safe limit, the power to the EB gun will be interrupted to prevent overheating of the ingot. In this Chapter, the limit is set to be the middle between the melting and boiling point of the ingot. In addition, it is assumed that materials are fed constantly to replenish the material evaporated from the ingot and that the pressure inside of the chamber is assumed to be in high vacuum, usually of the order of 10^{-2} to 10^{-5} torr for the operation of generation and unrestricted propagation of the EB in the chamber.

2.1.1.3. Evaporation

The evaporation model will determine the dynamics of the vapor plume in the chamber, which is critical for calculating the distribution of evaporants in the chamber and, in turn, the prediction and control of the deposition rate and thickness uniformity across substrates from design parameters (Powell et al. 2001). The shape of vapor plume generated inside the chamber by the evaporation has been determined by the theory of evaporation which is called "cosine law of emission" (Glang 1970). According to this law, the power index n determines the vapor intensity of the evaporated material, which depends on the rate of evaporation. Therefore, the power index n will be the main output from this evaporation model. Since the cosine law is valid for small area evaporator where the diameter of the melt pool is much smaller than the distance between the melt pool and the substrate h_v, it is assumed that every element in the square mesh individually

acts as the ideal vapor source with much smaller area compared to h_v and the evaporated materials from one element do not have any interaction with the ones from the others. Hence, if the power index n for every element in the square mesh can be calculated, the final vapor plume can be determined by adding the individual vapor plume from every element. Graper (1973) showed that the power index is dependent upon deposition rate with the relation $n = K_n r^{1/4}$ where K_n is a constant and r is the deposition rate (Å/sec). According to Azad (1998), the deposition rate can be calculated from the difference between the influx of vapor into a workpiece and absorption flux. Thus, assuming that the deposition rate is proportional to the evaporation rate a_v, namely the influx of vapor, and using Eq. 2.8 and the equation of deposition rate by Azad (1998), the power of cosine of an individual element is estimated as follows:

$$n_{ij} = K_n \left[f\left(a_{vij}\right) \right]^{1/4} \tag{2.13}$$

where

$$f\left(a_{vij}\right) = \frac{10^{10}}{\rho \cdot F_p} \cdot K_a \left(1 - \frac{P_{ij}^{'}}{\sqrt{T_{ij}^{'}}} \Bigg/ \frac{P_{ij}}{\sqrt{T_{ij}}} \right) \cdot a_{vij} \tag{2.14}$$

where i,j = 1,…,n_{mesh}, ρ the material density, K_a is a coefficient calculated from the ratio of surface area between a vapor plume and an ingot, and a_{vij} is the evaporation rate in the (i, j) element. By this power of cosine a vapor plume from an element can be determined and be superimposed with the others, resulting in the shape of vapor plume. Here, n_{ij}, the beam collimation parameter, indicates the extent of focusing of the vapor plume (Powell et al. 2001).

2.1.2 Deposition process model

Fuke et al. (2005) proposed both analytical and computational models for the coating thickness for substrates with complex geometry such as turbine blades for the first time. But, they used the reference value of the coating thickness of a given point at which the rate of deposition was known from experiments. According to Fancey and Matthews (1993), depending on the various process parameters, an inverse power function of source to substrate distance could describe the coating thickness on a given position directly above and facing the source but the underlying difficulty remains in providing the value of the power. Two deposition process models will be compared and applied for prediction of coating thickness: Pulker's model (Pulker 1984) and Schiller's model (Schiller et al. 1982). In the second model, the coating thickness at a given element directly above and facing the source, which is the reference value for a coating thickness in other elements, will be provided by using the first Pulker's model. Figure 2.5 shows the geometrical relation between vapor source and surface element.

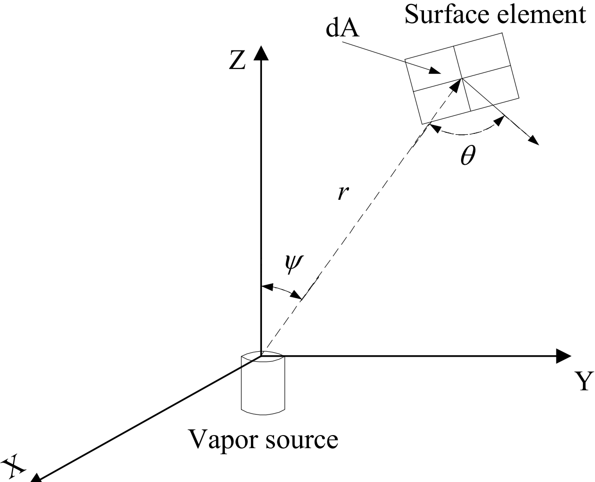

Figure 2.5. Geometrical relation between vapor source and surface element

In the Fig. 2.5, ψ denotes the angle between the direction of the emitted atom and the symmetry axis of the evaporation source, θ is the angle between the normal to the surface at the center of the substrate element with the area of dA and the incident vapor source beam, and r is the distance between the center of the substrate element and the vapor source.

According to Pulker (1984), the coating thickness on a substrate element, d_s, is obtained by

$$d_s = \frac{m}{\rho} \cdot \frac{n+1}{2\pi} \cdot \frac{\cos^n(\psi) \cdot \cos(\theta)}{r^2} \tag{2.15}$$

where n the beam collimation parameter. Differentiating Eq. 2.15 with respect to time t and replacing the temporal derivative of m in the right hand side of Eq. 2.15 with the evaporated mass a_v per unit time obtained by Eq. 2.12, yield

$$\dot{d}_s = \frac{n+1}{2\rho\pi} \cdot \frac{\cos^n(\psi) \cdot \cos(\theta)}{r^2} \cdot a_v. \tag{2.16}$$

Therefore, Eq. 2.16 becomes an ordinary differential equation with the right hand side which can be calculated from a_v and n provided by Eq. 2.12 and 13, respectively. In order to approximate $\dot{d}_s = f(n, \psi, \theta, s, a_v)$ where $f(\cdot)$ represents the right hand side of Eq. 2.16, discretizing time into small interval τ and applying the forward difference operator yield

$$d_s(k+1) = d_s(k) + \tau \cdot f(n, \psi, \theta, a_v). \tag{2.17}$$

Pulker's model in Eq. 2.15-2.17 can calculate the coating thickness at elements in the mesh.

Fuke et al. (2005) proposed the mathematical model to calculate the coating thickness, based on the second deposition process model, namely the Schiller's model. This model formulated the normalized value for the coating film thickness with respect to the one at $\psi = 0$ for a flat plate stationary above the evaporator source for a constant rate of evaporation (Schiller et al. 1982), as following:

$$\frac{d_s}{d_{s_0}} = \cos^n(\psi) \cdot \frac{\delta_0^2}{\delta^2} \cdot \cos(\theta) \qquad (2.18)$$

where d_s is the coating thickness at the point of interest, d_{so} is the coating thickness of a given point at which the rate of deposition is known from previous experiments, ψ and θ are shown in Fig. 2.5, δ is the distance of the point of interest from the vapor source, and δ_o is the distance of this given point, from the vapor source. As mentioned before, this formulation required the reference value of the coating thickness, d_{so}, from experiment.

2.2. Unified dynamics computational model

A generic computational model for predicting coating thickness was proposed by Fuke et al. (2005) because of the difficulty to derive analytical models to predict coating thickness for substrates with complex geometries like turbine blades. A unified dynamics computational model is proposed to combine the machine dynamic models and the deposition process model developed in the previous section. Figure 2.6 shows the organization of the unified dynamic computational model, where t represents the present time, t_{final} the simulation period, k the iteration number, and τ the time step of the simulation.

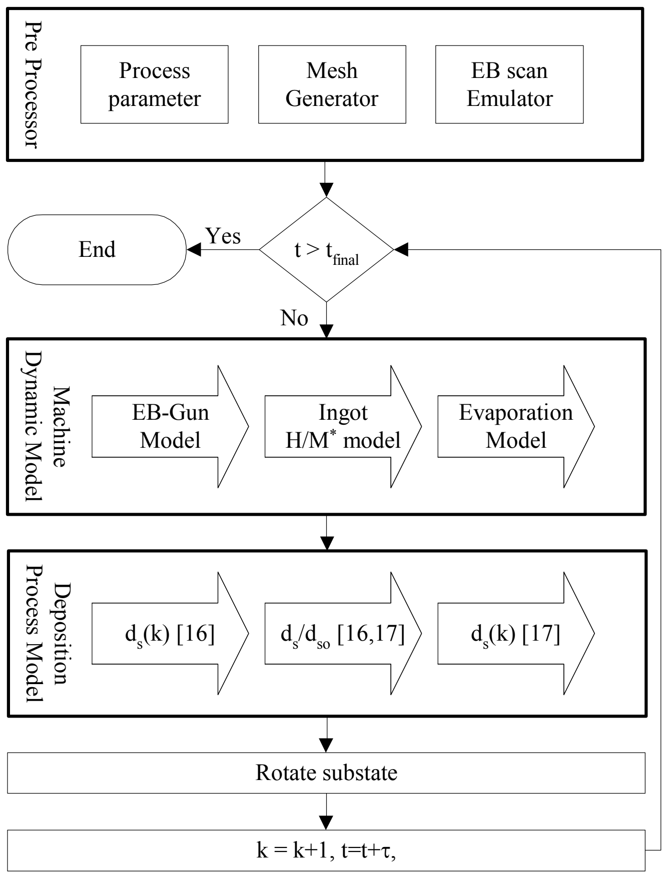

Figure 2.6. Organization for unified dynamic computational model, where H/M* is the acronym of heating and melting and [·] means the number of a related equation

In the "Pre Processor" shown in Figure 2.6, process parameters will be provided; mesh generator will generate a set of connected quadrilateral polygons and its centroids to approximate the surface of the substrate, where the coating thickness needs to be monitored. EB scan emulator will determine the set of the elements of the ingot mesh where the EB impinges based on the given scan pattern. Remainder of the computational steps calculates the coating thickness on the surface elements. Machine dynamic model explained in Section 2.1 calculates the temperature, the evaporated mass a_v per unit time,

and the beam collimation parameter n of every element in the ingot mesh. Using these data, deposition process model described in Section 2.2 calculate the coating thickness across substrate elements. To identify the points that are in the line of sight from the vapor source, a ray casting algorithm by Fuke et al. (2005) is adopted. After finishing calculation of the coating thickness, the next position of the substrate will be computed based on the motion plan and in turn, the spatial data of the substrate mesh will be updated. The computations stop after the desired duration of simulation, t_{final}, is completed. The assumptions that are made in this Chapter are summarized below:

- EB gun model
  - ✓ A constant swirl shape is selected as the EB scan pattern
  - ✓ Any impurity is ignored in the melt pool
- Ingot heating/melting model
  - ✓ The shape of an ingot is approximated with the variable s_{ij} in Eq. 2.4
  - ✓ The EB power is distributed both in one element where the EB impinges and in eight surrounding elements and α=0.9, β=0.02, and γ=0.005
  - ✓ Heat loss due to convection in the melt pool is ignored
  - ✓ EB current density is uniform over the entire element area
  - ✓ Heat loss due to radiation is calculated with T' obtained by isentropic expansion equation in Eq. 2.8
  - ✓ One-dimensional conduction is considered between the surface element of the ingot and the imaginary point below the surface
  - ✓ Saturated vapor pressure is given by Clausius-Clapeyron formula in Eq. 2.11
  - ✓ Initial temperature of the ingot is the room temperature (=273.5K)

✓ The safe limit of the temperature of the melt pool is set to be the middle between the melting and boiling point of the ingot

✓ The ingot are fed constantly to replenish the material evaporated

✓ The pressure inside of the chamber is in high vacuum so that the propagation of the EB in the chamber is unrestricted

- Evaporation model

✓ Every element in the square mesh acts as the ideal vapor source.

✓ There is no interaction between the evaporated materials so that the scattering of vapor particles is ignored.

✓ The deposition rate is proportional to the evaporation rate and is estimated by the formulation in Eq. 2.14.

- Deposition process model

✓ The ideal condensation is assumed which means that the influx of vapor is deposited without any loss in mass.

2.3. Experiments and Test results

In this section, to verify the usefulness of the finite element models discussed in the previous section, the computational model illustrated in Fig. 2.6 has been implemented using Matlab on a PC cluster LION-XO of Penn State's ASET. The simulation results using the implemented computational model are compared with experimental results. The experimental results were obtained using Penn State's industrial pilot Sciaky EB-PVD unit by Fuke et al. (2005). These experiments included

simple geometric shapes such as a cylinder rod coated with tungsten and a flat plate coated with titanium. Figure 2.7 depicts the experimental arrangement for the cylinder rod and the disk-shaped plate.

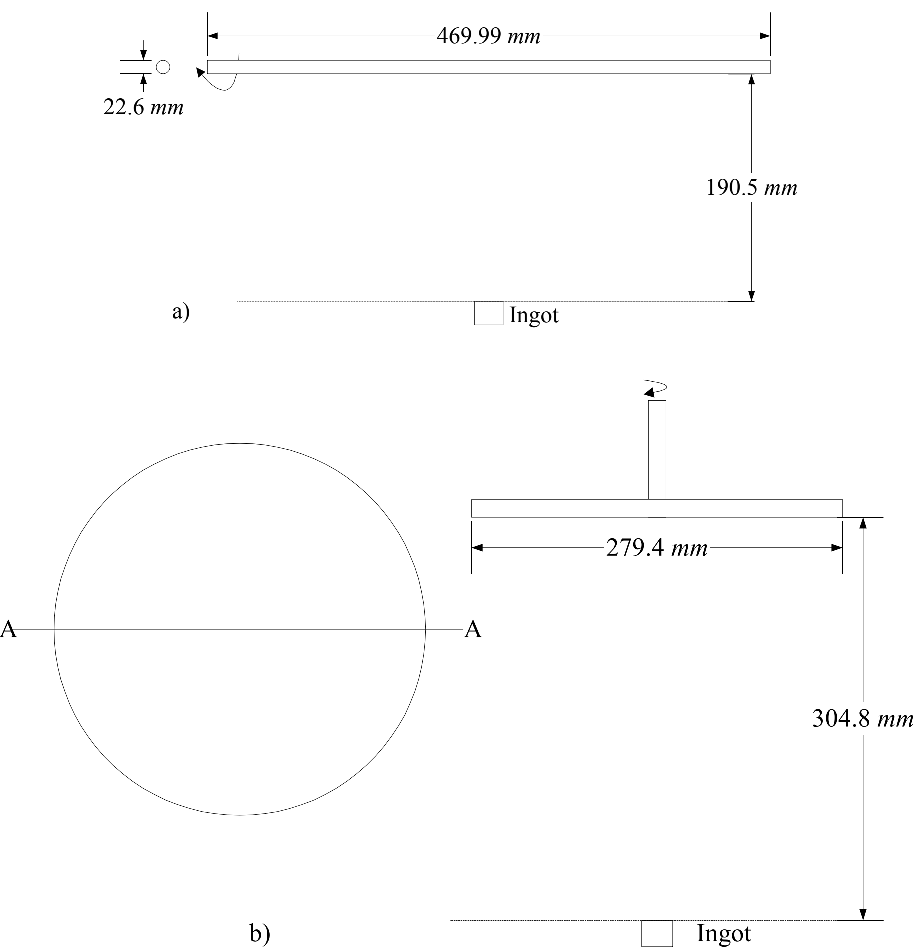

Figure 2.7. The experimental arrangement for a) cylinder rod and b) a disk-shaped plate

A cylindrical graphite rod 469.99 mm long and 22.6 mm thick was mounted along the horizontal axis, with a source-to-substrate distance of 190.5 mm. It was rotated about the horizontal axis at 10 RPM at a height of 190.5 mm from the vapor source. A flat, disk-

shaped plate with the diameter of 279.4mm was mounted on a vertical manipulator at a height of 304.8mm directly over the center point of the vapor source. The plate was rotated at 6 RPM about the vertical manipulator. In both experiments, the center point of cylinder shaped ingot was assumed to be the origin of the coordination system. The finite element mesh used for simulations in each case was generated according to the experiment layout shown in Fig. 2.7. The number of element nodes (n_e) and the number of polygons (n_p) in the case of the cylinder rod was 1323 and 1240, respectively; in the case of the flat plate, n_e = 1794 and n_e = 1710, respectively. As mentioned before, Fuke et al. (2005) used the computational deposition model, based on the Schiller's model that needs the reference value of the coating thickness of a given point, to predict the deposition thickness on the surface of a substrate without a consideration of the characteristics of an ingot material. In contrast, the unified dynamic computational model in this Chapter considers the machine dynamics including the ingot heating and melting. Therefore, the thermophysical properties of an ingot material should be considered. The thermophysical properties of tungsten and titanium used in this research are summarized at Table 2.1. In addition, Table 2.2 contains values for machine process parameters and empirical parameters used commonly in the simulations of both the cylinder rod and the flat plate. The three empirical variables, evaporation coefficient, vapor flux scattering coefficient, and condensation coefficient, are set to be 1 based on the assumption of ideal condition given in the previous section.

Table 2.1. The themophysical properties of titanium and tungsten

Properties	Tungsten (W)	Titanium (Ti)
Melting point (T_m)) (Chase 1986)	3650 K	1950 K
Vaporizing temperature (T_v) (Chase, 1986)	5800 K	3550 K
Theoretical density (ρ)	19.25 g/cm3	4.506 g/cm3
Molecular weight (M_D) (Chase, 1986)	183.86 g/mol	47.90 g/mol
Ratio of beam power absorbed in material (η_B) (Schiller et al., 1982)	0.63	0.74
Emissivity (http://www.electro-optical.com)	0.27	0.12
Latent heat of melting (q_m) (Chase, 1986)	189.64 kJ/kg	323.34 kJ/kg
Latent heat of evaporation (q_v) (Chase, 1986)	4387.35 kJ/kg	8957.52 kJ/kg
Thermal conductivity (λ(T)) (Touloukian 1970-79)	$\lambda(T) = 235.227 - 0.227044\ T + 0.00011405\ T^2$ W/(m*K) (100K < T < 1000K), $\lambda(T) = 149.919 - 0.0347802\ T + 0.00000503\ T^2$ W/(m*K) (1000K < T < 3653K), $\lambda(T) = 23.0206 + 0.0181452\ T - 0.00000141\ T^2$ W/(m*K) (3653K < T < 23000K)	$\lambda(T) = 53.2 - 0.321\ T + 0.00117\ T^2 - 0.000001\ T^3$ W/(m*K) (40K < T < 350K), $\lambda(T) = 29.3 - 0.0368\ T + 0.000042\ T^2 - 0.00000001\ T^3$ W/(m*K) (350K < T < 1100K), $\lambda(T) = 11.9 + 0.00843\ T$ W/(m*K) (1100K < T < 1950K), $\lambda(T) = 11.9 + 0.00843\ T$ W/(m*K) (1950K < T)
Specific heat (c_p) (Touloukian, 1970-79)	$c_p = -2E-12T^3 + 1E-6T^2 + 0.0225T + 126.51$ J/(kg*K) (273.15K<T<3650K), c_p =221.86 J/(kg*K) (3650K< T)	$c_p = 0.3159T + 423.92$ J/(kg*K) (294.09K<T<1123.15K), c_p = 699.89 J/(kg*K) (1123.15K<T)
Vapor Pressure (P) (Shackelford and Alexander 2001)	$\log(P) = 32.2 - 53529/T - 6.20\log(T)$ (Pa)	$\log(P) = -17.7 - 15338/T + 6.23\log(T)$ (Pa)

Table 2.2. Parameters used in the simulation

Machine parameters	Empirical parameters
Ingot height = 500 mm Cathode heating efficiency ηA=3.0 mA/W EB diameter = 3 mm EB Scan pattern = Swirl # of circulation of beam scan = 7 Scan frequency = 100 kHz	Variance of white noise of current and voltage = 0.01 Initial temperature of ingot and crucible = 298.15 K Evaporation coefficient (αv) = 1 (ideal evaporation) Vapor flux scattering coefficient = 1 (no scatter) Condensation coefficient = 1 (ideal condensation)

The machine parameters related to the input power and the time step of simulation τ shown in Fig. 2.6 were set in both cases as shown in Table 2.3. Figure 2.8 shows the screenshots of the developed computational models in Matlab.

Table 2.3. Machine parameters and time step used in the simulation

Experiment / Parameters (unit)	Cylinder rod with Tungsten	Flat plate with Titanium
Current of EB Gun A (A)	20	12
Voltage of EB Gun V (V)	100	100
Acceleration voltage UB (V)	10,000	10,000
Time step τ (sec)	0.01	0.01

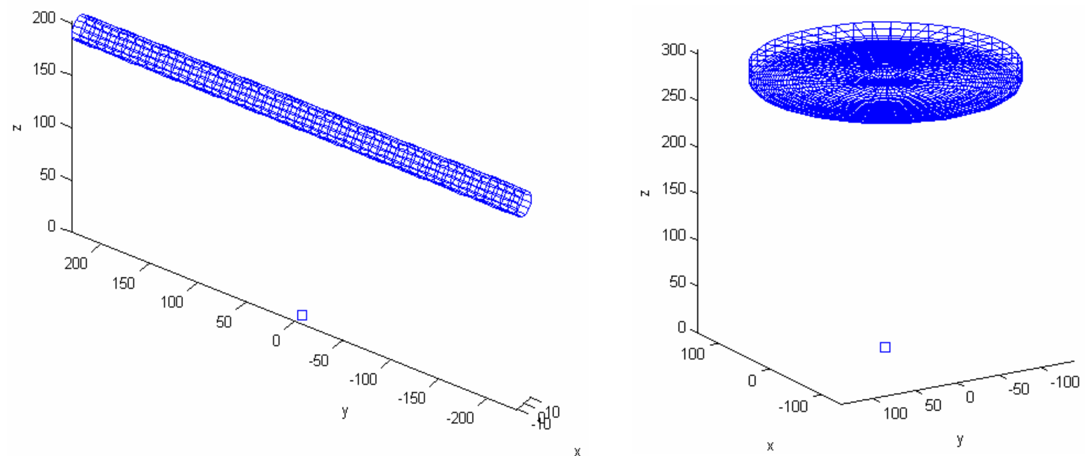

a) cylinder rod coated with tungsten b) flat plate coated with titanium

Figure 2.8. The screenshots of the developed computational models in Matlab

2.3.1. Cylinder rod coated with tungsten

The coating thicknesses obtained experimentally at various points along the cylinder rod are compared with those predicted using the unified dynamics computational models in Table 2.4, which shows the simulation results at 20sec, and the coating thicknesses along the longitudinal direction of the cylinder rod against divergence angle (ψ) are plotted in Fig. 2.9 as time increases from 0.2 sec to 20.2 sec, where the time interval of each curve is the same as 2sec. In Table 2.4, the simulation results d_3 by Fuke et al. (2005), which was based on the point vapor source with constant power of cosine *n*, is also compared as a reference. The d_1 and d_2 in Table 2.4 were obtained at 19.59^o, 26.48^o, -30.67^o, 32.64^o of divergence angle, respectively, because of the discrepancy between mesh and real measure points.

Table 2.4. Comparison of experiment and simulation for a cylinder rod coated with W

Divergence Angle (Degrees)	Experimental thickness d_e (μm)	Predicted thickness d_1 (μm)	Difference $\left(\frac{d_1 - d_e}{d_1}\right)$	Predicted thickness d_2 (μm)	Difference $\left(\frac{d_2 - d_e}{d_2}\right)$	Predicted thickness d_3 (μm)	Difference $\left(\frac{d_3 - d_e}{d_3}\right)$
19.19	0.025	0.025	0 %	0.0250	0 %	0.023	- 8.70 %
25.8	0.02	0.0216	7.41 %	0.0216	7.41 %	0.019	-5.26 %
–30.26	0.014	0.0193	27.46 %	0.0192	27.08 %	0.0155	9.68 %
31.66	0.014	0.0181	22.65 %	0.0181	22.65 %	0.015	6.67 %

* d_1 by Pulker's model, d_2 by Schiller's model, d_3 by Fuke et al. (2005)

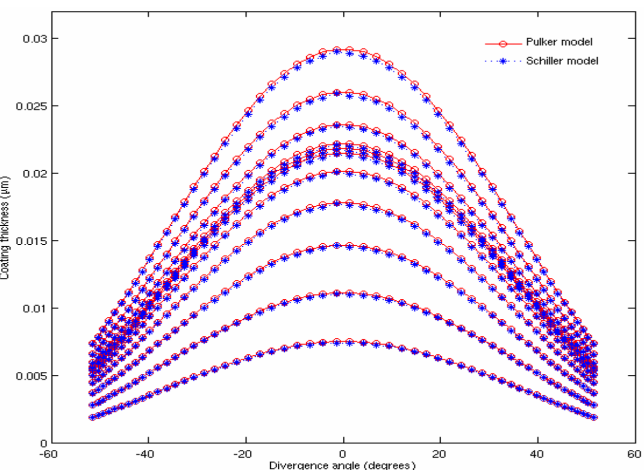

Figure 2.9. The coating thicknesses along the longitudinal direction of the cylinder rod against divergence angle (ψ) as time increases from 0.2sec to 20.2sec with the time interval of 2sec

As is seen from the difference in the experimental coating thickness d_e and the coating thicknesses d_1, d_2 and d_3 from simulation, respectively, the unified dynamic computational models could predict the coating thickness in the low divergence angle within the difference of about 8%; as the divergence angle increases over 30°, the

difference increases over 20%. The difference between experiment and unified dynamic models may come from the difference of the power of cosine n, which relates to the extent of vapor plume focusing (Powell et al. 2001). That is, the focusing of vapor in the experiment was larger than the one in the unified dynamic models. As can be seen in Table 2.4, the point vapor source based simulation predicted coating thicknesses d_3 in higher divergence angle better than the proposed deposition process models. However, the real vapor source diameter during the experiment was difficult to measure. In the simulation, the only swirl scanning pattern, which was maintained during the simulation, was used. Thus, the outside of the ingot could be heated over the melting point and the effects of the outside region as well as the effect of the core of the ingot melt pool were included in the calculation of the coating thickness. This resulted in over-calculation in the region with higher divergence angle. According to Fig. 2.9, the uniformity of the coating thickness along the longitudinal direction was decreased with the increase of time.

2.3.2. Flat plate coated with titanium

The ratios of the coating thicknesses obtained experimentally at various points with two divergent angles for the flat plate are compared with those predicted using the unified dynamics computational models as well as the simulation results by Fuke et al. (2005) in Table 2.5, which shows the simulation results at 90sec. Figure 2.10 shows the predicted ratio of the coating thicknesses both of the points with two divergence angles, 14.09^{o} and 25.52^{o}, and of the points along A-A section in Fig. 2.7 (b), which are obtained

at 90sec. The results of the prediction using the proposed models matched well with the experimental results as can be seen in Table 2.5. The proposed model provided more precise predicted coating thickness compare to the previous work. Figure 2.11 shows the change in the coating thickness in the A-A section as time increased from 1.4 sec to 3 sec, where the time interval of each curve is the same as 0.06sec.

The center point of the plate showed always the highest coating thickness at all time. From Tables 2.4 and 2.5, it can be seen that the simulation results in Table 2.5 agreed better with the experimental results than ones in Table 2.4. The reason may be that a cylinder rod in Table 2.4 has rapid change of coating thickness in higher divergence angles than a flat plate in Table 2.5 because two deposition process models, Pulker's model in Eq. 2.15-2.17 and Schiller's model in Eq. 2.18, depend on the geometry of substrate. Therefore, difference between experiment and simulation can worsen in the case of the cylinder rod compared to in the case of the flat plate. In the two experiments, the two deposition process models produced similar prediction about coating thickness. See Fig. 2.9 and 2.11. This can be explained that both models compute the spatial relationship between the vapor source and substrate and are based on the cosine law of emission (Glang 1970). The only difference of them is that the Pulker's model considers the evaporation mass and the Schiller model does not. As explained before, the latter needs the reference value d_{so} to calculate the coating thickness as seen in Eq. 2.18, which was calculated from the element just above the vapor source using the former; the coating thickness for the element should be equal for both model. This same reference coating thickness resulted in the similar prediction by both deposition models.

Table 2.5. Comparison of experiment and simulation for a flat plate coated with Ti

Divergence Angle (Degrees)	Experimental $r_e(\frac{ds_e}{ds_o})$	Predicted $r_1(\frac{ds_1}{ds_o})$	Difference $\left(\frac{r_1 - r_e}{r_1}\right)$	Predicted $r_2(\frac{ds_2}{ds_o})$	Difference $\left(\frac{r_2 - r_e}{r_2}\right)$	Predicted $r_3(\frac{ds_3}{ds_o})$	Difference $\left(\frac{r_3 - r_e}{r_3}\right)$
13.6	0.933	0.9113	-2.38 %	0.9113	-2.38 %	0.892	-4.60 %
25.86	0.733	0.7314	-0.22 %	0.7315	-0.21 %	0.66	-11.06 %
13.6	0.9537	0.9112	-4.66 %	0.9113	-4.65 %	0.892	-6.92 %
25.86	0.746	0.7314	-2.00 %	0.7314	-2.00 %	0.66	-13.03 %
13.6	0.869	0.9112	4.63 %	0.9112	4.63 %	0.892	2.58 %
25.86	0.7	0.7313	4.28 %	0.7314	4.29 %	0.66	-6.06 %

* r_1 by Pulker's model, r_2 by Schiller's model, r_3 by Fuke et al. (2005)

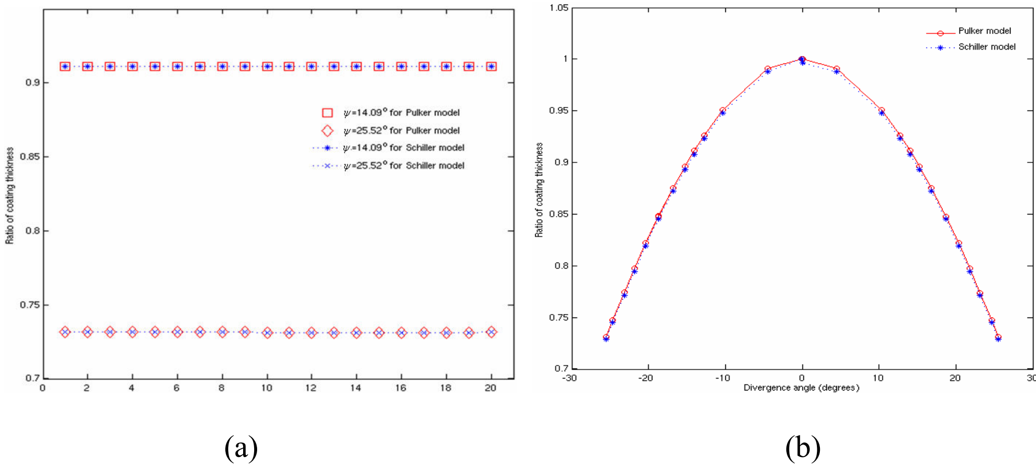

(a) (b)

Figure 2.10. Ratio of coating thickness: a) in two divergence angle, b) along A-A section

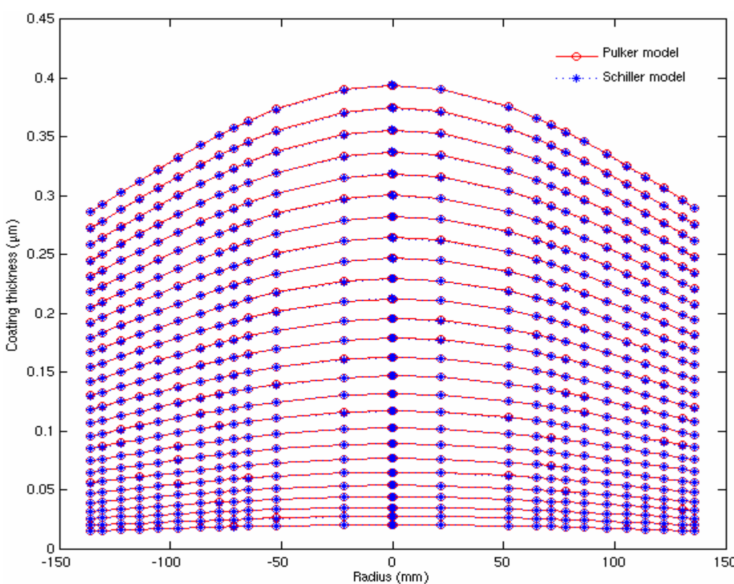

Figure 2.11. Coating thickness along A-A section in the flat plate as time increases

2.4. Summary

Finite element models for the EB-PVD process have been developed. In the models, the reduced-order physical models for various aspects of the EB-PVD machine dynamics such as EB generation and scanning, ingot melting, and evaporation are utilized in accordance with the discretized mesh of an ingot and a substrate. The unified dynamic computational model based on the proposed finite element models was implemented in Matlab to enable the prediction of coating thickness. The numerical experiments were conducted on two test cases: a cylinder rod coated with tungsten and a flat plate coated with titanium. The simulation results of the experiments were compared with experimental data. The comparison results indicate that the proposed unified dynamic computational model is feasible for the prediction of coating thickness.

Chapter 3

Discrete state space model for substrate motion in EB-PVD process*

Substrate motion significantly affects the microstructure and texture of coating produced using EB-PVD. A substrate holder, or fixturing, mainly affects the kinematics modes in the substrate motion. The kinematics mode of a substrate motion is mathematically formulated using techniques commonly used in robotics. A discrete state space model for the unified dynamic models of EB-PVD is proposed, which combine the substrate kinematics with machine dynamics and deposition process. The proposed model is implemented in Matlab to develop a simulation tool, or a simulator, that allows exploring the various kinematics modes during the deposition process and enables to assess the design of a fixturing and the feasibility of the condition of kinematics parameters.

A case study is presented of two substrate holders to validate that the proposed model can emulate various kinematics modes of a substrate. The two holders have different kinematics modes. A turbine blade is chosen as a substrate on which YSZ is deposited as coating. Statistical experimental design is used to study the effects of kinematics parameters on the performance of the EB-PVD process as well as the validation of the performance of the proposed model. Three-level full factorial design is chosen for experimentation. The results are statistically analyzed using Minitab.

---

* Submitted to Surface and Coatings Technology (2006)

3.1. Structure of EB-PVD process

Due to the complexity of the EB-PVD process, developing detailed process models of the system requires a complete understanding of the mechanisms of EB melting, evaporation, and deposition. The non-linearity, multivariability, and uncertainty of an individual vapor particle in vapor plume exacerbate the complexity of the EB-PVD process. In addition, substrate manipulation that changes the vapor incidence angle highly affects the kinetics of vapor particles in the vapor plume as well as the deposition process. Especially, the effect of the substrate manipulation on the microstructure of coating becomes more critical in the situation that the microstructure of coating is required to be controlled in nano-level. As the adequate description of the process becomes difficult, the availability of the process model decreases and it is impossible to apply modern advanced control methods such as adaptive control, predictive control, multivariable control and robust control. If simplified order models are developed based on a combination of simplified physical processes, the reduced order model can acquire the key dynamics of the system (Azad 1998). The decomposition of the EB-PVD process is described in Fig. 3.1.

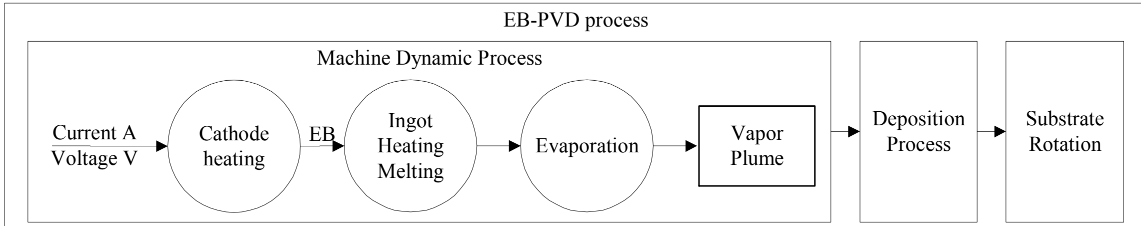

Figure 3.1. Decomposition of EB-PVD process that consists of three sub processes

The proper connection among three sub-process models of the EB-PVD process is a cascade connection, making outputs of a model as the inputs of next model. The interconnection among three models is shown in the Fig. 3.2, where a machine controller is also considered with respect to the models of the EB-PVD process.

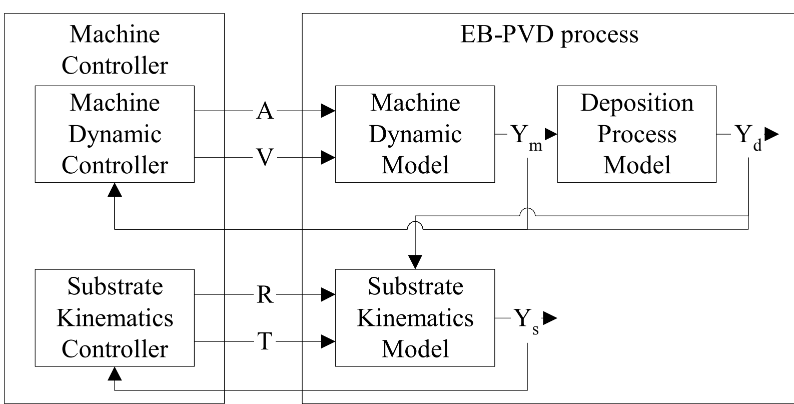

Figure 3.2. The architecture of EB-PVD process model

Machine dynamics model (*MDM*) shown in Fig. 3.2 combines models of various component dynamics in the EB-PVD machine such as cathode heating, ingot melting, and evaporation and generates the outputs Y_m based on the inputs current A and voltage V; Y_m acts as the inputs of next model, Deposition Process Model (*DPM*) shown in Fig. 3.2. DPM can predict the coating thickness and provides the output Y_d into next Substrate Kinematics Model (*SKM*) shown in Fig. 3.2. SKM unifies the evolution phenomena of the surface of a substrate and its geometric models that are computationally efficient for modeling the kinematics of substrate and manipulator motion. SKM processes inputs such as rotation velocity R and translation velocity T as well as Y_d from DPM to produce the ourput Y_s. MDM needs to accomplish two objectives: both the representation of key

dynamics in the physical phenomena and the economy of required resource (Azad 1998). Both MDM and DPM in Fig. 3.2 are proposed in Chapter 2. Y_m is defined as the beam collimation parameter or the power index of cosine law of emission (Glang 1970), Y_d and Y_s as coating thickness on the surface of the substrate. The surface of the substrate is constructed by using finite element method as spatial distribution-based analysis. In this Chapter, the two models, MDM and DPM, will be summarized with the lumped nonlinear state formulation. In addition, the SKM will be newly modeled using the lumped linear state space formulation because modeling by the state space formulation decreases the computation time compared to the conventional sequential simulation.

3.1.1. Machine dynamics model

Physical interactions in the EB-PVD machine dynamics can be simply described as follows:

$$
\begin{aligned}
\frac{\mathrm{d}\mathbf{x}_{\mathrm{m}}(t)}{\mathrm{d}t} &= \mathbf{f}_{\mathrm{m}}\left(\mathbf{x}_{\mathrm{m}}(t), \mathbf{u}_{\mathrm{m}}(t), t\right) \\
\mathbf{y}_{\mathrm{m}}(t) &= \mathbf{g}_{\mathrm{m}}\left(\mathbf{x}_{\mathrm{m}}(t), \mathbf{u}_{\mathrm{m}}(t), t\right)
\end{aligned}
\quad (3.1)
$$

where $\mathbf{x}_{\mathrm{m}}(t)$ is the state vector consisting of variables related to electron beam emission, heating and melting, and, evaporation, $\mathbf{u}_{\mathrm{m}}(t)$ the input vector consisting of time varying factors, $\mathbf{y}_{\mathrm{m}}(t)$ the output vector just one of the factors included in the state vector and $\mathbf{f}_{\mathrm{m}}(\cdot)$ and $\mathbf{g}_{\mathrm{m}}(\cdot)$ are nonlinear functions of $\mathbf{x}_{\mathrm{m}}(t)$, $\mathbf{u}_{\mathrm{m}}(t)$, and t. Since a simplified finite element model of the ingot in Chapter 2 is presented as a square mesh with n_{mesh} by n_{mesh} where n_{mesh} is the number of the square mesh along a diameter of ingot, the lumped MDM in

Eq. 3.1 corresponds to the representative element in the square mesh. The input vector, $\mathbf{u}_m(t)$, of the MDM consists of the commanded time varying factors of inputs current A and voltage V as follows.

$$\mathbf{u}_m(t) = [\dot{A}\ \dot{V}]^T \tag{3.2}$$

The state vector, $\boldsymbol{x}_m(t)$, of the MDM consists of a set of factors relating to the heating and melting of coating material ingot and evaporation. They are the power absorbed by an ingot (p_A), the temperature of the ingot (T); the evaporation rate (a_v) which means the amount evaporated per unit time, the vapor pressure given by the Clausius-Clapeyron formula (p_s), and the beam collimation parameter or the power index of the cosine law of emission (n). Thus, the 5×1 state vector, $\boldsymbol{x}_m(t)$, is expressed as follows.

$$\mathbf{x}_m(t) = [p_A\ T\ a_v\ p_s\ n]^T \tag{3.3}$$

The output vector, $\boldsymbol{y}_m(t)$, from the MDM is the evaporation rate (a_v) and the power of cosine (n).

$$\mathbf{y}_m(t) = [a_v\ n]^T \tag{3.4}$$

Due to the selection of $\boldsymbol{x}_m(t)$ and $\boldsymbol{y}_m(t)$, the second equation in Eq. 3.1 has linear form expressed as below

$$\mathbf{y}_m(t) = \mathbf{c}_m \cdot \mathbf{x}_m(t) + \mathbf{d}_m \cdot \mathbf{u}_m(t) \tag{3.5}$$

where $\mathbf{c}_m = [0\ 0\ 1\ 0\ 1]$ and $\mathbf{d}_m = [0\ 0]$. The complete MDM is thus an array of the model of every element of the mesh and the state and output vector of the MDM are given by

$$\mathbf{X}_\mathrm{m} = \left[\mathbf{x}_{\mathrm{m},(1,1)\,\mathrm{element}} \;\; \mathbf{x}_{\mathrm{m},(1,2)\,\mathrm{element}} \;\; \cdots \;\; \mathbf{x}_{\mathrm{m},(\mathrm{n}_{\mathrm{mesh}},\mathrm{n}_{\mathrm{mesh}})\,\mathrm{element}}\right]^T$$
$$\mathbf{Y}_\mathrm{m} = \left[\mathbf{y}_{\mathrm{m},(1,1)\,\mathrm{element}} \;\; \mathbf{y}_{\mathrm{m},(1,2)\,\mathrm{element}} \;\; \cdots \;\; \mathbf{y}_{\mathrm{m},(\mathrm{n}_{\mathrm{mesh}},\mathrm{n}_{\mathrm{mesh}})\,\mathrm{element}}\right]^T \qquad (3.6)$$

which are the state and output, respectively, of the machine dynamic for each element of the square mesh of the ingot. Equations of every element of the ingot square mesh in Eq. 3.1 are stacked to get

$$\frac{\mathrm{d}\mathbf{X}_\mathrm{m}(t)}{\mathrm{d}t} = \mathbf{F}_\mathrm{m}\left(\mathbf{X}_\mathrm{m}(t), \mathbf{u}_\mathrm{m}(t), t\right)$$
$$\mathbf{Y}_\mathrm{m}(t) = \mathbf{C}_\mathrm{m} \cdot \mathbf{X}_\mathrm{m}(t) + \mathbf{D}_\mathrm{m} \cdot \mathbf{u}_\mathrm{m}(t) \qquad (3.7)$$

where the input vector $\mathbf{u}_\mathrm{m}(t)$ remains unchanged since it applies to every element commonly. Thus, MDM consists of $n_{mesh}\times n_{mesh}$ state equations. In Eq. 3.7, the coefficient matrix $\mathbf{C}_\mathrm{m}$ for $\mathbf{X}_\mathrm{m}$ is a block diagonal one, in which c_m forms the non-zero block, with the dimension of $[n_{mesh}\times n_{mesh}, 5\times n_{mesh}\times n_{mesh}]$ to match the dimensions of the state and output vector, $[5\times n_{mesh}\times n_{mesh}, 1]$ as follows.

$$\mathbf{C_m} = \begin{bmatrix} \mathbf{c_m} & \mathbf{z} & \cdots & \mathbf{z} \\ \mathbf{z} & \mathbf{c_m} & \cdots & \mathbf{z} \\ \vdots & \vdots & \ddots & \vdots \\ \mathbf{z} & \mathbf{z} & \cdots & \mathbf{c_m} \end{bmatrix} \qquad (3.8)$$

where $\mathbf{z}$ is a zero row vector with 1×5 dimension. The coefficient matrix $\mathbf{D}_\mathrm{m}$ for $\boldsymbol{u}_\mathrm{m}$ is the zero matrix with the dimension of $[2\times n_{mesh}\times n_{mesh}, 2]$ to match the dimensions of the input and output vector, [2,1] and $[2\times n_{mesh}\times n_{mesh},1]$, respectively.

3.1.2. Deposition process model

In Chapter 2, a finite-element technique was utilized using 3-D CAD from which a mesh was generated including triangular or quadrilateral polygons. At the centroids of polygons, the computational model monitored the variation of the coating thickness in EB-PVD process. In the DPM, each polygon in the mesh will be considered and the all polygons will be combined into one model. The number of polygons (n_p) decides the size of final model and the computation time. The state vector, $\boldsymbol{x}_{\mathrm{d}}(t)$, of the DPM for a representative element consists of the coating thickness d_s. The research publications on the EB-PVD have focused on some understandings of the relationships between the process parameters of the EB-PVD and the microstructure and the properties of the coatings as shown in Fig. 1.1, from which the time rate of the microstructure change during the deposition can be naturally expected to depend on the applied process parameters. The process parameters shown in Fig. 1.1 are regarded as one of the states in the MDM. Therefore, an interconnection can be constructed between the MDM and the DPM, which carries the output $\mathbf{Y}_{\mathbf{m}}$ from the MDM to the input of the DPM. Thus, the system dynamic of the deposition process be expressed with an ordinary differential equation

$$\frac{\mathrm{d}\mathbf{x}_{\mathrm{d}}}{\mathrm{d}t} = \mathbf{f}_{\mathrm{d}}\left(\mathbf{x}_{\mathrm{d}}(t), \mathbf{Y}_{\mathrm{m}}(t), t\right) \quad (3.9)$$

where $\mathbf{f}_{\mathrm{d}}(\cdot)$ is a nonlinear function of $\mathbf{x}_{\mathrm{d}}(t)$, $\mathbf{Y}_{\mathrm{m}}(t)$, and t. The output vector, $\boldsymbol{y}_{\mathrm{d}}(t)$, of the DPM is the same as $\boldsymbol{x}_{\mathrm{d}}(t)$, so that the algebraic equations of the DPM in the state equation has similar form with Eq. 3.5 as follows.

$$\mathbf{y}_{\mathrm{d}}(t) = \mathbf{c}_{\mathrm{d}} \cdot \mathbf{x}_{\mathrm{d}}(t) + \mathbf{d}_{\mathrm{d}} \cdot \mathbf{Y}_{\mathrm{m}}(t) \quad (3.10)$$

where $\mathbf{c}_{\mathrm{d}} = [1]$ and $\mathbf{d}_{\mathrm{d}} = [0\ 0]$. As the same way in the MDM, the array of the state equation of every polygon becomes the complete DPM as follows.

$$\begin{aligned} \frac{\mathrm{d}\mathbf{X}_{\mathrm{d}}(t)}{\mathrm{d}t} &= \mathbf{F}_{\mathrm{d}}\left(\mathbf{X}_{\mathrm{d}}(t), \mathbf{Y}_{\mathrm{m}}(t), t\right) \\ \mathbf{Y}_{\mathrm{d}}(t) &= \mathbf{C}_{\mathrm{d}} \cdot \mathbf{X}_{\mathrm{d}}(t) + \mathbf{D}_{\mathrm{d}} \cdot \mathbf{Y}_{\mathrm{m}}(t) \end{aligned} \quad (3.11)$$

where

$$\begin{aligned} \mathbf{X}_{\mathrm{d}} &= \left[\mathbf{x}_{\mathrm{d,\,element\,1}}\ \mathbf{x}_{\mathrm{d,\,element\,2}}\ \cdots\ \mathbf{x}_{\mathrm{d,\,element\,n_p}}\right]^T \\ \mathbf{Y}_{\mathrm{d}} &= \left[\mathbf{y}_{\mathrm{d,\,element\,1}}\ \mathbf{y}_{\mathrm{d,\,element\,2}}\ \cdots\ \mathbf{y}_{\mathrm{d,\,element\,n_p}}\right]^T \end{aligned}.$$

Thus, n_p state equations compose the DPM. In Eq. 3.11, the coefficient matrix $\mathbf{C}_{\mathrm{d}}$ for $\mathbf{X}_{\mathrm{d}}$ is a $n_p \times n_p$ identity matrix to match the dimensions of the state and output vector, $[n_p, 1]$. The coefficient matrix $\mathbf{D}_{\mathrm{d}}$ for $\mathbf{Y}_{\mathrm{m}}$ is the zero matrix with the dimension of $[n_p, 2 \times n_{mesh} \times n_{mesh}]$ to match the dimensions of the input and output vector, $[2 \times n_{mesh} \times n_{mesh}, 1]$ and $[n_p, 1]$, respectively.

3.1.3. Substrate kinematics model

This SKM is computationally efficient for modeling the kinematics of substrate and manipulator motion which critically affects the microstructure of coating layers (Yamaguchi et al. 2003). The basic idea behind the SKM method is adopted from the coordinate transformation techniques in the robotics which computes the location and orientation of various points of the robot-arm system (Craig 1989). Junker et al. (2004) facilitated state space formulation to develop a deposition model for physical vapor

deposition onto a moving 2-D substrate, resulting in a significant rise in the computational speed. Based on this linear algebra, the EB-PVD process for a moving 3-D substrate can also be expressed in the lumped linear state space formulation based on the discrete-time system as follows:

$$\begin{aligned} \mathbf{X_k}(k+1) &= \mathbf{A_k X_k}(k) + \mathbf{B_k U_k}(k) \\ \mathbf{Y_k}(k) &= \mathbf{C_k X_k}(k) + \mathbf{D_k U_k}(k) \end{aligned} \tag{3.12}$$

where k is the integer ranging from 0 to $+\infty$, illustrating the time $t = k\tau$ where τ is the sampling time.

First, the centroid of a polygon can be expressed by a 3-dimensional vector $\mathbf{s}$ (s_1, s_2, s_3) in Euclidian 3-space; the outward normal unit vector can be expressed by a 3-dimensional vector $\mathbf{u}$ (u_1, u_2, u_3). In the EB-PVD process with companion of substrate manipulation, there are two kind of causes for the change of spatial information of the substrate: one is the substrate manipulation, expressed as $\mathbf{s}^m$, and the other the deposition changing the coating thickness, expressed as $\mathbf{s}^d$. This vector manipulation is depicted in Fig. 3.3.

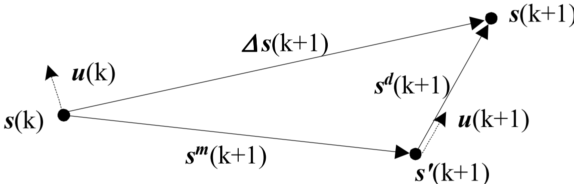

Figure 3.3. The change of spatial vector by kinematics and deposition

As shown in Fig. 3.3, the relationship of the spatial vector **s**(k) of a centroid of polygon of 3D substrate at any time *k* with the spatial vector **s**(k+1) of a centroid of polygon of 3D substrate after a sampling time τ can be expressed as follows.

$$\mathbf{s}(k+1)=\mathbf{s}(k)+\mathbf{s}^{m}(k+1)+\mathbf{s}^{d}(k+1) \qquad (3.13)$$

where $\mathbf{s}'(k+1)=\mathbf{s}(k)+\mathbf{s}^{m}(k+1)$.

According to Halnan and Lee (1983), various part holders has been used in EB-PVD: single part holder and multi parts holder with angular offset of parts. Therefore, for the SKM to cope with the various part holder systems which result in generating various modes of the substrate manipulation, multi-link transformation with the operations such as translation and rotation should be considered. In this Chapter, the right-handed coordinate system is chosen; a frame which accompanies the manipulation of substrate or link is assumed that its –z-axis is in accordance with the longitudinal of the substrate or the link. Then, the substrate is located along –z-axis at the origin of the local frame that is attached to the end of the multi-link so that the direction of angular velocity measured in RPM is identical with z-axis of the local frame. The description of the initial spatial vector of any point of the substrate will be relative to the local frame where the substrate is attached. The information needed to describe a frame relative to a frame $\{A\}$ is a 3×3 rotation matrix with the notation ${}^{A}_{B}\mathbf{R}$ and a position vector with the notation ${}^{A}\mathbf{s}_{BO}$ which locates the origin of the frame $\{A\}$. When the unit vectors of a coordinate system $\{i\}$ is denoted as $\hat{x}_i$, $\hat{y}_i$, and $\hat{z}_i$, each component of ${}^{A}_{B}\mathbf{R}$ can be written as the dot product of a pair of unit vectors of {A} and {B} as

$$ {}_{B}^{A}\mathbf{R} = \begin{bmatrix} \hat{x}_B \cdot \hat{x}_A & \hat{y}_B \cdot \hat{x}_A & \hat{z}_B \cdot \hat{x}_A \\ \hat{x}_B \cdot \hat{y}_A & \hat{y}_B \cdot \hat{y}_A & \hat{z}_B \cdot \hat{y}_A \\ \hat{x}_B \cdot \hat{z}_A & \hat{y}_B \cdot \hat{z}_A & \hat{z}_B \cdot \hat{z}_A \end{bmatrix} \quad (3.14) $$

Notice that ${}^{A}\mathbf{s}_{BO}$ and the unit vectors of the frame $\{B\}$ should be described with respect to the frame $\{A\}$. As said before, the position vector of a point on the substrate was at first described with respect to the local frame at the end of the multi-link. Therefore, it is needed to know its description with respect to the universe frame of the EB-PVD coater, which usually has the universe origin at the center of one of ingots with z = 0. This mapping of the description of position vector relative to the frame {B} involving the frame $\{A\}$ can be expressed as follows.

$$ {}^{A}\mathbf{s} = {}_{B}^{A}\mathbf{R}\,{}^{B}\mathbf{s} + {}^{A}\mathbf{s}_{BO} \quad (3.15) $$

where ${}^{A}\mathbf{s}$ and ${}^{B}\mathbf{s}$ are the description of a point relative to $\{A\}$ and $\{B\}$, respectively. With more appealing conceptual form, the form of Eq. 3.15 can be changed to the more compact equation which defines a 4×4 matrix operator and use 4×1 position vectors as follows:

$$ \begin{bmatrix} {}^{A}\mathbf{s} \\ \cdots \\ 1 \end{bmatrix} = \begin{bmatrix} {}_{B}^{A}\mathbf{R} & \vdots & {}^{A}\mathbf{s}_{BO} \\ \cdots & \cdots & \cdots \\ 0\ 0\ 0 & \vdots & 1 \end{bmatrix} \begin{bmatrix} {}^{B}\mathbf{s} \\ \cdots \\ 1 \end{bmatrix}. \quad (3.16) $$

where the 4×4 matrix is called a transformation operator with the notation of ${}_{B}^{A}\mathbf{T}$. In the case that a frame is assigned in the position corresponding to the manipulation such as rotation and translation, it is just needed to change ${}_{B}^{A}\mathbf{R}$ for the rotation and ${}^{A}\mathbf{s}_{BO}$ for the translation. Since the assumption mentioned above about the frame corresponding to the

manipulation, it is needed to consider only rotation and translation about z-axis of the frame and the rotation matrix and position vector are given by

$$ {}^{A}_{B}\mathbf{R} = \begin{bmatrix} \cos(\theta) & -\sin(\theta) & 0 \\ \sin(\theta) & \cos(\theta) & 0 \\ 0 & 0 & 1 \end{bmatrix}, \quad {}^{A}\mathbf{s}_{BO} = [0\ 0\ \lambda]^T. \tag{3.17} $$

where θ and λ are the rotation angle and the translation distance of the substrate during a sampling time interval, respectively. Once the link frames have been defined based on the way explained above, the link transformations can be multiplied together to find a single transformation that relates the end frame {*N*} with respect to which the position of the substrate will be described to frame {*0*} defining the universe origin of the EB-PVD coater:

$$ {}^{0}_{N}\mathbf{T} = {}^{0}_{1}\mathbf{T}\,{}^{1}_{2}\mathbf{T}\,{}^{2}_{3}\mathbf{T} \cdots {}^{N-1}_{N}\mathbf{T}. \tag{3.18} $$

The change of the Cartesian position of a centroid of the substrate by the substrate manipulation at time k+1 can be computed by ${}^{0}_{N}\mathbf{T}$. Thus, the $\mathbf{s}'(k+1)$ shown in Fig. 3.3 can be calculated as follows:

$$ \mathbf{s}'(k+1) = {}^{0}_{N}\mathbf{T}\mathbf{s}(k). \tag{3.19} $$

Notice that a position vector is 3×1 or 4×1 depending on where it appears multiplied by a 3×3 matrix or 4×4 matrix so that $\mathbf{s}'(k+1)$ and $\mathbf{s}(k)$ in Eq. 3.19 are 4×1 vectors which have 1 as the last element.

The change of position vector of the substrate by deposition, expressed as $\mathbf{s}^{d}(k+1)$ in Fig. 3.3, can be derived from the output $\mathbf{y}_{\mathrm{d}}$ of previous DPM in Eq. 3.10,

which means the increase of coating thickness at time t. Since the SKM develops the discrete-time system, the output $\mathbf{y}_{\mathrm{d}}(k)$ of the DPM at the time k can be calculated by the Riemann integral from $k\tau$ to $(k+1)\tau$. Then, $\mathbf{y}_{\mathrm{d}}(k)$ means the norm of the vector $\mathbf{s}^{d}(k+1)$ so that the assumption that the unit vector of $\mathbf{s}^{d}(k+1)$ is identical to the outward normal vector $\mathbf{u}(k)$ of the point at time k will yield

$$\mathbf{s}^{d}(k+1) = y_{d}(k)\mathbf{u}(k). \tag{3.20}$$

Substituting Eq. 3.19 and 3.20 into Eq. 3.13 yields

$$\mathbf{s}(k+1) = {}_{N}^{0}\mathbf{T}\mathbf{s}(k) + y_{d}(k)\mathbf{u}(k). \tag{3.21}$$

Notice that a normal unit vector is 3×1 or 4×1 depending on where it appears with a 3×3 matrix or 4×4 matrix so that $\mathbf{u}(k)$ in Eq. 3.21 are 4×1 vectors which have 0 as the last element to match the dimension of the position vector $\mathbf{s}(k)$. Since the movement of a substrate changes the normal unit vector $\mathbf{u}(k)$ of a polygon in the same way that it changes the position vector of the centroid of the polygon, the normal unit vector $\mathbf{u}(k)$ can be obtained similarly with Eq. 3.19. To use the transformation ${}_{N}^{0}\mathbf{T}$ in Eq. 3.18, a new vector $\mathbf{w}$ that represents the head of the normal unit vector of a position vector should be considered. It is obtained by adding the two vectors, the normal unit vector $\mathbf{u}$ and the position vector $\mathbf{s}$. Substituting $\mathbf{w}$ with $\mathbf{s}$ in Eq. 3.19 yields

$$\mathbf{w}(k) = {}_{N}^{0}\mathbf{T}\mathbf{w}(k-1). \tag{3.22}$$

where $\mathbf{w}(k)$ and $\mathbf{w}(k-1)$ are 4×1 vectors which have 1 as the last element. Then, the normal unit vector $\mathbf{u}(k)$ can be obtained by taking the difference between $\mathbf{w}(k)$ and $\mathbf{s}(k)$ as follows:

$$\mathbf{u}(k) = \mathbf{w}(k) - \mathbf{s}(k). \qquad (3.23)$$

The state vector $\mathbf{X_k}$ of the SKM is defined as a column vector with the dimension of [4×n_p, 1], where the elements of $\mathbf{s}$ of n_p centroids are sequentially stacked from the centroid *1* to the centroid n_p with the addition of 1 as the fourth element of every centroid, as follows:

$$\mathbf{X_k} = \left(s_1^1 \;\; s_2^1 \;\; s_3^1 \;\; 1 \;\; s_1^2 \;\; s_2^2 \;\; s_3^2 \;\; 1 \;\; \cdots \;\; s_1^{n_p} \;\; s_2^{n_p} \;\; s_3^{n_p} \;\; 1\right)^T \qquad (3.24)$$

where the superscript of elements means the index of a centroid. In the same way of generating $\mathbf{X_k}$ shown in Eq. 3.24, the input vector $\mathbf{U_k}$ of the SKM is defined as a [4×n_p, 1] column vector by sequentially stacking the 4×1 outward normal unit vector of from centroid *1* to centroid n_p as follows:

$$\mathbf{U_k} = \left(u_1^1 \;\; u_2^1 \;\; u_3^1 \;\; 1 \;\; u_1^2 \;\; u_2^2 \;\; u_3^2 \;\; 1 \;\; \cdots \;\; u_1^{n_p} \;\; u_2^{n_p} \;\; u_3^{n_p} \;\; 1\right)^T. \qquad (3.25)$$

To make a discrete state equation for the SKM, a block diagonal matrix $\mathbf{A}_\mathrm{k}$ with the dimension of [4×n_p, 4×n_p] is defined using Eq. 3.21 as follows:

$$\mathbf{A_k} = \begin{bmatrix} {}^{0}_{N}\mathbf{T} & \mathbf{Z} & \cdots & \mathbf{Z} \\ \mathbf{Z} & {}^{0}_{N}\mathbf{T} & \cdots & \mathbf{Z} \\ \vdots & \vdots & \ddots & \vdots \\ \mathbf{Z} & \mathbf{Z} & \cdots & {}^{0}_{N}\mathbf{T} \end{bmatrix} \qquad (3.26)$$

where $\mathbf{Z}$ is a zero matrix with the dimension of [4, 4]. From Eq. 3.20 and 3.22, the coefficient matrix $\mathbf{B}_\mathrm{k}$ of the input vector $\mathbf{U_k}$ of the SKM is given by

$$\mathbf{B_k} = \begin{bmatrix} \mathbf{Y_d}_N^{1^0}\mathbf{T} & \mathbf{Z} & \cdots & \mathbf{Z} \\ \mathbf{Z} & \mathbf{Y_d}_N^{2^0}\mathbf{T} & \cdots & \mathbf{Z} \\ \vdots & \vdots & \ddots & \vdots \\ \mathbf{Z} & \mathbf{Z} & \cdots & \mathbf{Y_d}_N^{n_p{}^0}\mathbf{T} \end{bmatrix} \tag{3.27}$$

where

$$\mathbf{Y_d^i} = \begin{bmatrix} y_d^i & 0 & 0 & 0 \\ 0 & y_d^i & 0 & 0 \\ 0 & 0 & y_d^i & 0 \\ 0 & 0 & 0 & 1 \end{bmatrix},$$

and the superscript of $\boldsymbol{Y_d}$ means the index of a centroid.

The in-situ sensor measurements using the conventional sensors such as thermocouples and quartz crystal microbalances (QCM) can provide in-situ surface measurements of such as temperature and coating thickness, respectively, in real time. The QCM can read the change in crystal thickness due to the change in resonance frequency (Mahan 2000) using the relationship given by

$$\Delta d = -\Delta f_r \cdot \frac{v_{tr}}{2 f_r^2} \tag{3.28}$$

where Δd is the change in the crystal thickness, Δf_r is the change in resonance frequency, f_r is a resonance frequency, and v_{tr} is the velocity of an elastic transverse wave, 3.340×10^3m/s for “ATC” quartz crystals. When multiple QCM are employed in the EB-PVD coater, they enable simultaneously monitoring the coating thicknesses at multiple sites. Let us consider, for simplicity, n_q QCMs equipped on the centroid of polygons of the substrate, where $n_p \geq n_q$. Considering 3×1 position vector for convenience, the output vector $\mathbf{Y}_\mathrm{k}$ of the SKM shown in Eq. 3.12 has the dimension of $3n_q\times1$. Then, the

coefficient matrix $\mathbf{C}_k$ for $\mathbf{X}_k$ is a $3n_q \times 4n_p$ matrix to match the dimensions of the state and output vector and given by

$$\mathbf{C_k} = \begin{bmatrix} \Delta_{11} & \Delta_{12} & \cdots & \Delta_{1n_p} \\ \Delta_{21} & \Delta_{22} & \cdots & \Delta_{2n_p} \\ \vdots & \vdots & \ddots & \vdots \\ \Delta_{n_q 1} & \Delta_{n_q 2} & \cdots & \Delta_{n_q n_p} \end{bmatrix} \text{and } \Delta_{ij} = \begin{bmatrix} \delta_{ij} & 0 & 0 & 0 \\ 0 & \delta_{ij} & 0 & 0 \\ 0 & 0 & \delta_{ij} & 0 \end{bmatrix} \quad (3.29)$$

where $\delta_{ij} = 1$ when the *i*-th QCM is equipped on the *j*-th centroid and, otherwise, $\delta_{ij} = 0$ for i = 1,…, n_q and j = 1,…, n_p. The coefficient matrix $\mathbf{D}_k$ for $\mathbf{U}_k$ is the zero matrix with the dimension of [$3n_q$, $4n_p$] to match the dimensions of the input and output vector, [$4n_p$, 1] and [$3n_q$, 1], respectively.

3.2. Process simulation

In this Chapter, the dynamic simulation of the EB-PVD process uses the more advanced model for the substrate kinematics in addition to the computational model in Chapter 2; the SKM enables to simulate the substrate kinematics modes that various substrate holders can generate in the real deposition process. For example, in the case of a single part holder, a substrate can be thought of as a link with a cylindrical joint, which has only one degree of freedom, in the end. On the other hand, in the case of a set of parts holder which has two rotation modes at both a main shaft and a substrate holder, a substrate is assigned the angular offset. It can be thought of as a three-link connected with a fixed revolute joint and two cylindrical joints which two degrees of freedom with respect to rotation and translation. Since the deposition process depends on the substrate kinematics as well as the machine dynamics, the coating thickness, which is the output of

the DPM, also will be affected by the line-of-sight of an interested point that can be judged by a ray casting algorithm by Fuke et al. (2005). By comparison with the experimental data, the simulation tool helps validate the feasibility of the proposed model and with increasing the reliability of the EB-PVD process models with low-cost computing, the simulation tool enables optimized process planning including process parameters and substrate kinematics planning.

The flowchart of the EB-PVD computational model with an advanced substrate kinematics model is depicted in Fig. 3.4. An implementation of the unified model of the EB-PVD process described in the previous section in Matlab on a PC cluster LION-XO of Penn State' ASET has been developed.

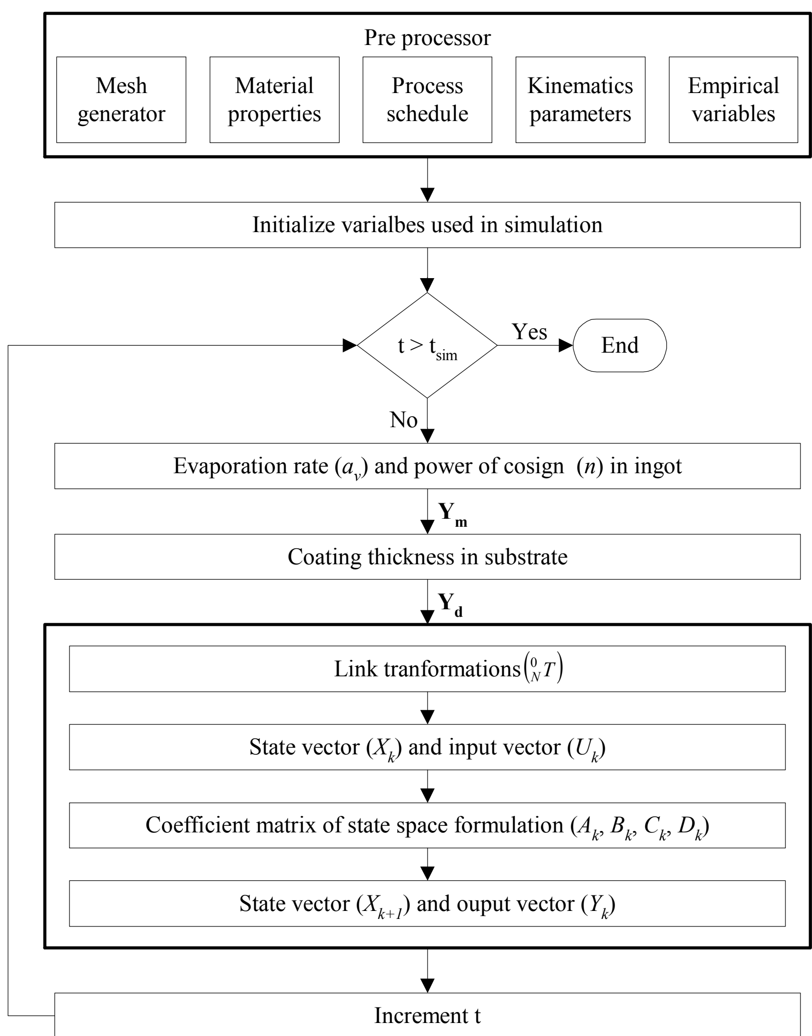

Figure 3.4. The flowchart of the EB-PVD computational model

The first pre-processor shown in Fig. 3.4 functions as an input module which collects the data: the geometry of substrate and ingot, material properties, EB-PVD process schedule, such as EB-Gun parameters, kinematics parameters, and empirical variables, such as evaporation factor, vapor scattering factor, and condensation factor. The EB-PVD computational model utilizes those inputs to calculate the coating thickness on the surface elements of a substrate. Mesh generator shown in the pre processor will

generate from a 3-D CAD model of the substrate the nodes and their inter-connectivity to approximate the surface of the substrate by a set of connected triangular or quadrilateral polygons, and centroids, which are points of interest on these polygons, where the coating thickness needs to be monitored. Before starting the main procedures, variables used in the simulation will be initialized. The procedure of the computational model will be finished when the desired duration of simulation, t_{sim}, is satisfied. Machine dynamic model composing several state variables in Eq. 3.3 derives the evaporation rate (a_v) and the power of cosine (n), or the beam collimation parameter, of every element in the ingot mesh. These combine into the output vector $\mathbf{Y_m}$. The power of cosine in the $\mathbf{Y_m}$ will determine the vapor plume shape and in turn, the deposition rate across a substrate.

Next, the deposition process model using the information in $\mathbf{Y_m}$ will calculate the coating thickness across substrate elements. In this procedure, it is important to calculate the visibility of every substrate element from the ingots using a ray-casting algorithm. The coating thicknesses of the substrate elements combine into an output vector $\mathbf{Y_d}$ that is used by the SKM to calculate the spatial data of the substrate. In the SKM, the link transformation will be generated based on the parameters of rotation and translation. Next, the state and input vector, X_k and U_k, respectively, will be calculated; the coefficient matrix of the state equation will be produced using the link transformation and $\mathbf{Y_d}$. By solving the state equation in the matrix formulation, the state vector X_{k+1} and the output vector Y_k will be computed, resulting the cumulative coating thickness at all the points of interest till current time. Increasing the time by a time step τ and comparing it with t_{sim} complete the iteration loop of the computational model.

3.3. Case study

Simulation results are presented for a turbine blade shown in Fig. 3.5. This substrate was chosen to validate that the proposed computational model can predict the coating thickness on a complex shape like a turbine blade as well as a simple shapes presented in Chapter 2. To digitize the geometry of the turbine blade for the simulation, the point cloud of the turbine blade was generated using Zeiss Eclipse coordinate measurement machines (CMM), and then 3D mesh was produced as shown in Fig. 3.6. In the mesh, the addendum shape was simplified to be box-shaped.

Figure 3.5. The turbine blade

Figure 3.6. The digitization of the turbine

To evaluate the performance of the proposed SKM and to investigate the effects of the kinematics parameters on the EB-PVD process, two substrate holders and their link systems were selected as detailed in Fig. 3.7, where heavy-weight lines correspond to the link and italic characters in rectangular box are the substrate kinematics parameters.

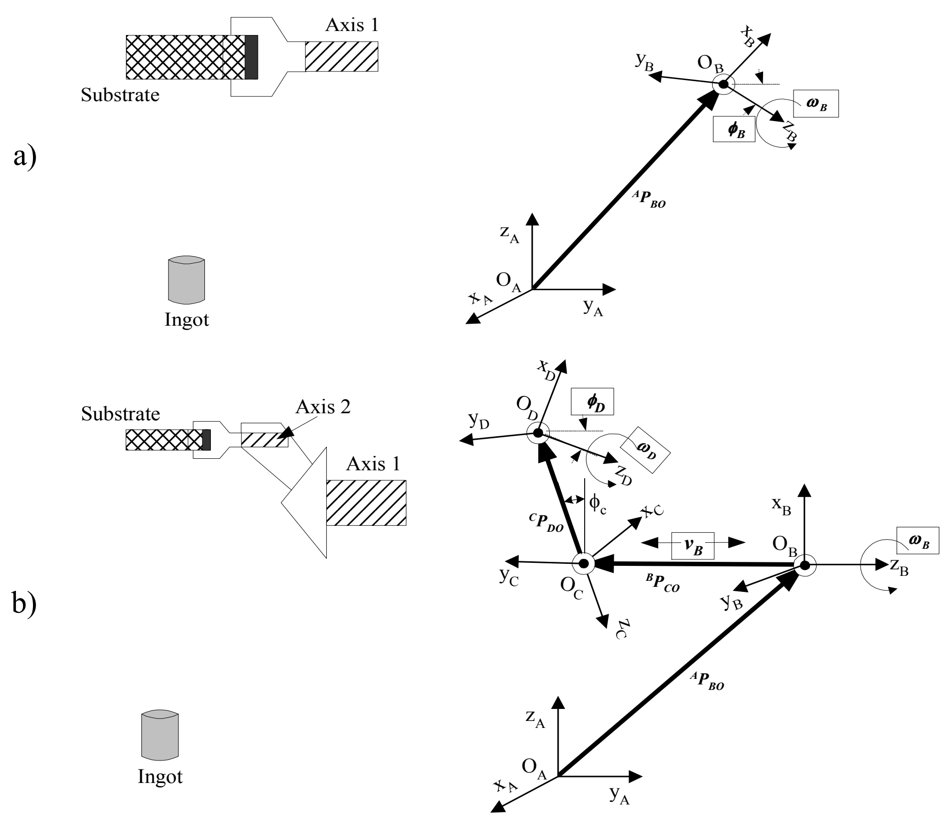

Figure 3.7. Schematic drawing of two substrate holders with their link system: a) One-axis Holder, b) Two-axis Holder

One-axis Holder shown in Fig. 3.7(a) has only one degree of freedom with respect to rotation; in Two-axis Holder shown in Fig. 3.7(b), only first and third of three joints have two degrees of freedom with respect to rotation and translation, and one degree of freedom with respect to rotation, respectively. The variables inside the rectangular box in

Fig. 3.7 were selected as the substrate kinematics parameters, which are called factors of the experiment.

According to Averill et al. (1982), an experimental design can provides a way of deciding beforehand which particular system variants to simulate so that the desired information can be obtained at minimal cost, i.e., with the least amount of simulating. It can be thus more efficient than a sequence of runs in which a number of alternative systems are tried unsystematically to see what happens. In addition, the designs of experiments can be particularly useful in the early stages of experimentation when we are pretty much in the dark about which factors are important and how they might affect the measure of performance, called the response. Therefore, a statistical experimental design is used to study which factors of the substrate kinematics really matter and how they affect the response.

The values of the constant substrate parameters used in the simulation are summarized in Table 3.1. Notice that there is a limitation of translation so that ±60 mm along the z_B axis was selected as the alternate length, which corresponds to one third of the length of the turbine blade's main body.

Table 3.1. Constant kinematics parameters

Kinematics Parameters (*unit*)	One-axis Holder	Two-axis Holder
${}^{A}P_{BO}$ (mm)	$[0\ 182.7846\ 500]$	$[0\ 432.7846\ 600]$
${}^{B}P_{CO}$ (mm)	-	$[0\ 0\ -200]$
θ_C $(^o)$	-	30
${}^{C}P_{DO}$ (mm)	-	$[0\ 0\ -100]$

According to Cho et al. (2005), there are the five prime objectives in an EB-PVD coating processing: minimizing the amount of material evaporated, achieving the minimum coating thickness, maximizing the amount of evaporated material deposited on the substrate, minimizing the coating time, and uniformity of coating thickness. They proposed three metrics to quantify those objectives. One is the sum of coating thicknesses at all the control points to measure the amount of material deposited on the substrate, $M(t_{sim})$. Second is the variance of coating deposition thickness at the control points to measure of coating uniformity, $v(t_{sim})$. Third is the minimum coating thickness over the entire substrate to measure the achievement a minimum coating thickness at any point on the substrate, $d_{min}(t_{sim})$; those can be expressed as follows:

$$\begin{aligned} M(t_{sim}) &= \sum_{i=1}^{n_p} d_s^i(t_{sim}) \\ v(t_{sim}) &= \frac{1}{n_p}\sum_{i=1}^{n_p}\left(\frac{M(t_{sim})}{n_p} - d_s^i(t_{sim})\right)^2 \\ d_{\min}(t_{sim}) &= \min\left\{d_s^1(t_{sim}), d_s^2(t_{sim}), \cdots, d_s^{n_p}(t_{sim})\right\} \end{aligned} \tag{3.30}$$

where $d_s^i(t_{sim})$ is the coating deposition thickness at the i-th control point after the simulation period t_{sim}. These three metrics in Eq. 3.30 are calculated from the coating thickness and adopted as the response of the experimental design. The selected factors of the experimental design (with their units), depicted in Fig. 3.7, and their values, or levels, are listed in Table 3.2.

Table 3.2. Factors and levels for the experimental design

Kinematics Parameters (unit)		One-axis Holder			Two-axis Holder		
		Lower	Center	Upper	Lower	Center	Upper
ω_B (*RPM*)	RPMB	1	10	20	1	10	20
φ_B (^{o})	OffsetAngleB	0	15	30	-	-	-
v_B (*m*/*min*)	TranVel	-	-	-	0	0.5	1
ω_D (*RPM*)	RPMD	-	-	-	0	10	20
φ_D (^{o})	OffsetAngleD	-	-	-	0	15	30

In both kinematics modes a three-level full factorial design was used so that each factor is coded to the levels lower, center, upper as shown in Table 3.2. Since One-axis Holder has only one degree of freedom with respect to the rotation along z_B shown in Fig. 3.7, the rotation speed ω_B, called as 'RPMB', is selected as a factor of the experiment for One-axis Holder. The offset angle of z_B, called as 'OffsetAngleB', shown in Fig. 3.7 with respect to the horizon is also selected as another factor of the experiment for One-axis Holder.

In contrast to the One-axis Holder, Two-axis Holder has more degree of freedom than One-axis Holder does. That is, as shown in Fig. 3.7, there are two degree of freedom with respect to the rotation and the translation along z_B, and there is one degree of freedom with respect to the rotation along z_D. Therefore, the rotation speed ω_B, the translation velocity v_B, called as 'TranVel', and the rotation speed ω_D, called as 'RPMD', are selected as factors of the experiment for Two-axis Holder. The offset angle of z_D, called as 'OffsetAngleD', shown in Fig. 3.7 with respect to the horizon is also selected as another factor of the experiment while the offset angle of z_B, is ignored for Two-axis

Holder. This means that the z_B-axis remains parallel to the horizon without any inclination for Two-axis Holder. The maximum of the two rotation speeds ω_B and ω_D is set to be 20rpm as the experiments by Yamaguchi et al. (2003).

Since the three-level full factorial design requires simulation runs at each of the 3^m possible combinations of factor levels, where *m* means the number of factors of the experimental design, a two-factor experiment for One-axis Holder requires 9 simulation runs while a four-factor experiment for Two-axis Holder requires 81 simulation runs.

As a coating material ingot, the YSZ was chosen to be deposited on the turbine blade because it is used as the basis of the majority of today's TBCs for aircraft engines (Yamaguchi et al. 2003). The themophysical properties of YSZ that is required by the MDM, summarized by Simon and Pal (1999), was applied in the experiment; all properties in Table 2.1 are corrected for the YSZ. Machine process parameters and empirical parameters used in the simulation runs are summarized in Table 3.3.

Table 3.3. Parameters used in the simulation of YSZ deposition on turbine blade

Machine parameters	Empirical parameters
Ingot height = 500 mm	Variance of white noise of current and voltage = 0.01
Cathode heating efficiency η_A=3.0 mA/W	Initial temperature of ingot and crucible = 298.15 K
EB diameter = 3 mm	Evaporation coefficient (αv) = 1 (ideal evaporation)
EB Scan pattern = Swirl	Vapor flux scattering coefficient = 1 (no scatter)
# of circulation of beam scan = 5	Condensation coefficient = 1 (ideal condensation)
Current of EB Gun = 45 A	Time step = 0.05 sec
Voltage of EB Gun = 1000 V	
Acceleration voltage U_B = 10 kV	

For the machine parameters, there are inputs for the MDM such as current and voltage of EB gun, cathode heating efficiency, electron beam diameter, scan pattern and its parameter (# of circulation of beam scan), and acceleration voltage. For empirical parameters, there are inputs for both the MDM and DPM such as variance of white noise of current and voltage in EB gun, initial temperature of ingot and crucible, vapor flux scattering coefficient, and condensation coefficient.

The proposed computational model will give deterministic outputs. That is, the computational experiments return identical observations with the same inputs. Then, the coating thickness predicted by the proposed computational model will be not randomly varied while it will only depend on the level of the factors of the experimental design. Therefore, it is assumed that the results are real and not being explained by random fluctuation, resulting that the replication number of the experiment design is set to be 1. In all simulation runs, the process time (t_{sim}) was setup as 60 sec because it is the minimum time for a substrate assigned by 1 RPM to finish one rotation. Figure 3.8 shows the screenshot of the simulator in Matlab.

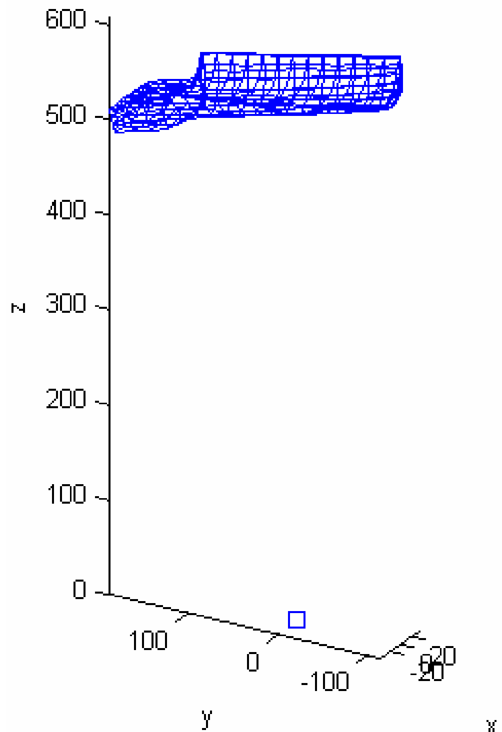

Figure 3.8. The screenshot of the simulator using Matlab

3.3.1. One-axis Holder

From each of 9 simulation runs, the coating thicknesses on n_p polygons of the turbine blade mesh shown in Fig. 3.6 are calculated by the proposed computational model, from which the responses of the 3^2 full factorial design, $M(t_{sim})$, $v(t_{sim})$, and $d_{min}(t_{sim})$, are computed by Eq. 3.30.

Figure 3.9 shows main effect plots using the data means for $M(t_{sim})$, $v(t_{sim})$, and $d_{min}(t_{sim})$ in One-axis Holder, where RPM and Offsetangle mean the rotation velocity ω_B and the offset angle φ_B, shown in Fig. 3.7, respectively. The main effect of a factor is defined as the change in the average response due to moving the factor from a level to another level. The x-axis of a main effect plot is the level of factors from lower to center

to upper. That is, 1, 2, and 3 in the x-axis refer to lower level, center level, and upper level, respectively. In the y-axis of the main effect plot, each response is normalized to plot.

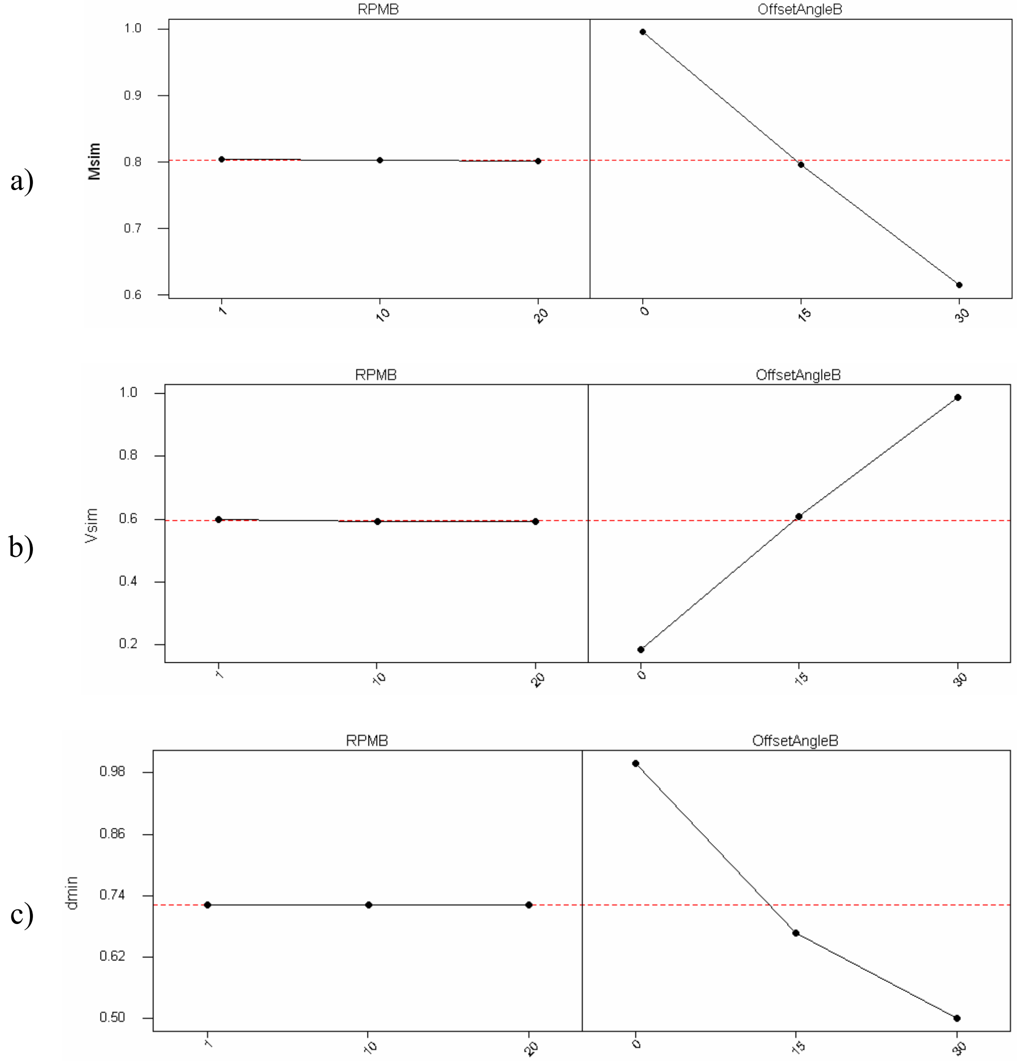

Figure 3.9. Main effect plots for a) $M(t_{sim})$, b) $v(t_{sim})$, c) $d_{min}(t_{sim})$ in One-axis Holder

In all the three responses shown in Fig. 3.9, the normalized main effects are almost same for RPM. That is, the average effect of raising RPM for One-axis Holder

from lower level to center or upper level will not change the responses such as $M(t_{sim})$, $v(t_{sim})$, and $d_{min}(t_{sim})$. This indicates that the change of the rotation velocity ω_B for the One-axis Holder can not change the process efficiency of the EB-PVD measured by the responses such as $M(t_{sim})$, $v(t_{sim})$, and $d_{min}(t_{sim})$ and that the rotation velocity ω_B is statistically insignificant for the One-axis Holder. This supports the experiment results by Yamaguchi et al. (2003), where the substrate manipulation decreases the deposition rate compared to stationary deposition condition but there was no difference in the deposition rate among three levels of the rotation speed. Contrary to the rotation speed ω_B, the change of the offset angle φ_B for One-axis Holder changed the responses of the experimental designs. That is, as the level of the offset angle φ_B increased by one level, the normalized main effect for OffsetAngleB decreased up to about 25% in the $M(t_{sim})$ and about 30% in the $d_{min}(t_{sim})$ while that increased up to about 65% in the $v(t_{sim})$. Thus, it appears that the smaller value of the offset angle φ_B would be preferable, since the objectives are to maximize $M(t_{sim})$ and $d_{min}(t_{sim})$ and to minimize $v(t_{sim})$.

To check the effect of the interaction between RPMB and OffsetAngleB on the three responses, interaction plots were generated using Minitab as shown in Figure 3.10. As can be seen from the plots, there is no significant interaction between the rotation speed ω_B and the offset angle φ_B in One-axis Holder.

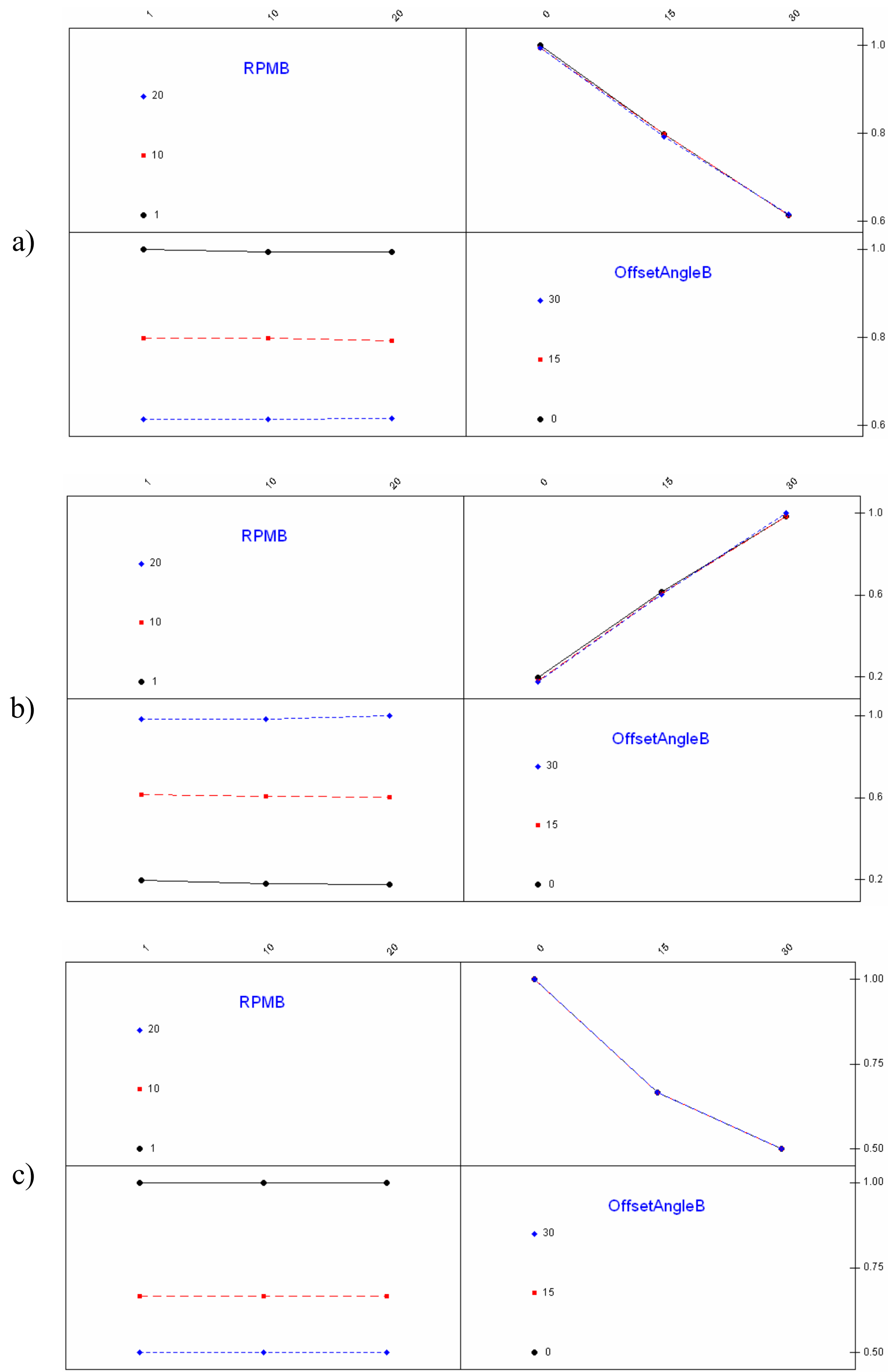

Figure 3.10. Interaction plot for a) $M(t_{sim})$, b) $v(t_{sim})$, c) $d_{min}(t_{sim})$ in One-axis Holder

Since the interaction effect between RPMB and OffsetAngleB is not significant for the three responses in One-axis Holder, it was pooled with the error term for a reduced linear regression model; analysis of variance (ANOVA) for the three responses was performed using reduced linear regression model with Minitab. The results are summarized in Table 3.4-3.6.

Table 3.4. Analysis of Variance for reduced model of $M(t_{sim})$

Source	DF	SS	MS	F	P
RPMB	2	0.0000092	0.0000046	0.53	0.626
OffsetAngleB	2	0.2180943	0.1090471	1.30E+04	0
Error	4	0.0000347	0.0000087		
Total	8	0.2181382			

Table 3.5. Analysis of Variance for reduced model of $v(t_{sim})$

Source	DF	SS	MS	F	P
RPMB	2	0.0000825	0.0000412	0.45	0.668
OffsetAngleB	2	0.9738419	0.4869209	5.29E+03	0
Error	4	0.0003684	0.0000921		
Total	8	0.9742928			

Table 3.6. Analysis of Variance for reduced model of $d_{min}(t_{sim})$

Source	DF	SS	MS	F	P
RPMB	2	0	0	0	1
OffsetAngleB	2	0.3888889	0.1944444	1.40E+16	0
Error	4	0	0		
Total	8	0.3888889			

From Table 3.4-3.6, the F and P values of OffsetAngleB for the three responses are greater than 1000 and zero, respectively. The P values of RPMB for the three

responses are greater than 0.05. This implies that only OffsetAngleB is statistically significant with 95% confidence. This agrees well with the results of the main effect plots shown in Fig. 3.9.

3.3.2. Two-axis Holder

As in the experiment for One-axis Holder, the coating thicknesses on n_p polygons of the turbine blade mesh shown in Fig. 3.6 are calculated by the proposed computational model from each of 81 simulation runs. Then, the responses of the 3^4 full factorial design, $M(t_{sim})$, $v(t_{sim})$, and $d_{min}(t_{sim})$, are computed by Eq. 3.30 from the predicted coating thicknesses.

Figure 3.11 shows main effect plots using the data means for $M(t_{sim})$, $v(t_{sim})$, and $d_{min}(t_{sim})$ in Two-axis Holder, where RPMB, TranVel, RPMD, and OffsetangleD mean the rotation velocity ω_B, the translation velocity v_B, the rotation speed ω_D, and the offset angle φ_D, shown in Fig. 3.7, respectively. As in Fig. 3.9, 1, 2, and 3 in the x-axis refer to lower level, center level, and upper level, respectively. In the y-axis of the main effect plot, each response is normalized to plot as well.

Contrary to the results in One-axis Holder, the amount of material deposited on the substrate $M(t_{sim})$ decreases linearly with increasing the rotation speed ω_B (RPMB) as shown in Fig. 3.11 (a). This is expected since the increase of the rotation speed along z_B causes the turbine blade to deviate more and more from the center of a vapor plume. The coating uniformity, $v(t_{sim})$ and the minimum coating thickness $d_{min}(t_{sim})$ are also decrease

as RPMB increases over the center level. However, Fig. 3.11 (b) and (c) show that the quadratic effect of the RPMB on $v(t_{sim})$, and $d_{min}(t_{sim})$ in Two-axis Holder is significant.

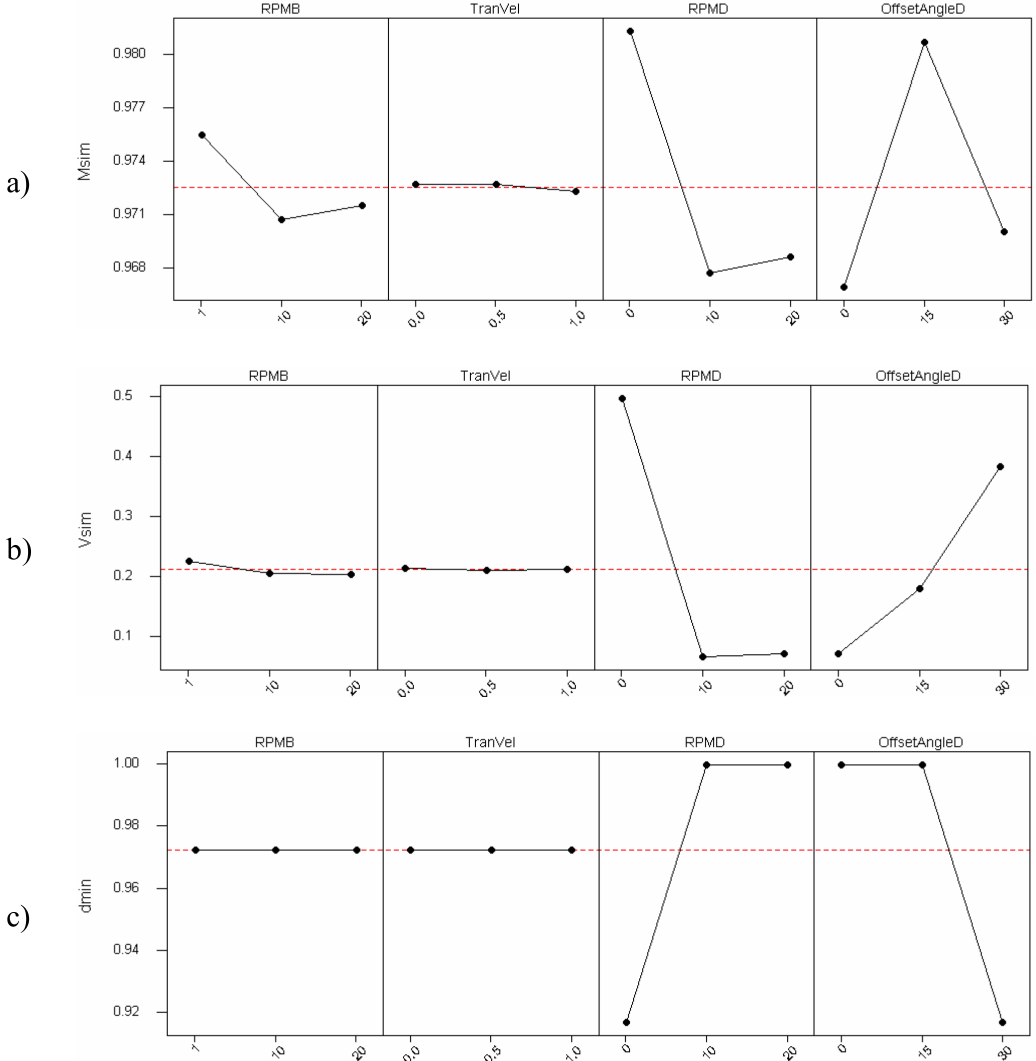

Figure 3.11. Main effect plots for a) $M(t_{sim})$, b) $v(t_{sim})$, c) $d_{min}(t_{sim})$ in Two-axis Holder

In all the three responses shown in Fig. 3.11, the normalized main effects are almost same for TranVel. That is, the average effect of raising the translation velocity v_B along z_B for Two-axis Holder from lower level to center or upper level will not change the responses such as $M(t_{sim})$, $v(t_{sim})$, and $d_{min}(t_{sim})$. Thus, the translation velocity v_B is statistically insignificant as other factors for all three outputs in Two-axis Holder. This indicates that the alternate length given by ±60 mm along the z_B axis resides in the vapor plume so that the translation velocity v_B proved statistically insignificant.

The change of the rotation speed ω_D (RPMD) as well as the offset angle of z_D (OffsetAngleD) for Two-axis Holder changed the three responses of the experimental designs. As the level of RPMD changed from the lower to the upper level, the amount deposited on the substrate decreases but the coating uniformity and the minimum coating thickness increase. In contrast, the change of the level of OffsetAngleD from the lower to the upper level increases the amount deposited on the substrate and decreases the coating uniformity and the minimum coating thickness, respectively. Fig. 3.11 particularly shows that the quadratic effect of RPMD on the three responses in Two-axis Holder is significant while the quadratic effect of the OffsetAngleD is significant on only $M(t_{sim})$.

As mentioned before, the objectives are to maximize $M(t_{sim})$ and $d_{min}(t_{sim})$ and to minimize $v(t_{sim})$. Since the RPMD and OffsetAngleD have different linear and quadratic effect on the three responses, the preferable condition would be selected with the compromise among the three objectives.

ANOVA for the three responses using full model with all the possible interactions was preliminarily performed to find out the insignificant interaction terms. The two-way

interactions including the translation velocity v_B (TranVel) were statistically insignificant with 95% confidence. Thus, after pooling the two-way interactions including TranVel as well as all three- and four-way interactions with the error term for a reduced model, ANOVA for the three responses was performed using the reduced model with Minitab. Since the error term for $d_{min}(t_{sim})$ was still 0, all the interaction effects were pooled with the error term for $d_{min}(t_{sim})$. The results are summarized in Table 3.7-3.9.

Table 3.7. Analysis of Variance for reduced model of $M(t_{sim})$

Source	DF	SS	MS	F	P
RPMB	2	0.00035606	0.00017803	15.07	0
TranVel	2	0.00000272	0.00000136	0.11	0.892
RPMD	2	0.00313741	0.0015687	132.75	0
OffsetAngleD	2	0.00282248	0.00141124	119.43	0
RPMB*RPMD	4	0.00024669	0.00006167	5.22	0.001
RPMB*OffsetAngleD	4	0.00011627	0.00002907	2.46	0.055
RPMD*OffsetAngleD	4	0.00010625	0.00002656	2.25	0.074
Error	60	0.000709	0.00001182		
Total	80	0.00749688			

Table 3. 8. Analysis of Variance for reduced model of $v(t_{sim})$

Source	DF	SS	MS	F	P
RPMB	2	0.00835	0.00418	29.36	0
TranVel	2	0.00019	0.0001	0.68	0.511
RPMD	2	3.31817	1.65909	12000	0
OffsetAngleD	2	1.36481	0.6824	4796.57	0
RPMB*RPMD	4	0.03362	0.0084	59.07	0
RPMB*OffsetAngleD	4	0.00087	0.00022	1.53	0.205
RPMD*OffsetAngleD	4	1.25019	0.31255	2196.88	0
Error	60	0.00854	0.00014		
Total	80	5.98474			

Table 3.9. Analysis of Variance for reduced model of $d_{min}(t_{sim})$

Source	DF	SS	MS	F	P
RPMB	2	0	0	0	1
TranVel	2	0	0	0	1
RPMD	2	0.125	0.0625	18	0
OffsetAngleD	2	0.125	0.0625	18	0
Error	72	0.25	0.003472		
Total	80	0.5			

From Table 3.7 and 3.8, the P values of three main factors (RPMB, RPMD, and OffsetAngleD) are zero. This implies that the three factors excluding TranVel are significant with 95% confidence. Also, the interaction of RPMB and RPMD is statistically significant at the 95% confidence level, while the interaction of RPMD and OffsetAngleD is statistically significant at the 95% confidence level only for $v(t_{sim})$. The interaction between RPMB and RPMD is expected to be statistically significant since these factors dictate both the residence time and the location of a substrate in the vapor plume. For the minimum coating thickness $d_{min}(t_{sim})$, the P values of two main factors (RPMD and OffsetAngleD) are zero. This implies that the main factors related the z_D axis, where a substrate attaches directly, are significant for the minimum coating thickness with 95% confidence.

To evaluate the two-way interaction among the four factors, interaction plots for the three responses, $M(t_{sim})$, $v(t_{sim})$, and $d_{min}(t_{sim})$, were generated using Minitab as shown in Figure 3.12-3.14. As can be seen from the interaction plots, there are significant two-way interactions among the three factors, RPMB, RPMD, and OffsetAngleD, for $M(t_{sim})$, $v(t_{sim})$ while there is no significant two-way interaction including $d_{min}(t_{sim})$ except when RPMD = 0rpm or OffsetAngleD = 30°.

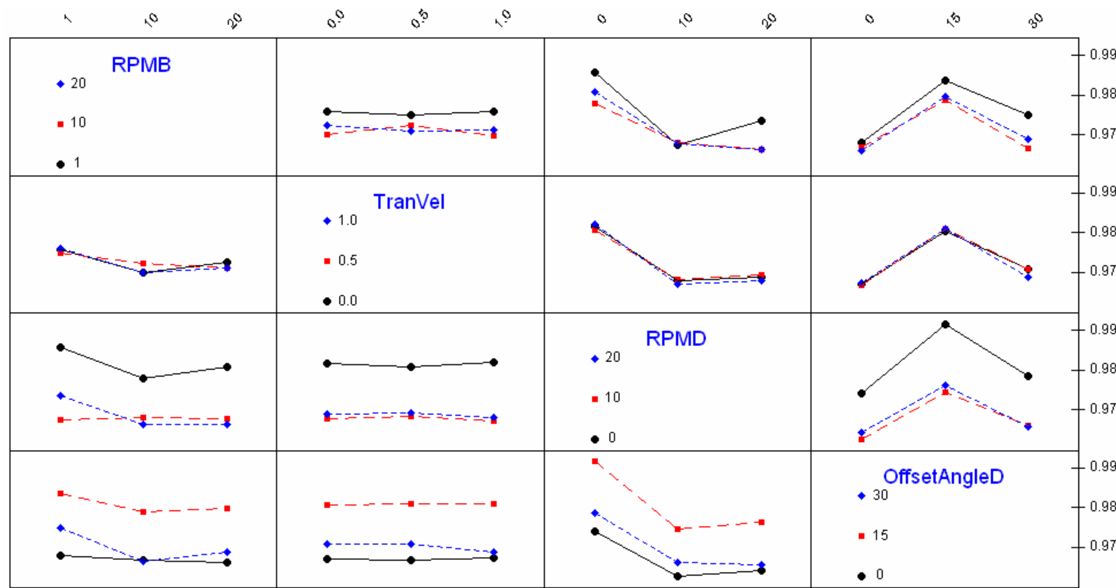

Figure 3.12. Interaction plot for $M(t_{sim})$ in Two-axis Holder.

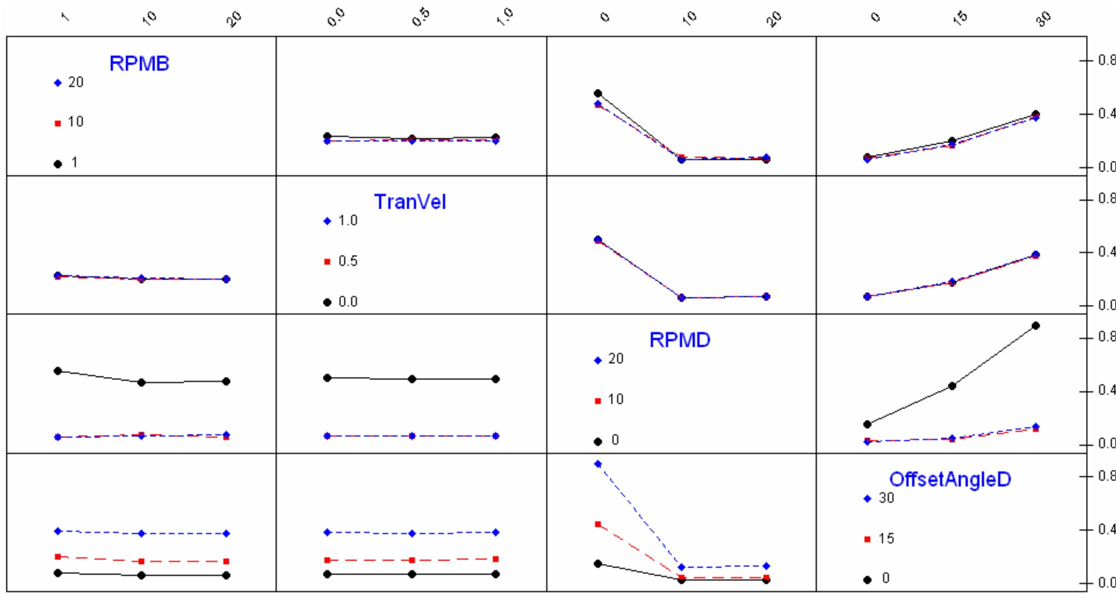

Figure 3.13. Interaction plot for $v(t_{sim})$ in Two-axis Holder.

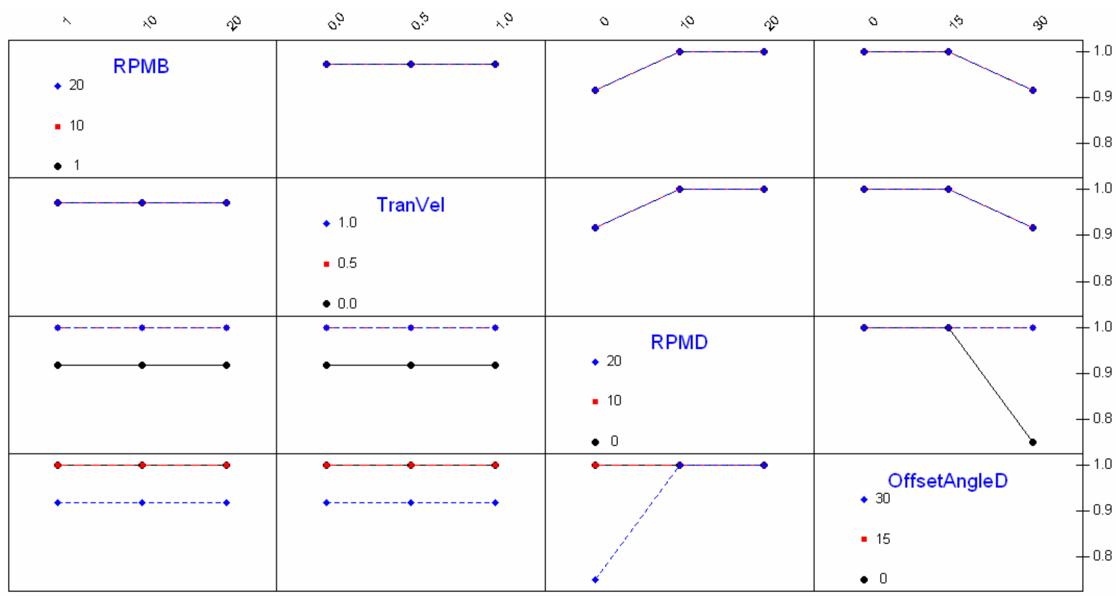

Figure 3.14. Interaction plot for $d_{min}(t_{sim})$ in Two-axis Holder.

3.4. Summary

A discrete state space model for the unified dynamic computational models of EB-PVD process is proposed, which combines the substrate kinematics with machine dynamics and deposition process. The kinematics mode of a substrate was mathematically formulated using techniques commonly used in robotics. The discrete state space model was implemented in Matlab. The computational models were tested on a study of the YSZ deposition on the turbine blade through 3^m full factorial design of experiment in two different holders. Three metrics to measure the coating objectives, such as the sum of coating thicknesses, the variance of coating thickness, and the minimum coating thickness, were chosen as "response variable". Rotation velocity, translation velocity and offset angle with respect to the horizon were chosen as factors. In conclusion, it is shown that the proposed computational model can efficiently emulate the

various kinematics modes that are significantly influenced by the substrate holder. From the statistical analysis of the results of the experimental design, it is derived that the offset angles OffsetAngleB and OffsetAngleD were statistically significant for all three response variables in One-axis and Two-axis Holder, respectively. For Two-axis Holder which has two rotation axes, the rotation velocity of the second axis, ω_D, was statistically significant for all three response variables.

Chapter 4

Simulation of nanostructured coating in EB-PVD using level set approach

In this Chapter a comprehensive modeling approach to link machine dynamics, substrate kinematics and the evolution of the surface profile of coating in electron beam physical vapor deposition (EB-PVD) is presented. The machine dynamics in EB-PVD process are captured by finite element models explained in Chapter 2, which predict evaporation rate and vapor distribution. The substrate kinematics is mathematically formulated with the state space formulation proposed in Chapter 3.

In this Chapter, the propagation of the coating surface is implicitly presented by a level set approach using a function ϕ of higher dimension than the three-dimensional coating surface. The function ϕ is defined as the distance from the coating surface to a three-dimensional point expressed in Cartesian coordinates. Based on this, the coating surface is given by the zero level set of ϕ. In other words, at any time the evolving coating surface can be found by solving for $\phi=0$. By the chain rule of differentiation, a partial differential equation (PDE) is derived involving ϕ and the evolution speed F of the coating surface, which called as a level set equation. The evolution speed F is a critical factor in solving the PDE for the level set function ϕ in the EB-PVD process. Thus, the evolution speed F is derived for the EB-PVD process, by which the machine process parameters of the EB-PVD are related to the deposition process. The level set equation can be regarded as a kind of a Hamilton-Jacobi equation which can be solved to find the coating surface. The solution of the level set equation will be approximated by a

computational scheme which exploits the numerical techniques developed for the solution of the hyperbolic conservation law.

The proposed approach is implemented in Matlab to develop a digital simulator that uses three-dimensional grid with which the level set equation is approximated. The developed simulator performs a series of simulation runs of YSZ deposition on a rotated flat substrate. Compared with the published physical-experiment results, the simulation results demonstrate that the proposed modeling approach can be applied to predict the evolution of coating of EB-PVD process in the nano-level up to 50nm.

4.1. Level set method

A brief introduction to the level set method is presented here for completeness (Sethian 1999). Consider a surface of a substrate $\Gamma(t)$ in $\Re^3$, on which vapor particles are deposited, resulting in coating. The surface $\Gamma(t)$ is assumed to propagate along a direction normal to the surface itself with a speed function F at any time. Using the deposition process model in Eq. 2.15, the speed function F for the EB-PVD process will be developed later. There is an implicit method to represent the surface propagation with ϕ one dimension higher than the three-dimensional surface $\Gamma(t)$. Considering the level set of the time-dependent function ϕ corresponding to a real value c, the introduced function ϕ can be expressed as follows:

$$\phi(x(t), t) = c . \tag{4.1}$$

To embed the surface into ϕ, the level set function ϕ will be defined as a distance function $\pm d$, where d is a distance from the surface to the position $x(t)$ at any time t:

$$\phi(x(t), t) = \pm d \ . \qquad (4.2)$$

Since $d = 0$ at the surface at any time, the position of the surface is regarded as the zero level set of the ϕ so that the value of level set of the surface is set to be zero:

$$\phi(x(t), t) = 0 \ . \qquad (4.3)$$

The illustration of the level set method for two-dimensional front is depicted in Figure 4.1. The evolution of ϕ is linked to the propagation of the surface through a time-dependent initial value problem. By applying the chain rule to Eq. 4.3, a partial differential equation is obtained as follows:

$$\phi_t + \nabla\phi(x(t), t) \cdot x'(t) = 0 \ . \qquad (4.4)$$

Since $F = x'(t) \cdot \hat{n}$, where $\hat{n}$ is the normal vector to the ϕ given by $\hat{n} = \nabla\phi / |\nabla\phi|$, Eq. 4.4 yields an evolution equation of ϕ, namely level set equation (Osher and Sethian 1988):

$$\phi_t + F|\nabla\phi| = 0, \text{given } \phi(x, t = 0) \qquad (4.5)$$

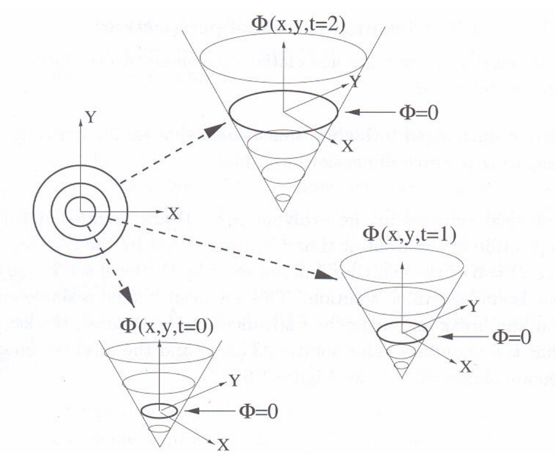

Figure 4.1. Illustration of level set method for two dimensional front (Sethian 1999)

According to Sethian (1999), since there is no change when it is applied to higher dimensions, this method can be applied to 3D deposition process without any change in the formulation. In addition, the intrinsic geometric properties of the surface $\Gamma(t)$ are easily determined. For example, the normal vector is given by $\hat{n} = \nabla\phi / |\nabla\phi|$. Furthermore, the solution of Eq. 4.5 can be accurately approximated by computational schemes which exploit the numerical techniques developed for the solution of the hyperbolic conservation law, and is explained later.

4.2. Speed function F of EB-PVD process

Adalsteinsson and Sethian (1995a; 1995b) applied the level set method to the problem of surface advancement including deposition, etching, and lithography. They proposed the general formulation of the speed function F for each physical phenomenon. They considered three individual types of deposition: isotropic deposition, unidirection deposition, and source deposition. In this Chapter, it is assumed that there is only deposition effect on surface evolution during the EB-PVD process, and that only source deposition occurs. This implies that the deposition radiating from point sources is considered because the EB-PVD is primarily a line-of-sight process where a vapor stream is generated from an ingot melt pool.

The speed function F for EB-PVD process will be derived by modifying the Pulker's deposition process model in Section 2.1.2. First, differentiating Eq. 2.15 with

respect to time t yields Eq. 2.16. Next, replacing the temporal derivative of m in the right hand side of Eq. 2.16 with the evaporated mass a_v per unit time that is derived by Eq. 2.10-2.12, and using the definition of the speed as the ratio of coating thickness increase to time, the temporal derivative of d_s in Eq. 2.16 becomes equal to speed function F as following:

$$F = \frac{n+1}{2\rho\pi} \cdot \frac{\cos^n(\varphi) \cdot \cos(\theta)}{r^2} \cdot a_v. \qquad (4.6)$$

Therefore, Eq. 4.6 can provide the speed of evolution using both the machine-dynamic related data, like the evaporated mass a_v in Eq. 2.12 and the beam collimation parameter n in Eq. 2.13, and the substrate-kinematics related data, like the two angles, φ and θ, and the distance r, shown in Fig. 2.5. The latter data set, namely φ, θ, and r, represents the dependency of the speed function F on the geometric relation between a substrate and a vapor source; it implies that the speed function F varies widely from point to point on the surface of the substrate.

4.3. Numerical scheme for level set equation

Substituting the speed function F of EB-PVD process in Eq. 4.6 into the level set equation in Eq. 4.5 yields a Hamilton-Jacobi equation, namely

$$\phi_t + H(\phi_x, \phi_y, \phi_z) = 0 \qquad (4.7)$$

where the Hamilton $H(\phi_x, \phi_y, \phi_z) = F|\nabla\phi|$. The θ in F of Eq. 4.6 depends on the normal vector to the surface of a substrate $\hat{n}$ and the position vector $\vec{x}$. Since the term of $\cos(\theta)$

in Eq. 4.6 is calculated from the dot product of two vectors $\hat{n}$ and $\vec{x}$, the Hamilton H in Eq. 4.7 is given as a linear equation of ϕ_x, ϕ_y, and ϕ_z. Thus, the Hamilton H can be regarded as convex function. The solution of the level set equation shown in Eq. 4.5 need not be differentiable, even with arbitrarily smooth boundary data (Sethian 1999). This is connected to the notion of appropriate weak solution that means a function for which the derivatives appearing in the equation may not all exist but which is nonetheless deemed to satisfy the equation in some precisely defined sense. Thus computational solution will requires a numerical technique that can handle this non-differentialbility. Osher and Sethian (1988) introduced a numerical algorithm to approximate the level set equation in Eq. 4.5. They relied on an essentially non-oscillatory (ENO) scheme which can accurately capture the formation of sharp gradients and cusps in the moving fronts with various orders of accuracy. In this Chapter, a numerical scheme with first order in time and second order in space is used (Sethian 1999), which is given by

$$\phi_{ijk}^{s+1} = \phi_{ijk}^{s} - \Delta t[\max(F_{ijk},0)\nabla^{+} + \min(F_{ijk},0)\nabla^{-}] \qquad (4.8)$$

where

$$\begin{aligned}
\nabla^{+} = [&\max(MX,0)^2 + \min(PX,0)^2 \\
&+ \max(MY,0)^2 + \min(PY,0)^2 \\
&+ \max(MZ,0)^2 + \min(PZ,0)^2]^{1/2}, \\
\nabla^{-} = [&\max(PX,0)^2 + \min(MX,0)^2 \\
&+ \max(PY,0)^2 + \min(MY,0)^2 \\
&+ \max(PZ,0)^2 + \min(MZ,0)^2]^{1/2},
\end{aligned} \qquad (4.9)$$

where

$$
\begin{aligned}
MX &= D_{ijk}^{-x} + \frac{\Delta x}{2} m\left(D_{ijk}^{-x-x}, D_{ijk}^{+x-x}\right) \\
PX &= D_{ijk}^{+x} + \frac{\Delta x}{2} m\left(D_{ijk}^{+x+x}, D_{ijk}^{+x-x}\right) \\
MY &= D_{ijk}^{-y} + \frac{\Delta y}{2} m\left(D_{ijk}^{-y-y}, D_{ijk}^{+y-y}\right) \\
PY &= D_{ijk}^{+y} + \frac{\Delta y}{2} m\left(D_{ijk}^{+y+y}, D_{ijk}^{+y-y}\right) \\
MZ &= D_{ijk}^{-z} + \frac{\Delta z}{2} m\left(D_{ijk}^{-z-z}, D_{ijk}^{+z-z}\right) \\
PZ &= D_{ijk}^{+z} + \frac{\Delta z}{2} m\left(D_{ijk}^{+z+z}, D_{ijk}^{+z-z}\right),
\end{aligned}
\qquad (4.10)
$$

where D means the shorthand notation of $D\phi$; D^{+} and D^{-} are forward and backward first-order difference operators; D^{++}, D^{+-}, and D^{--} are forward, centered, and backward second-order difference operators; and the switch function m is given by

$$
m(x, y) = \begin{cases} \begin{cases} x & \text{if } |\mathrm{x}| \le |\mathrm{y}| \\ y & \text{if } |\mathrm{x}| > |\mathrm{y}| \end{cases} & xy \ge 0 \\ 0 & xy < 0 \end{cases}. \qquad (4.11)
$$

As mentioned before, only source deposition is considered for the EB-PVD process, and this implies that the speed function F given by Eq. 4.6 for the EB-PVD is always non-negative, namely that the surface always evolves outward. Therefore, the right term inside of the square bracket in Eq. 4.8 becomes always zero.

Sethian and Strain (1992) showed that the approximation of normal vector $\hat{n}$ can be biased along computational grid lines under the condition of anisotropic speed function and introduced a numerical technique to diminish the grid effect in two-dimensional case. In this Chapter, it is extended to three-dimension case to derive the

normal $\hat{n}_{ijk}$ at the grid point ($i\Delta x$, $j\Delta y$, and $k\Delta z$), where Δx, Δy, and Δz are the space steps along x, y, and z axis, respectively, as follows:

$$\begin{aligned} n^{*}_{ijk} &= \frac{\phi_x, \phi_y, \phi_z}{(\phi_x^2 + \phi_y^2 + \phi_z^2)^{1/2}} \\ &\approx \frac{1}{w_n}\left[\begin{array}{l} n_{ijk}^{+x+y+z} + n_{ijk}^{+x+y-z} + n_{ijk}^{+x-y+z} + n_{ijk}^{+x-y-z} \\ + n_{ijk}^{-x+y+z} + n_{ijk}^{-x+y-z} + n_{ijk}^{-x-y+z} + n_{ijk}^{-x-y-z} \end{array}\right] \end{aligned} \tag{4.12}$$

where w_n is the weight coefficient that represents the number of approximation in the square bracket which has non-zero denominator and

$$\begin{aligned} n_{ijk}^{+x+y+z} &= \frac{\left(D_{ijk}^{+x}, D_{ijk}^{+y}, D_{ijk}^{+z}\right)}{[\left(D_{ijk}^{+x}\right)^2 + \left(D_{ijk}^{+y}\right)^2 + \left(D_{ijk}^{+z}\right)^2]^{1/2}}, \\ &\cdots, \\ n_{ijk}^{-x-y-z} &= \frac{\left(D_{ijk}^{-x}, D_{ijk}^{-y}, D_{ijk}^{-z}\right)}{[\left(D_{ijk}^{-x}\right)^2 + \left(D_{ijk}^{-y}\right)^2 + \left(D_{ijk}^{-z}\right)^2]^{1/2}}. \end{aligned} \tag{4.13}$$

If the any approximation in Eq. 4.12 vanishes with zero denominator, the term will be ignored in the recalculation of the weight coefficient w_n. Then normalizing n^{*}_{ijk} obtains $\hat{n}_{ijk} = n^{*}_{ijk} / \left|n^{*}_{ijk}\right|$.

4.4. Simulation and Results

The level set method for the EB-PVD process is embedded into the unified models of the EB-PVD process, discussed in Chapter 2, and then the integrated model is implemented using Matlab on a PC cluster LION-XO of Penn State's ASET to predict the time-dependent deposition evolution of deposition layers in nano-order. A flow chart

for the EB-PVD simulator implementing the level set method as well as the unified models of the EB-PVD process is depicted in Figure 4.1.

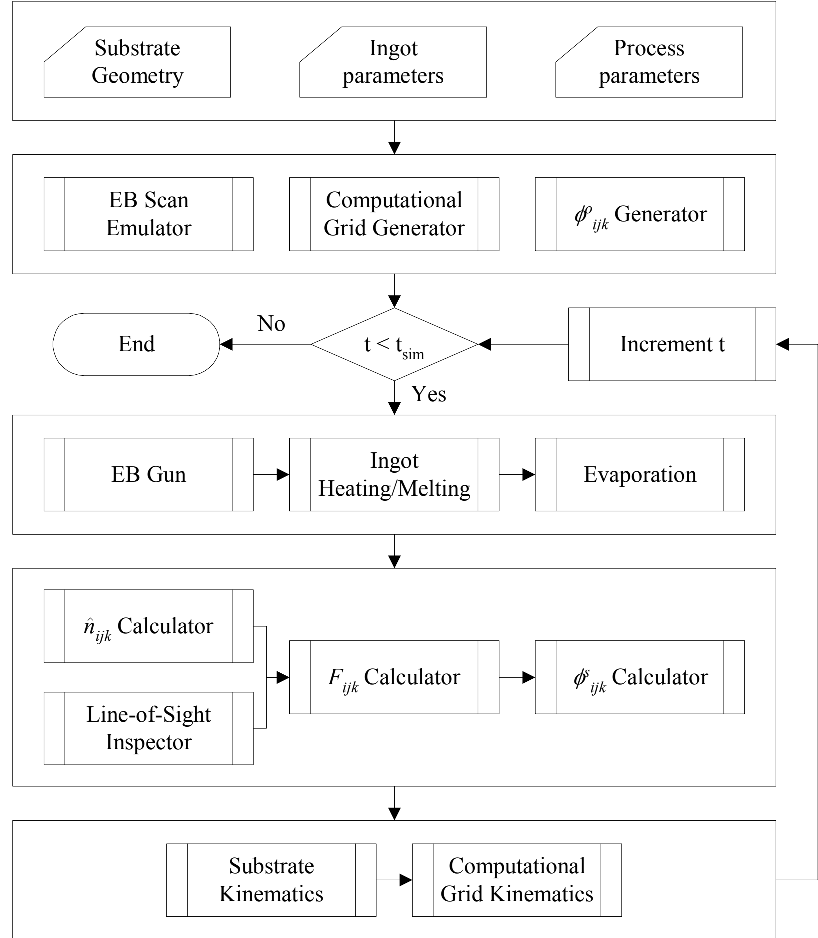

Figure 4.1. Flow chart of the EB-PVD simulator implementing the level set method

The simulator inputs include substrate geometry, ingot parameters, and process parameters, together with the process plan that constrains simulation period, ingot heating process, and substrate kinematics mode, etc. To prepare the dynamic simulation of the EB-PVD process, 'EB scan emulator' shown in Figure 4.1 decides, based on the given

scan pattern, the order of elements of the ingot mesh where EB impinges. ‘Computational grid generator’ in Figure 4.1 generates three-dimension computational grid with the space steps Δx, Δy, and Δz. The initial value of ϕ at all computational-grid points, ϕ_{ijk}^{o}, will be calculated as the distance from the grid point to the surface of the substrate, based on the definition of in Eq. 4.2. In the main body of the simulator, at first, the machine dynamics model is computed which includes the EB current, the temperature tomography of the ingot surface, and the evaporation rate a_v and the beam collimation parameter n, respectively, of each element of the ingot mesh. In the next module, after calculating the normal vector $\hat{n}$ of every grid point and inspecting the visibility of each grid point from vapor source, the speed function F of every grid point will be calculated using Eq. 4.6, with which the level set equation in Eq. 4.5 will be solved to approximate ϕ_{ijk}^{s} at every iteration during simulation using Eq. 4.8-4.11. Finally, the spatial location of both the substrate and the computational grid will be updated based on the given substrate kinematics mode.

To validate the developed simulator, the numerical solution is compared with the experiment results by Yamaguchi et al. (2003), where YSZ was chosen as coating material. This specific paper by Yamaguchi et al. is chosen for comparison because of the thorough documentation of experimental parameters. In the experiments YSZ was deposited upon a hexagonal plate located over the ingot while the input power varied from 35kW to 60kW and the rotation speed also varied from 1rpm to 20rpm with or without the alternation of rotation direction about 180° as experiment parameters. As the

results of the experiments, the microstructures of coating layer, deposition rate and porosity were measured. The arrangement of the experiments is illustrated in Figure 4.2.

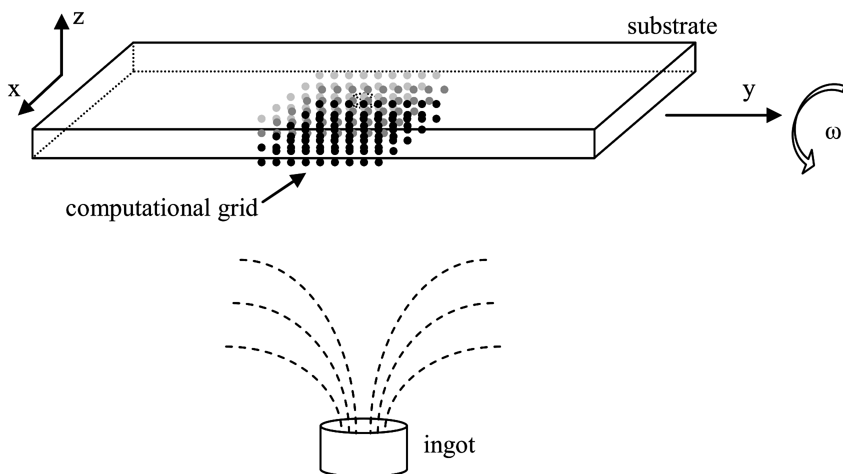

Figure 4.2. Experimental arrangement

The substrate 60mm long in y-axis direction and 20mm wide in x-axis direction and 2.5mm thick in z-axis direction is mounted 300mm above the surface of an ingot. It is rotated counter-clockwise about the positive y-axis at the given rotation speed and, in some experiments, the rotation direction will be alternated at 180°. The three-dimensional computational grid, where the level set function ϕ will be calculated by solving the level set equation in Eq. 4.5, is placed on the center of the substrate just above the center of the ingot surface. The space steps along x, y, and z axis, Δx, Δy, and Δz, are set to be equal to each other as $\Delta = \Delta x = \Delta y = \Delta z$ on each experiment. The themophysical properties of YSZ, summarized by Simon and Pal (1999), are used in this Chapter. In the simulation, the electron-beam power was fixed as 45kW and the time step was 0.01s for

computational experiments. The kinematics parameters used in the simulation runs were set to be same with the physical experiments by Yamaguchi et al. (2003). That is, two rotational modes, such as no alternation and alternation at 180°, were selected; the rotation speed was varied from 1rpm to 20rpm in both rotational modes.

In particular, the size of the Δ was varied from 1μm to 100nm and to 50nm to investigate the effect of Δ on the resolution of the proposed model. Simulation period was fixed at 120sec with Δ = 1μm and 60sec with Δ = 100nm and 50nm, respectively. Table 4.1 summarizes the machine process parameters and empirical parameters used in the simulation.

Table 4.1. Parameters used in the simulation

Machine parameters	Empirical parameters
Ingot height = 500 mm EB power = 45 kW Cathode heating efficiency η_A=3.0 mA/W Electron beam diameter = 3 mm Scan pattern = Swirl # of circulation of beam scan = 7 Scan frequency = 100 kHz	Variance of white noise of current and voltage = 0.01 Initial temperature of ingot and crucible = 298.15 K Vapor flux scattering coefficient = 1 (no scatter) Condensation coefficient = 1 (ideal condensation) Evaporation coefficient = 1 (ideal evaporation)

The thickness of deposition at the surface was calculated from the value of the level set function ϕ of every point of the computational grid. The change of sign of the value of ϕ from plus to minus in the computational grid is regarded as the change of thickness by the one space step. Since the level set method uses the discretized,

computational grid, the continuous change of the thickness can not be seen but the step function shape. The number of the grid point varied with respect to the size of the space step: 11×11×16 when Δ = 1μm and 20×20×20 when Δ = 100nm and 50nm, respectively. As mentioned before, the level set method can calculate the normal vector $\hat{n}$ of every grid point, with which the evolution direction on the surface can be estimated. In every iteration the evolution vector will be constructed at (i×j) grid points for every i and j that has the zero- or the maximum negative-value of ϕ. Its unit vector and norm are given by the normal vector $\hat{n}$ and by the product of Δt and speed function F, respectively. That is, there will be calculated the evolution vectors for every i and j in every n_{itr} iteration, which is given by the simulation period dividing by Δt. The n_{itr} evolution vectors for every i and j will be added together to estimate the evolution direction. Figure 4.3 shows the screenshot of the simulation model including a rotating substrate over an ingot represented with square.

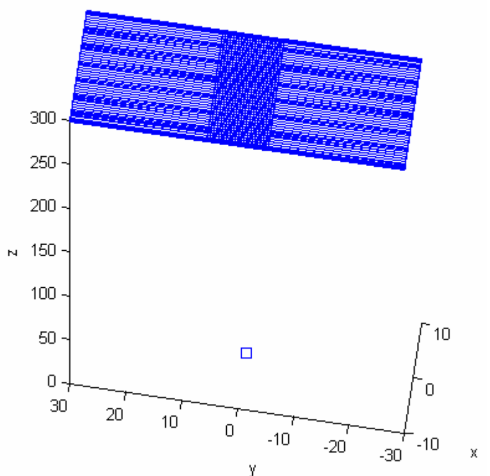

Figure 4.3. The screenshot of simulation model in Matlab

Figure 4.4 shows the simulation results under various rotation speeds from 1rpm to 20rpm with $\Delta = 1\mu m$ and without the change of the rotation direction. Figure 4.4(a), 4.4(c), and 4.4(e) show the thickness of deposition in μm and the speed of evolution in 10^{-4}mm/sec against time in second under the different rotation speeds. Since the rotation was set to start at time 0, the speed of evolution asymptotically increases to the steady-state speed of evolution during the early period. When the computational grid receded from the sight of vapor source, the speed of evolution decreased, while when it approached to the vapor source, the speed of evolution increased and became the maximum just above the ingot, as seen in the curve of the speed of evolution.

As the rotation speed increases, there was no significant change in the deposition rate or the thickness of the deposited YSZ. This can be explained by the same residence time in the vapor plume even though the rotation speed varies. Significant differences, however, existed in the shape of the curves of the thickness of the deposition, which has the shape of step function. That is, at low rotation speed like 1rpm (Figure 4.4(a)), the interruption time when there was no increase in the thickness was long so that the horizontal step also was longer than at the high rotation speed like 20rpm (Figure 4.4(e)), where the horizontal step was short and even in the whole deposition time. Figure 4.4(b), 4.4(d), and 4.4(f) show the evolution directions at two points, into which the n_{itr} evolution vectors were added together, respectively, and from which the structure of the deposition layer of YSZ could be estimated. The unit of x-axis is 10^{-8}mm.

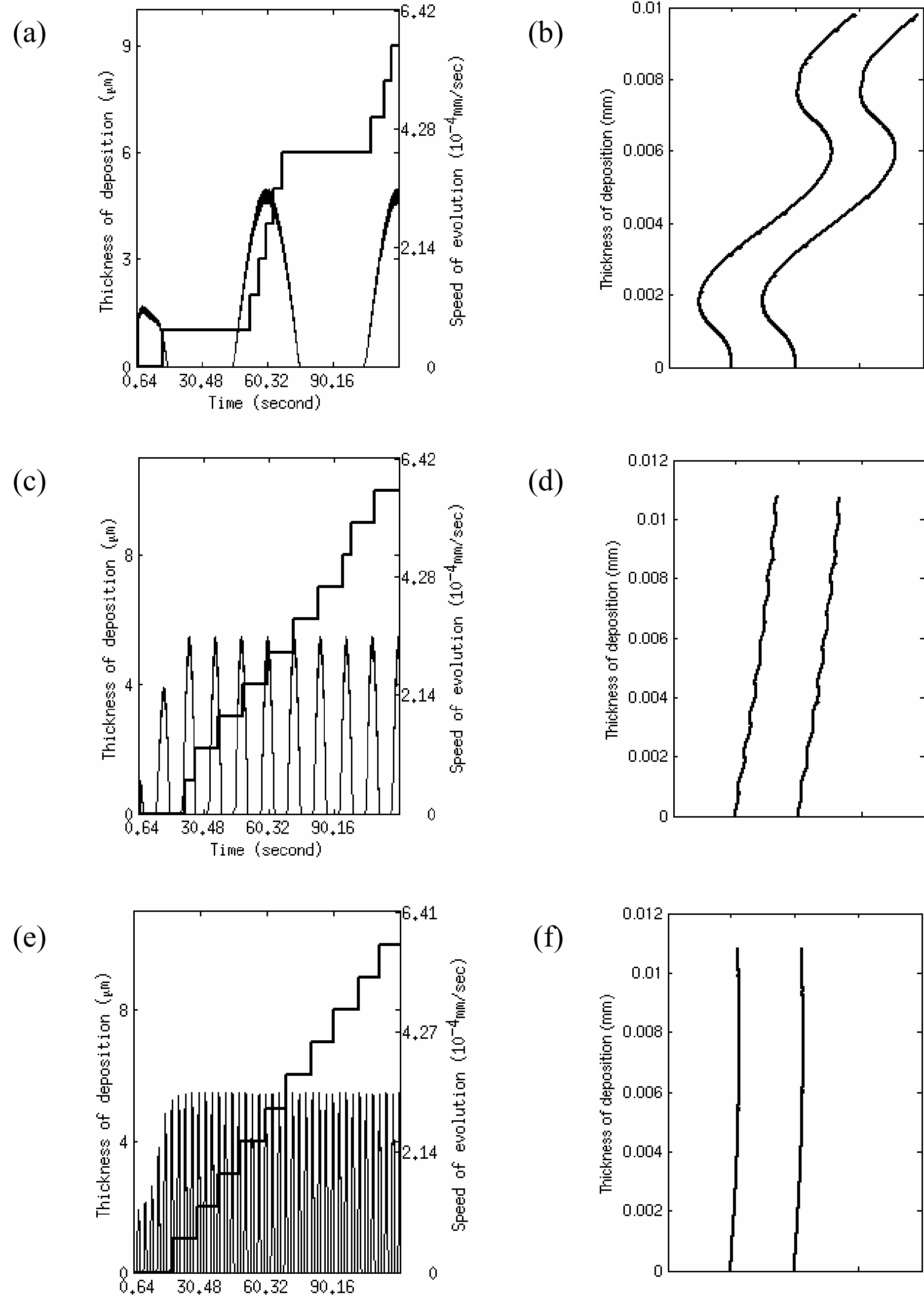

Figure 4.4. Simulation results under various rotation speeds with Δ = 1μm and without the change of rotation direction: a) and b) with 1rpm, c) and d) with 5rpm, e) and f) with 20rpm

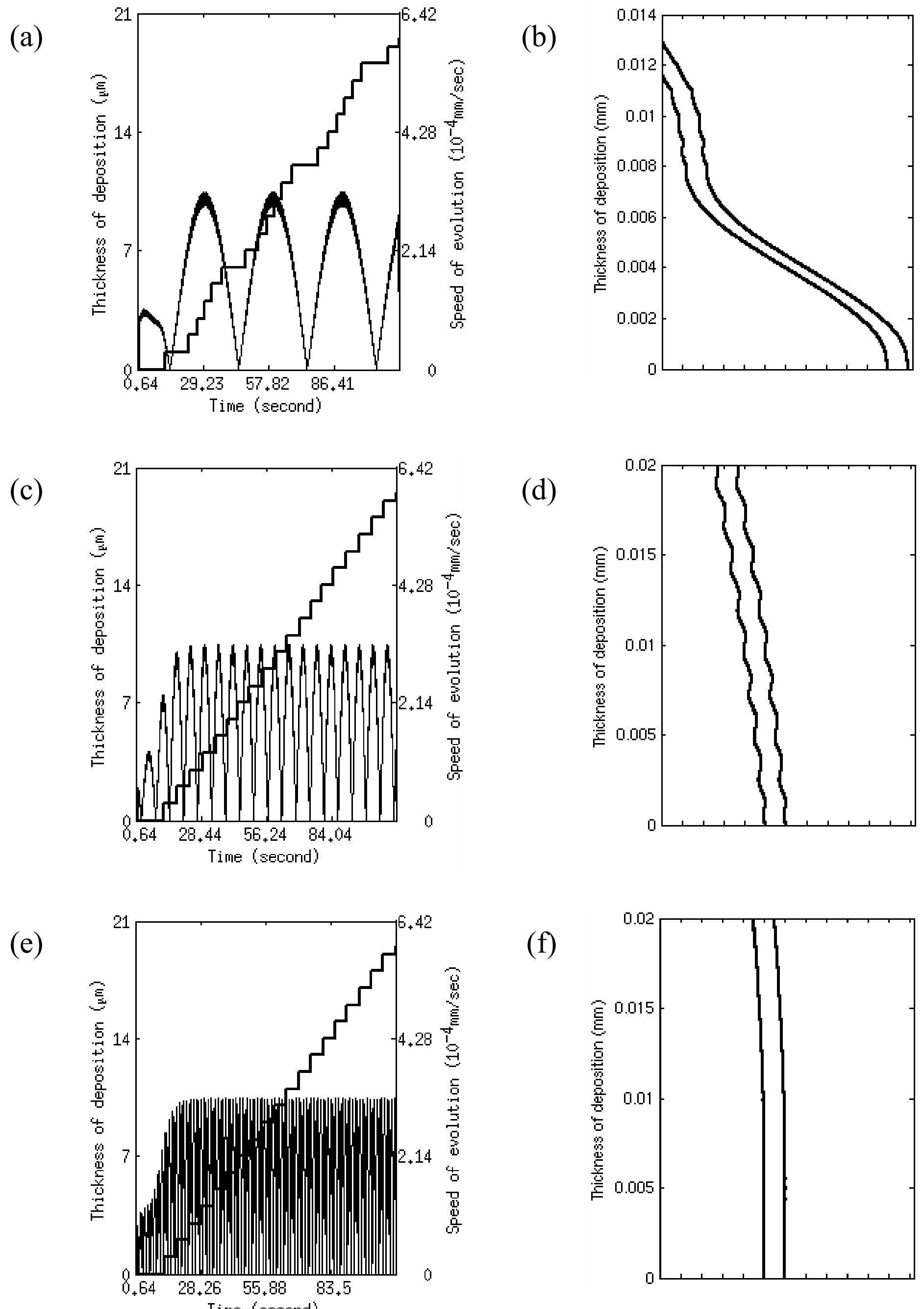

Figure 4.5. Simulation results under various rotation speeds with Δ = 1μm and the change of rotation direction at 180°: a) and b) with 1rpm, c) and d) with 5rpm, e) and f) with 20rpm

At low rotation speed like 1rpm (Figure 4.4(b)), the ‘zigzag’ structure with about 6μm pitch is clearly seen, which similarly exhibited in the bent column with about 5μm pitch from the experiment results by Yamaguchi et al. (2003), shown in Figure 4.6. The higher magnification image in Figure 4.7 referred to Yamaguchi et al. (2003) shows more clearly the bent columns of the same experimental condition. As the rotation speed increases to 20rpm (Figure 4.4(f)), the evolution direction shows less-bent shape as small as about 0.3μm compared to the straight column with almost 0μm pitch from the experiment results shown in Fig. 4.6 (c).

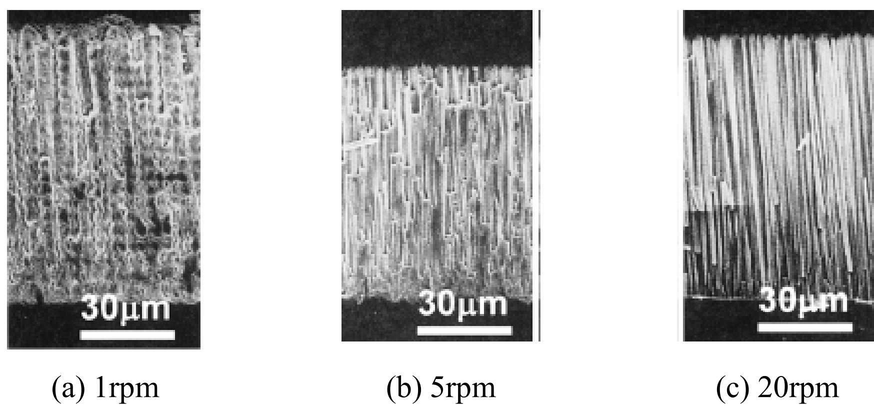

(a) 1rpm (b) 5rpm (c) 20rpm

Figure 4.6. Experimental results under various rotation speeds (Yamaguchi et al., 2003)

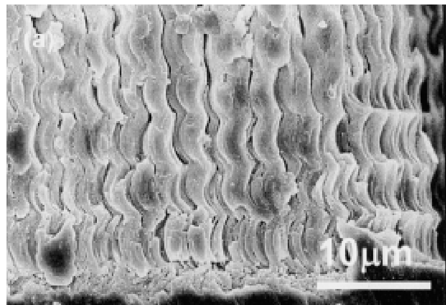

Figure 4.7. Bent columns under the rotation speed of 1 rpm (Yamaguchi et al., 2003)

When the rotation direction altered at every 180°, however, the deposition rate increased, compared to the condition of no alternation of the rotation direction, as seen in the comparison between Figure 4.4 and 4.5. This can be explained by the increase of the residence time in vapor plume. That is, there was not “no-deposition” period in the case of alternation of the rotation direction as seen in the speed of evolution shown in Figure 4.5. Figure 4.5(b), 4.5(d), and 4.5(f) show the evolution directions at two points. The unit of x-axis is 10^{-8}mm. At low rotation speed like 1rpm (Figure 4.5(b)), the ‘zigzag’ structure with about 10μm pitch is clearly seen, which similarly exhibited in the bent column with about 8μm pitch from the experiment results by Yamaguchi et al. (2003), shown in Fig. 4.8.

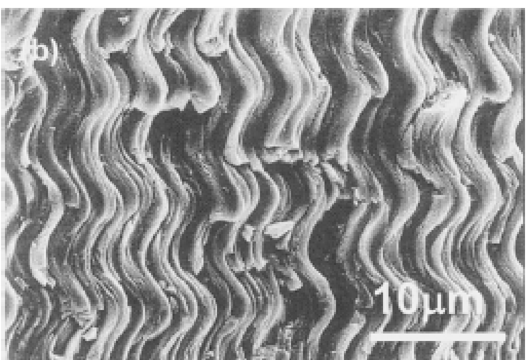

Figure 4.8. Bent columns under the rotation speed of 1 rpm (Yamaguchi et al., 2003)

In Table 4.2 the pitches of the ‘zigzag’ structure at various conditions are summarized to compare experimental results and those predicted using the unified dynamics computational models when $\Delta = 1\mu m$.

Table 4.2. Comparison of experiment and simulation for a plate coated with YSZ

Experimental conditions		Predicted pitch	Experimental pitch (Yamaguchi et al. 2003)
Change of rotation direction	RPM		
No	1 rpm	6μm	5μm
No	5 rpm	1μm	≥0μm
No	20 rpm	0.3μm	0μm
180°	1 rpm	10μm	8μm
180°	5 rpm	2.5 μm	≥0μm
180°	20 rpm	≥0μm	0μm

Table 4.2 implies that the pitch of the 'zigzag' structure becomes larger with the alternation at 180° (Figure 4.5) than with no alternation of the rotation direction (Figure 4.4). For example of low rotation speed like 1rpm, the pitch of the 'zigzag' structure with the alternation is larger than that without the alternation

Figure 4.9 and 4.10 show 11 time marks at the same intervals. While there was no deposition in the point of 1, 2, 10, and 11 without the alternation of rotation direction (Figure 4.9), the deposition occurred at all time marks in the case of the change of the rotation direction (Figure 4.10).

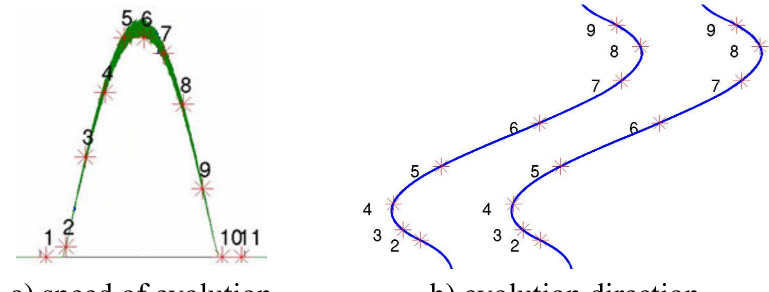

a) speed of evolution   b) evolution direction

Figure 4.9. Time marks with Δ = 1μm, 1rpm, and no change of rotation direction

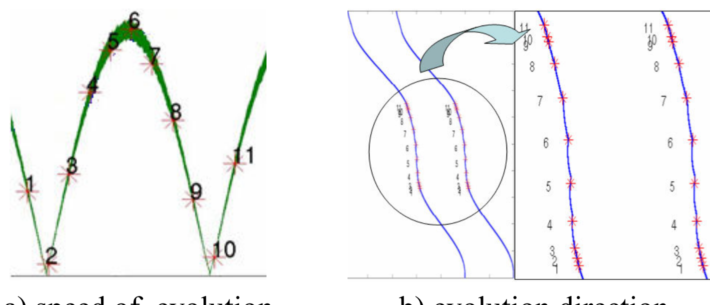

a) speed of evolution b) evolution direction

Figure 4.10. Time marks at the same with Δ = 1μm, 1rpm, and the change of rotation direction at 180°

Figure 4.11 shows simulation results under various rotation speeds from 1rpm to 20rpm when Δ = 100nm without the alternation of the rotation speed. Figure 4.11(a), 4.11(c), and 4.11(e) show the thickness of deposition in 100nm and the speed of evolution in 10^{-4}mm/sec. During the simulation period of 60sec, at low rotation speed of 1rpm (Figure 4.11(a)), the deposition rate was reduced to half of that observed at higher rotation speed (Figure 4.11(c) and 4.11(e)). This can be explained by the limitation of visibility of the point where the computational grid resided in the early stage of the simulation. This difference of the deposition rate will decrease as this simulation run longer. In the case of Δ = 100nm shown in Figure 4.11, the shape of the thickness of deposition were similar to that with Δ = 1μm, shown in Figure 4.4. That is, at low rotation speed like 1 rpm (Figure 4.11(a)), the interruption time when there was no increase in the thickness was long so that the horizontal step also was longer than at the high rotation speed like 20 rpm (Figure 4.11(e)). Figure 4.11(b), 4.11(d), and 4.11(f) show the evolution directions at two points, where Figure 4.11(b) shows just a part of the deposition layer. The unit of x-axis is 10^{-9}mm. As in the case of Δ = 1μm shown in

Figure 4.4, the amplitude and pitch of the 'zigzag' structure decreased as the rotation speed increased from 1rpm ((Figure 4.11(b))) to 20rpm ((Figure 4.11(f))).

When the rotation direction altered at every 180°, however, the deposition rate increased, compared to the condition of no alternation of the rotation direction, as seen in the comparison between Figure 4.11 and 4.12. This can be explained by the increase of the residence time in vapor plume as mentioned before. Comparing the evolution directions under the same rotation speed in Figure 4.11 and 4.12, the amplitude and pitch of the 'zigzag' structure were larger with the alternation at 180° (Figure 4.12) than with no alternation of the rotation direction (Figure 4.11). For example of the middle rotation speed of 5rpm, the pitch of the 'zigzag' structure with the alternation, which is about 12.5µm shown in Figure 4.12(d), is larger than that without the alternation, which is about 10µm shown in Figure 4.11(d).

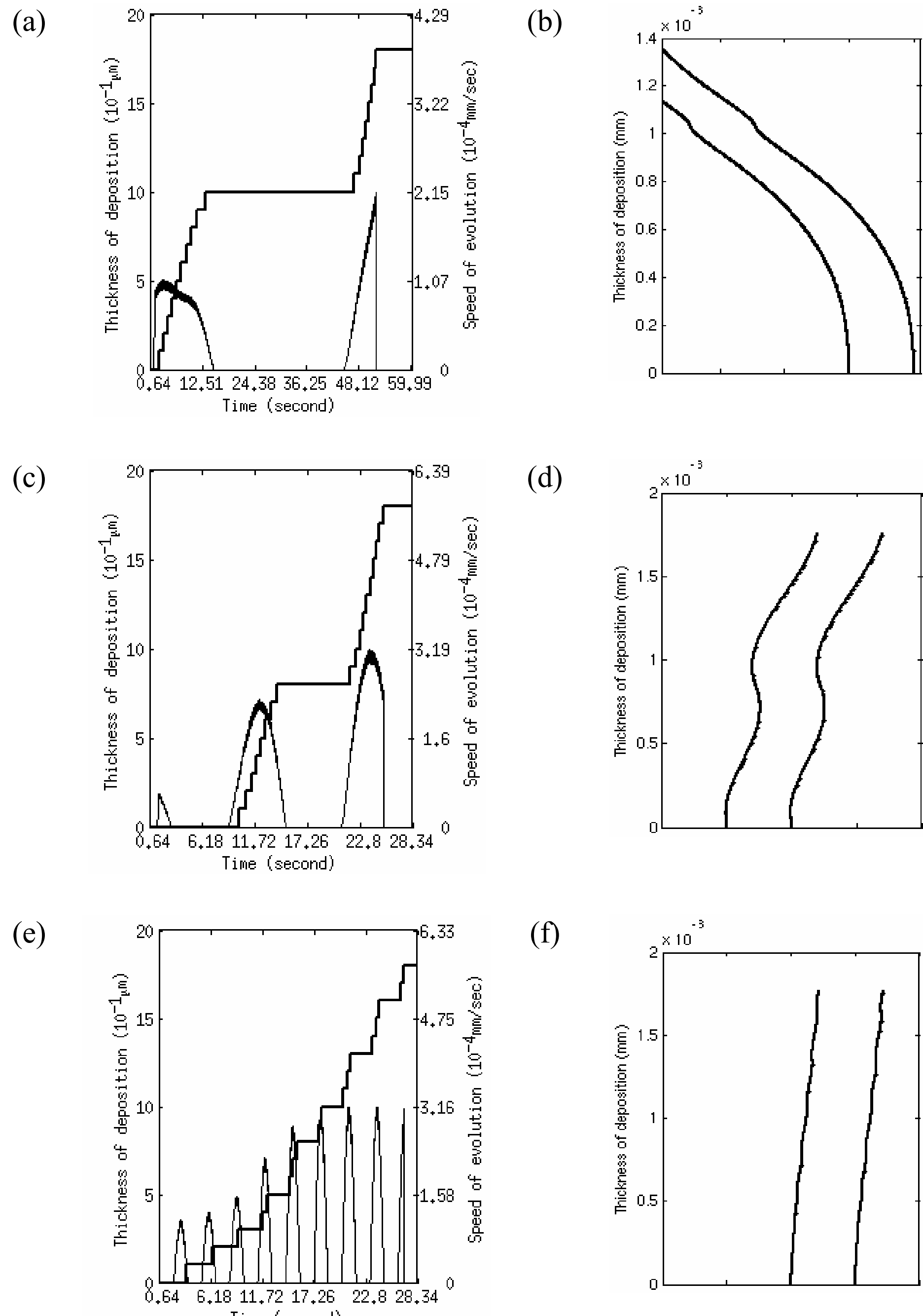

Figure 4.11. Simulation results under various rotation speeds with Δ = 100nm and without the change of rotation direction: a) and b) with 1rpm, c) and d) with 5rpm, e) and f) with 20rpm

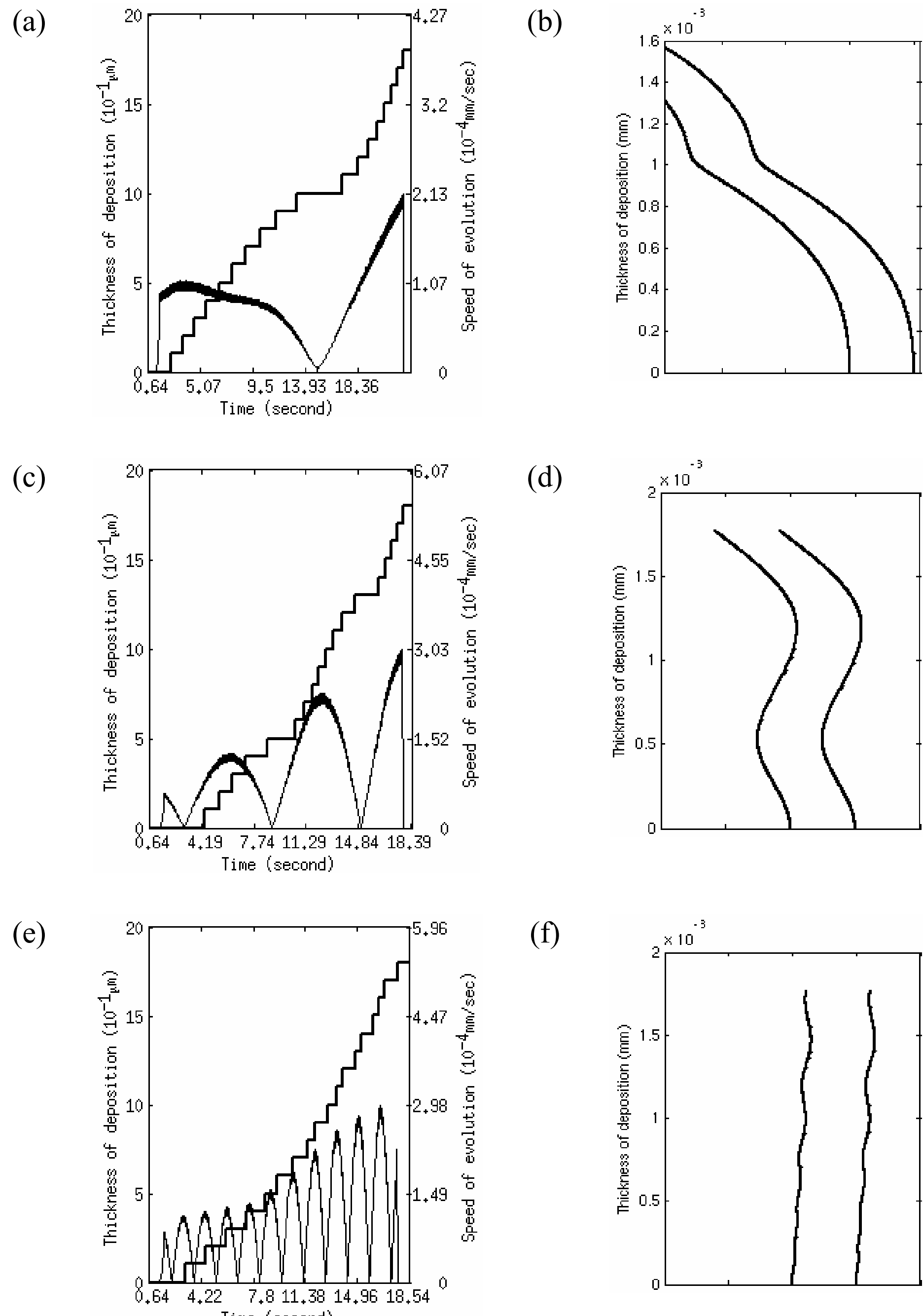

Figure 4.12. Simulation results under various rotation speeds with Δ = 100nm and the change of rotation direction at 180°: a) and b) with 1rpm, c) and d) with 5rpm, e) and f) with 20rpm

Figure 4.13 shows simulation results under various rotation speeds from 1rpm to 20rpm with Δ = 50nm and without the change of the rotation direction. Figure 4.13(a), 4.13(c), and 4.13(e) show the thickness of deposition in 50nm and the speed of evolution in 10^{-4}mm/sec. Contrary to the results with Δ = 1μm and 100nm, at low rotation speed like 1rpm (Figure 4.13(a)), the deposition rate was larger than that at higher rotation speed (Figure 4.13(c) and 4.13(e)). Figure 4.13(b), 4.13(d), and 4.13(f) show the evolution directions at two points, where just a part of the deposition layer are depicted. The unit of x-axis is 10^{-9}mm. As in the case of Δ = 1μm and 100nm shown in Figure 4.4 and 4.11, respectively, the amplitude and pitch of the 'zigzag' structure decreased as the rotation speed increased from 1rpm (Figure 4.13(b)) to 20rpm (Figure 4.13(f)). When the rotation direction altered at every 180°, the deposition rate slightly increased, compared to the condition of no alternation of the rotation direction, as seen in the comparison between Figure 4.13 and 4.14.

Comparing the evolution directions under the same rotation speed in Figure 4.13 and 4.14, the amplitude and pitch of the 'zigzag' structure were similar in both conditions with no alternation of the rotation direction (Figure 4.13) and with the alternation at 180° (Figure 4.14). As seen in Figure 4.13 and 4.14 where the space step of the computational grid Δ = 50nm, the evolution directions are similar to the 'zigzag' structure at Δ = 1μm and 100nm shown in Figure 4.4 to 4.12. Assuming that the structure of the deposition layer can be estimated from the evolution direction, the similarity verifies the feasibility of the proposed model and the developed simulator to estimate the deposition phenomena in the nano-level up to the 50nm.

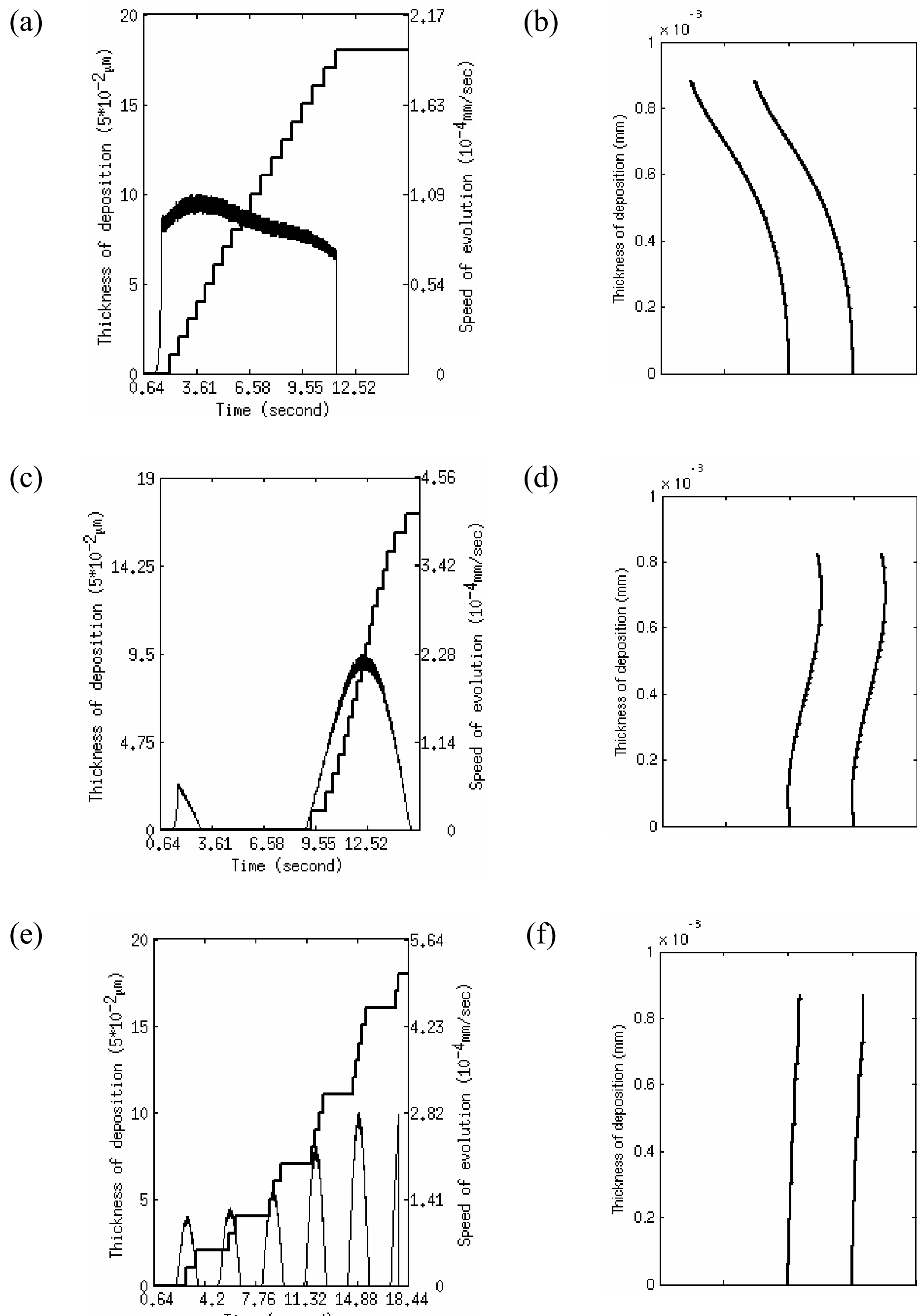

Figure 4.13. Simulation results under various rotation speeds with Δ = 50nm and without the change of rotation direction: a) and b) with 1rpm, c) and d) with 5rpm, e) and f) with 20rpm

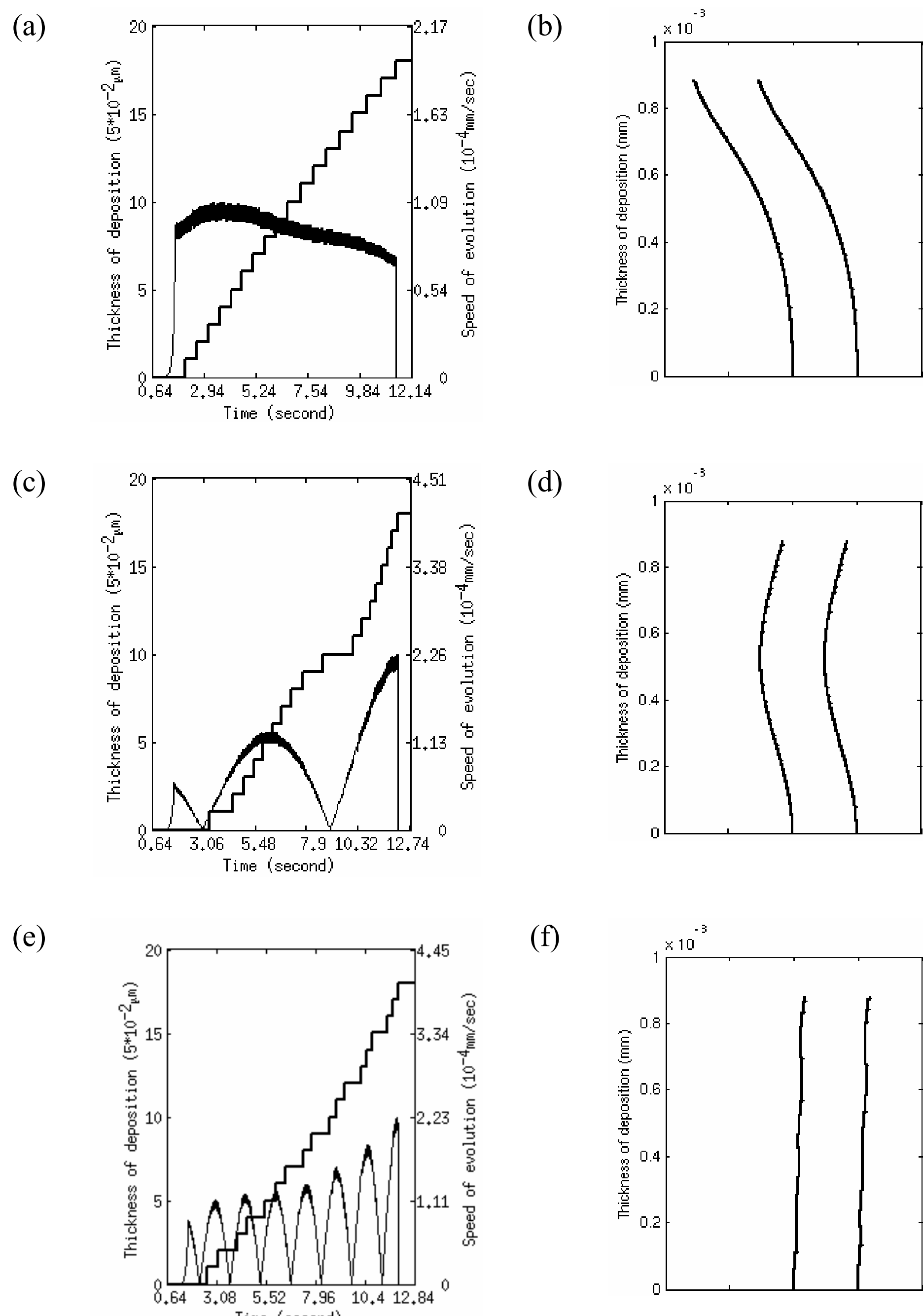

Figure 4.14. Simulation results under various rotation speeds with Δ = 50nm and the change of rotation direction at 180°: a) and b) with 1rpm, c) and d) with 5rpm, e) and f) with 20rpm

Hawkeye and Brett (2005) could control the thin film microstructure in nanoscale by using glancing angle deposition (GLAD) technique. That is, manipulating the substrate kinematics mode changed the geometries of thin film microstructures, resulting in various columnar structures such as zigzag or chevron, spiral, helical, or vertical post. For example, the helical columnar structure can be generated when a substrate is slowly and continuously rotated without the intermittent of the rotation direction as shown in Fig. 4.15.

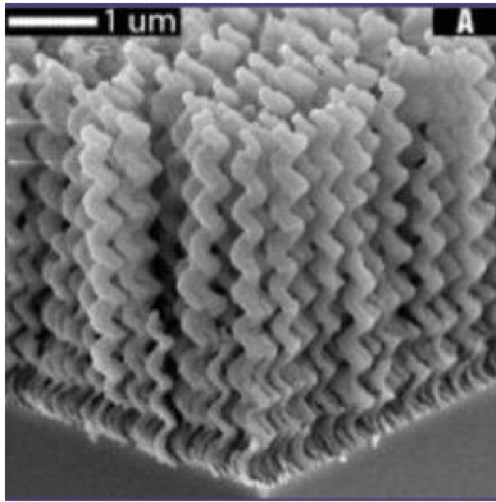

Figure 4.15. Helical columnar shape from experiment in the low rotation speed (Hawkeye and Brett, 2005)

When the normal vector $\hat{n}$, used as the unit vector of the evolution vector, is rotated by the rotating angle of the substrate relative to the y-axis shown in Figure 4.2, the resulting evolution vector can involve a change of the incidence angle of the vapor flux. For the case of 1rpm with $\Delta = 1\mu m$ and without the change of rotation direction,

shown in Figure 4.4(a) and 4.4(b), the revised evolution direction is constructed with the rotated evolution vector, and the result is shown as Figure 4.16. This result shows that the proposed model and the developed simulator fairly well predict the deposition phenomena by using the level set method.

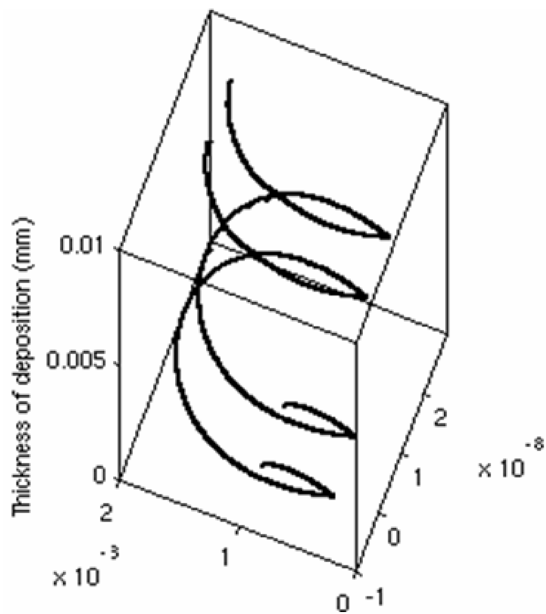

Figure 4.16. Helical columnar shape from simulation in the low rotation speed

4.5. Summary

Based on the unified model of EB-PVD process, the integrated modeling is proposed by extending the level set approach into EB-PVD process. From the traditional deposition models that use the geometric distribution of vapor plume to predict the thickness distribution of coating, the speed function *F* is derived, which is critical to solve the level set equation. To accurately approximate solutions of the level set equation, the numerical technique borrowed from the numerical solutions of hyperbolic conservation

laws is applied. That is, the first order-forward difference scheme is chosen in time space and the second order difference scheme is chosen in spatial space, respectively. The proposed modeling method was implemented in Matlab; to verify it, the simulation results were compared with the experiments. With the literature about YSZ experiment using EB-PVD, the empirical parameters used in the model could be calibrated. In addition, it was investigated the effect of the rotation speed and the change of the rotation direction on the evolution of deposition and the deposition rate. The intrinsic geometrical feature like normal vector could be approximated by the level set approach, with which the evolution direction can be estimated, similar to the columnar structures shown in the experiments. At the micro level in the space step like 50nm, the simulation results showed the similar results with the experiments.

Chapter 5

Parameter selection by solving multiobjective optimization problem

Decision making problems in highly complex system like EB-PVD inevitably involve multiple decision makers (DMs) working in a distributed team structures as well as multiple objectives to be pursued. This Chapter presents a new interactive fuzzy approach for solving multiple objective linear programming (MOLP) problems. In the approach, decision makers' preference can be quantified with a membership function and a reference value, or threshold, of the membership function. A weighted sum of objective functions is assumed as a utility function, resulting in P_λ problem. Using the deviation of membership function from the threshold, a heuristic is developed to automatically search a set of weights factors in their space. It extends the DATC that was originally developed for distributed scheduling of heterarchical manufacturing systems by Prabhu (1995). It applies the feedback control algorithm for making "best" scheduling in real-time. The algorithm is developed by combining the interactive fuzzy approach and DATC. And it is implemented in Matlab and GAMS. The case study for manufacturing TBC made of YSZ using the EB-PVD process is provided to show the feasibility of the proposed algorithm. The formulation of an optimization problem is developed for the EB-PVD process, including four criteria: production cost, uniformity of coating thickness, collection efficiency of material on substrate, and coating lifetime. Physical models and statistical technique are used to develop the formulation and physical constraints also are described. To apply a heuristic developed for distributed environments with multiple decision

makers in different locations, the proposed problem is simplified with the given data and solved. The computational results are provided to show multiobjective optimization of process parameter in EB-PVD and to test the proposed algorithm.

5.1 Problem formulation

In this Chapter, the following multi objective linear programming (MOLP) problem is considered for an MODM problem:

$$\begin{aligned} &\text{maximize}\, \mathbf{f}(\mathbf{x}) = \mathbf{C}\mathbf{x} \\ &\text{subject to } \mathbf{A}\mathbf{x} = \mathbf{b}, \mathbf{x} \geq 0 \end{aligned} \tag{5.1}$$

where **A** is (m×n) matrix of rank m, **b** is an m-vector, **x** is an n-vector of decision variables, and **C** is (p×n) matrix. The $\mathbf{f}(\mathbf{x}) = \{f_1(\mathbf{x}), f_2(\mathbf{x}), \ldots, f_p(\mathbf{x})\}$ are *p* distinct linear objective functions of the decision vector **x,** which are to be maximized in the decision space $\mathbf{X} = \{\mathbf{x} \mid \mathbf{A}\mathbf{x} = \mathbf{b}, \mathbf{x} \geq 0\}$. As mentioned before, it is assumed that there are *p* DMs and that each of them can handle only one linear objective function, so that the membership function of the fuzzy goal of each of the objective functions can be elicited from a DM individually.

In the MOLP problem in Eq. 5.1, the objective functions are assumed to be in conflict, resulting that there is not a *superior solution* but only infinite *efficient solutions*. Mathematically, a point $\mathbf{x}^* \in \mathbf{X}$ is said to be efficient if and only if there is no another $\mathbf{x} \in \mathbf{X}$ such that $f(\mathbf{x}) \geq f(\mathbf{x}^*)$ and $f(\mathbf{x}) \neq f(\mathbf{x}^*)$ (Koopmans 1951). Usually, the set of all efficient solutions, called the efficient set, consists of an infinite number of points, so that

a "*best*" compromise or satisfactory solution among the efficient solutions should be chosen with respect to DM's preference.

When the decision space **X** is a closed convex set, objectives are concave on **X**, an efficient solution can be obtained by solving a single objective problem in which the objectives are combined using weights (Geoffrion 1967; Zionts and Wallenius 1976). The weighted sum of the objectives is assumed as the utility function of all p DMs in the form of $\sum_i \lambda_i f_i(\mathbf{x})$. Since the $f_i(\mathbf{x})$'s are linear functions, the utility function is also linear. As a result, the MOLP problem shown in Eq. 5.1 can be transformed into P_λ problem of the following form:

$$\begin{aligned} &P_\lambda = \text{Max} \sum_{i=1}^{p} \lambda_i f_i(\mathbf{x}) \\ &\text{subject to}: \quad \mathbf{x} \in \mathbf{X}, \quad \sum_{i=1}^{p} \lambda_i = 1, \quad \lambda_i \geq 0 \end{aligned} \tag{5.2}$$

Each DM has expertise related to one of the p objective functions but potentially fuzzy or imprecise goal for this objective function. For example, a goal assigned by a DM to an objective may be to achieve "much larger than A and/or slightly less than B". To quantify this type of statement, the membership function can be derived, by which each value assigned to objective function after calculation is mapped to [0, 1]. To derive a membership function $\mu_{f_i}(\mathbf{x}), i = 1, \ldots, p$, at first the minimum $f_i^{\min}$ and maximum $f_i^{\max}$ of each objective function $f_i(\mathbf{x})$ will be calculated under the given constraints. By considering the minimum and maximum value as well as the rate of increase of membership of satisfaction, a DM will decide the membership function $\mu_{f_i}(\mathbf{x})$ based on his/her subjective judgement. By assuming that μ_{f_i} is a strictly monotone increasing and

continuous function, the membership function of the fuzzy goal for each of the objective functions, $f_i(\mathbf{x})$, $i = 1, \ldots, p$, can be defined by

$$\mu_{f_i}(\mathbf{x}) = \begin{cases} 1, & \text{if } f_i(\mathbf{x}) > f_i^2 \\ d_i(f_i(\mathbf{x})), & \text{if } f_i^1 \le f_i(\mathbf{x}) \le f_i^2 \\ 0, & \text{if } f_i(\mathbf{x}) < f_i^1 \end{cases} \tag{5.3}$$

where $f_i^{\min} \le f_i^1 \le f_i^2 \le f_i^{\max}$ and $d_i(f_i(\mathbf{x}))$ is a strictly monotone increasing and continuous function with respect to $f_i(\mathbf{x})$ and may be linear or nonlinear such as quadratic or exponential. Note that this function will be strictly decreasing and continuous in the problem seeking the minimum of objectives.

After determining the membership function for each of the objective functions, to generate a candidate for the compromise or satisfactory solution, each DM is asked to specify his/her target value of the membership function, called the threshold, with which s/he might at least be satisfied. Let $\bar{\mu}_{f_i}$ be the threshold for the objective function, $f_i(\mathbf{x})$.

5.2. Heuristic for searching the set of weight factors

Usually, many researchers have studied minmax problem (Sakawa et al. 1987; Mahapatra and Maiti 2005), in which the membership value of each objective function is penalized only when it is less than the threshold; therefore the policy is to increase the membership value beyond the threshold whenever possbile. With growing the number of DMs involved in this problem, the philosophy that penalizes only the under-achievement in a objective function should be adjusted to the situation with multiple DMs. In this Chapter, over-achievement as well as under-achievement in a objective function will be

penalized like early-tardy heuristic by Prabhu (1995). Actually, this strategy that assigns the penalty to both over- and under-achievement in an objective function has been common in scheduling problems in which penalties have been assigned for early and tardy completion of jobs. When there are multiple DMs involved in an MOLP problem, under-achievement in a objective function might not be accepted by the DM who manages the objective function. In addition, over-achievement in an objective function, which usually causes under-achievement in one or more objective functions, also could not be accepted by the other DMs. Therefore, the local goal for each objective function by individual DM is to minimize the absolute value of the difference between the threshold and the membership value:

$$g_i = \left| \bar{\mu}_{f_i} - \mu_{f_i} \right| \tag{5.4}$$

where $\bar{\mu}_{f_i}$ and μ_{f_i} are the threshold and the membership value for the *i*-th objective function, respectively. By adopting the absolute value for the goal, the membership value of an objective function can be increased to meet its threshold and penalize it in both over- and under-achievement of the objective function. The global goal for all *p* objective functions by all *p* DMs is to minimize average membership value deviation of all objective functions:

$$G = \frac{1}{p} \sum_{i=1}^{p} g_i . \tag{5.5}$$

If *G* is '0', then the local goals of the objective functions are globally coherent and optimal, satisfying both the individual objective functions and the global goal. If *G* is not '0', then the local goals are not necessarily optimal and the heuristic is used to generate

the new set of weight factors with better global merit. As a result, instead of a minimax problem, this Chapter will focus on minimizing the deviation of the membership value from the threshold of an objective function.

In most interactive approaches, the best compromise solution can be reached by either searching for the optimal weight set or successively reducing the weight factors space $\Lambda = \{\lambda \mid \sum \lambda_i = 1, \lambda_i \geq 0\}$ for the P_λ problem shown in Eq. 5.2. By searching the weight factors space based on a DM's preference, the compromise solution may be reached. While these methods are based on a DM's preference of the given solution for which he should compare the value of the whole objective functions, multiple DMs' preferences can not be considered by those methods.

In the heuristic, each weight factor of the objective functions will be adjusted by the weight factor controller associated to each objective function, which uses a local control law and local feedback without any knowledge about other DMs. Therefore, the heuristic can be viewed as a local "closed-loop" heuristic finding "best" set of weight factors because it uses the result of solution as feedback to modify the individual weight factor for use in the next iteration, illustrated in Figure 5.1.

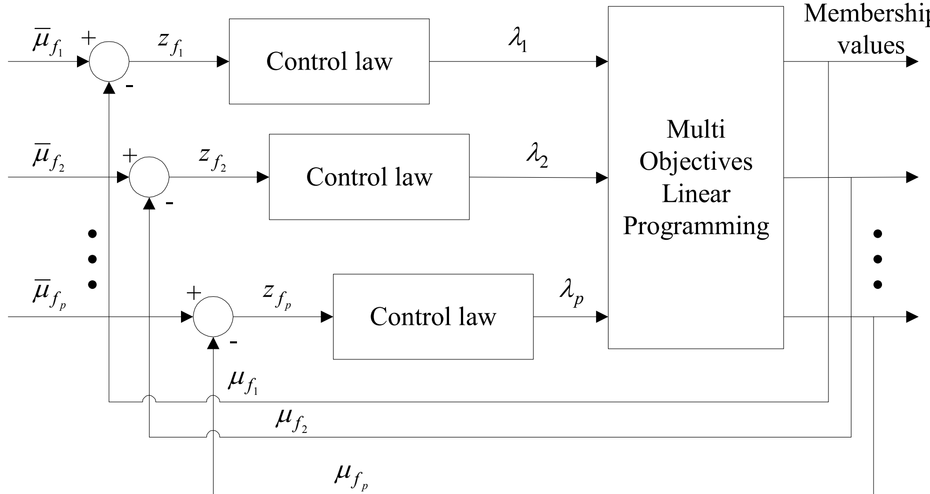

Figure 5.1. "Closed-loop" structure of the proposed heuristic

Figure 5.1 shows the closed loop structure of the proposed heuristic to find out the set of weight factors for the “best” compromise or satisfactory solution, where $\bar{\mu}_{f_i}$ is the threshold, μ_{f_i} is the membership value, z_{f_i} is the membership value deviation from the threshold, and λ_i is the weight factor of the *i*-th objective function. Note that only the weight factor of each objective function is controlled using the difference between the membership value and the threshold after solving the MOLP problem with the given set of weight factors. As the local law, the integral control law by Prabhu (1995) is chosen and implemented equivalently to the following equation:

$$\boldsymbol{\lambda}(m) = \boldsymbol{\lambda}(0) + \mathbf{k}\left(\bar{\boldsymbol{\mu}}_f - \boldsymbol{\mu}_f(m-1) - \mathbf{M}(m-1)\right) \tag{5.6}$$

where *m* is the iteration number, $\boldsymbol{\lambda}(m)$ is the weight factor vector, $\mathbf{k}$ is the controller gain vector, $\bar{\boldsymbol{\mu}}_f$ is the threshold vector, $\boldsymbol{\mu}_f(m)$ is the membership value vector, and $\mathbf{M}(m)$ is the average vector of the deviation of the membership value from the threshold

in the m-th iteration. Note that these vectors all are p-dimensional vectors. In each iteration, the membership value vector for objective functions is obtained from solving the MOLP problem and serves as a feedback for the weight factor controller. To maintain the constraint on the weight factors as Eq. 5.2, the constant value $M(m)$, the average of the deviation of the membership value from the threshold in the m-th iteration, is subtracted in m-th iteration so that every element in $\mathbf{M}(m)$ is identical as following:

$$M(m)=\frac{\sum_{i=1}^{p}\left(\overline{\mu}_{f_i}-\mu_{f_i}(m)\right)}{p}. \qquad (5.7)$$

By the subtraction, the sum of the weight factors will be maintained as 1 in each iteration.

At the end of iteration, each local goal shown in Eq. 5.4 will be computed based on the calculated membership value and the global performance as Eq. 5.5 will be calculated based on the every local goal of the p objective functions. The set of weight factors with the best global performance among those discovered in iterations can be used to generate the compromise or satisfactory solution based on the acceptance value of every DM, namely the threshold. The resultant heuristic can handle the complex situation involving multiple DMs who have different interest or preference from the others.

5.3. New algorithm

Following the discussion about the heuristic based on the "close-loop" control to search the set of weight factors, a general algorithm, which derives the compromise solution for multiple DMs from the efficient solution set especially from MOLP

problems, can be summarized as follows. First, the controller gain k_i ($k_i > 0$) for each of objective functions is determined, this in turn will determine how the weight factors are changed. Higher k_i will increases the convergence rate. In addition, the termination criterion τ, is also defined at this time. In next step, the maximum $f_i^{\max}$ and minimum $f_i^{\max}$ of each of objective functions, $f_i(\mathbf{x}),\ i = 1,\ldots,p$, are calculated to help DMs define the membership function defined in Eq. 5.3. In next step, every DM will be interviewed with providing both $f_i^{\max}$ and $f_i^{\max}$ obtained in previous step to elicit a membership function $\mu_{f_i}(\mathbf{x})$ of the objective function $f_i(\mathbf{x})$ which he/she manages. Many types of the membership function have been studied: linear, exponential, hyperbolic, hyperbolic-inverse, and piecewise-linear functions (Sakawa, Yano and Yumine 1987). Every DM can choose the type of the membership function from this list. In next step every DM should set the threshold $\overline{\mu}_{f_i}$ for the objective function $f_i(\mathbf{x})$. From next step, the proposed heuristic in Section 5.3 proceeds to find the set of weight factors $\lambda_i, i = 1,\ldots,p$. To do that, the set of weight factors and the best global goal are initialized. The set of the weight factors will be initialized as an arbitrary set $\Lambda^0 = \{\lambda \mid \lambda_i = 1/p,\ \text{for all}\, i\}$, which means that all the objective functions are given same weight factor. The initial best global goal, G_{best}^0, also should be initialized as *1,* the worst case. In next step, the MOLP problem transformed into P_λ problem formulation in Eq. 5.2 using the given weight factors is solved, providing the values of every objective function for the given weight factors. The membership value of p objective functions are calculated from the membership functions elicited by the DMs. The next step calculates the deviation of the

membership value from the threshold for every objective function, then calculating the local goals for every objective functions using Eq. 5.4 and the global goal using Eq. 5.5. Comparing this present global goal with the previous stored best global goal, the old best global goal is replaced with the present global goal when there is an improvement in the present global goal, namely the decrease of the global goal. In this case, it can jump to the steps in which new weight factors are calculated. The algorithm will stop the heuristic process when there is no improvement in the global goal over certain iterations τ. If there is any negative weight factor, the heuristic will stop. Otherwise, the newly generated set of the weight factors, $\Lambda^m = \{\lambda \mid \lambda_i, \text{ for all } i\}$, will be provided into new iteration of the heuristic. After the heuristic stops, the efficient solution with the present best global goal is presented to every DMs. When anyone of them changes his/her mind, this algorithm can be restarted from the second step, in which any unsatisfied DM can change the membership function and/or threshold of his/her objective function. Otherwise, for new iteration, in next steps, the new set of the weight factors should be calculated using Eq. 5.6. As shown in Eq. 5.6, the average of the deviation of the membership value from the threshold, $M(m)$, is calculated using Eq. 5.7. In next step, the new set of weight factors is generated using the feedback control method in Eq. 5.6. This newly generated weight factors will be provided into new iteration of the heuristic. Figure 5.2 summarizes the steps of the proposed algorithm.

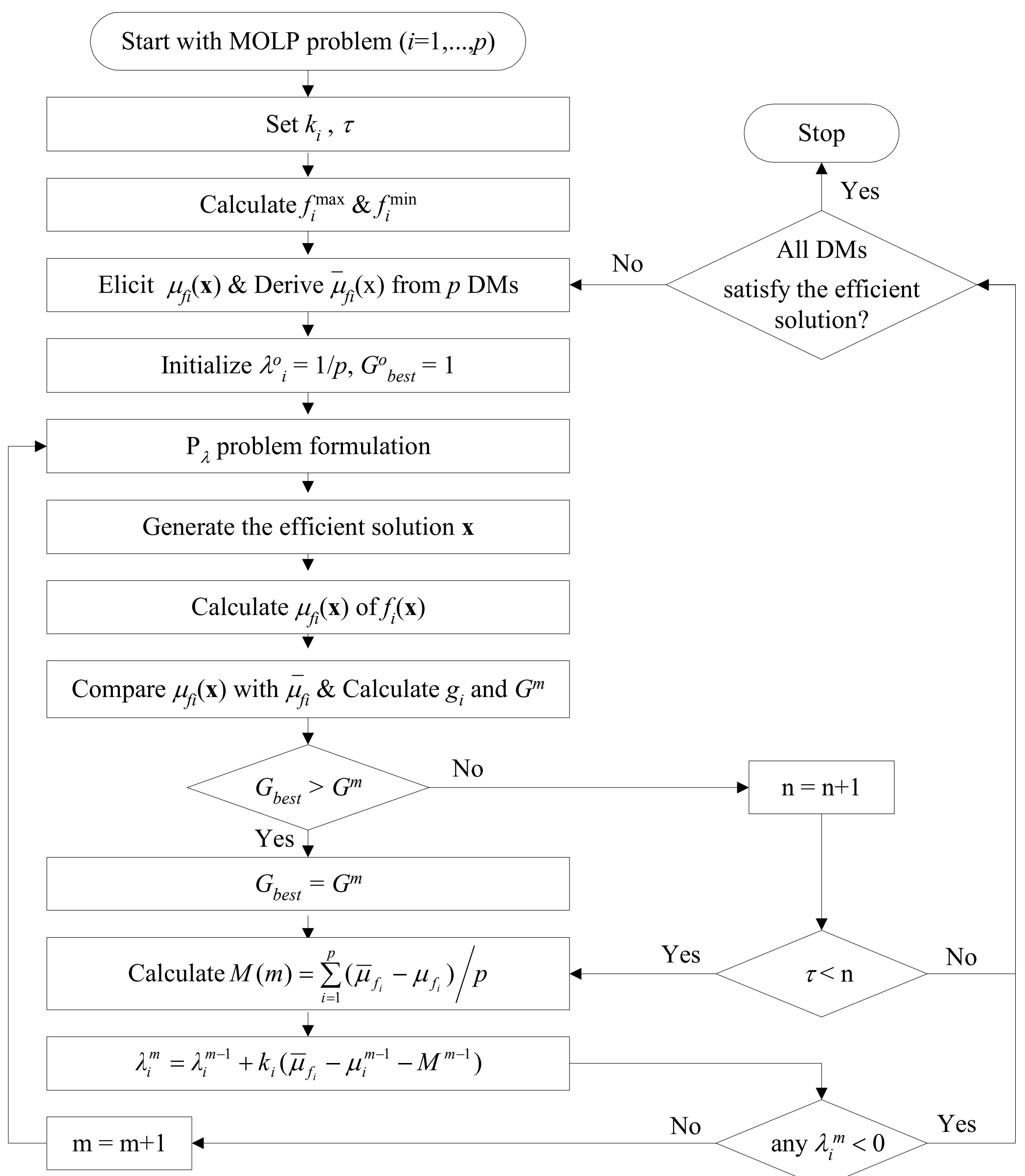

Figure 5.2. Flowchart for the proposed algorithm

5.4. Optimization problem formulation for EB-PVD process

The problem considered is the Pareto optimal selection of a set of variables of EB-PVD process for the TBC made of YSZ. Table 5.1 summarizes variables, concerned

by multiple decision makers from various areas such as management, process planning, product design, and customer, as well as their units; Table 5.2 lists the constants and the variables in Table 5.1are restricted as follows:

$$X_i \geq 0,\ i = 1,2,\cdots,24 \qquad (5.8)$$

Table 5.1. Variables of EB-PVD process

Variable	Description	Variable	Description
X1	Cost of Material	X12	Effective vertical distance (mm)
X2	Cost of Energy	X13	Actual distance between source and substrate (mm)
X3	Mass emitted by source (g)	X14	Maximum Radius (mm)
X4	Total process-time (s)	X15	Mass collected on substrates (g)
X5	Evaporation rate (g/s)	X16	Number of substrates
X6	Minimum thickness (mm)	X17	Index of Diameter
X7	Deposition rate (mm/s)	X18	Index of Columnar
X8	Vapor pressure (mmTorr)	X19	Pressure/30
X9	Melt pool temperature (K)	X20	$\frac{\text{Substrate temperature}}{\text{Melting temperatuer of substrate}}$
X10	Rotation speed (RPM)	X21	RPM/30
X11	EB power (kW)		

Table 5.2. Constants for optimization problem of EB-PVD

Constant	Description	Constant	Description
Km	Price per gram ($/g)	Kais	Area of ingot surface (mm^2)
Ker	Constant for evaporation rate	Kmw	Molecular weight (g)
Ke	Price per kilowatthour ($/Whr)	Kvd	Virtual source heigth factor
Kd	Density (g/mm^3)	Kas	Area of a substrate (mm^2)
Kmp	Melting point of ingot (K)	Kbp	Boiling point of ingot (K)
Kmps	Melting point of substrate (K)	Kecp	Constant for vapor pressure
Kesr	Constant for substrate rotation		

The system model will be developed under assumptions as follows:

a. All substrates have the same shape and area; substrate temperature remains constant as pre-heating temperature.
b. Only one ingot is used in the process and the composition maintains it orig inal configuration all over the deposition.
c. The rotation axis of the substrate holder is perpendicular to the ingot surfac e, with which the holder of a planar shape is coaxial.
d. The coater is batch-type machine with the features of planetary geometry, water loading on the planet, pump down time, etc.
e. Both labor and equipment cost are constant and can be ignored.

The four criteria (manufacturing cost, uniformity of coating thickness, collection efficiency of material on substrate and lifetime) are described below.

5.4.1 Production cost

Hill (1986) developed production cost analysis for industrial PVD system with the help of the cost analysis program which combines physical models of deposition processes with cost assumption to evaluate industrial processes with respect to production rate (throughput) and production cost. The four principal cost parameters were considered: material, electric power, direct labor, coater equipment. In this section, based on the assumption (e), only both material and electric power are considered to estimate the production cost of TBC using EB-PVD. The main factor affecting both parameters is

total process-time (X4). While achieving requirements for TBC, minimizing the coating time and minimizing the amount of material evaporated are necessary to gain the goal of production cost. Minimum thickness specification (X6) is also important to determine the amount of material used as well as the electric power used. The production cost of TBC (COST) is obtained by

$$\mathrm{COST} = \mathrm{X1} + \mathrm{X2} \tag{5.9}$$

where the objective is minimizing the production cost of TBC (COST).

The cost of material (X1) is greater than the cost for the mass emitted by source (X3) calculated as follows:

$$\mathrm{X1} > \mathrm{Km} \cdot \mathrm{X3} \tag{5.10}$$

where X3 is given from the total process-time (X4) and the evaporate rate (X5) as follows:

$$\mathrm{X3} = \mathrm{X4} \cdot \mathrm{X5} \tag{5.11}$$

where the total process-time (X4) is larger than the time to make the minimum thickness (X6) with the deposition rate (X7) as follows:

$$\mathrm{X4} \geq \mathrm{X6} / \mathrm{X7}, \tag{5.12}$$

and, based on the assumptions that the specific evaporation rate (Langmuir 1913) is constant over the whole surface of melt pool and that the saturated vapor pressure at a melt pool's temperature is similar to the chamber pressure (X8), the evaporate rate (X5) can be computed, as follows:

$$\mathrm{X5} = \mathrm{Kais} \cdot \left[\mathrm{Ker} \cdot \mathrm{X8} \cdot \left(\frac{\mathrm{Kmw}}{\mathrm{X9}} \right)^{1/2} \right]. \tag{5.13}$$

Yamaguchi et al. (2003) investigated YSZ deposition upon a plate over vapor source at difference input powers and kinematics modes. They provided the graphs showing the relation between the deposition rate and EB-PVD process parameters like the rotation

speed (X10) and the EB power (X11). To develop the equation for the deposition rate (X7) from the regression model of X10 and X11, the least squre method (Johnson and Wichern 2002) is applied and resulting equation of the depositio late is

$$\begin{aligned} X7 &= -3.92 + 10.2 \cdot \{1 - 0.3[1 + \text{sign}(X10 - 0.5)]\} \\ &\quad + 0.894 \cdot [-5.82 + 0.221 \cdot X11] \end{aligned} \quad (5.14)$$

where sign(·) is -1 for a negative number, 0 for the number zero, or 1 for a positive number.

The cost of energy (X2) is calculated from the total process-time (X4) and the input energy which contains EB power (X7) as well as the chamber pressure (X8) and substrate rotation (X10) as follows:

$$X2 > Ke \cdot X4 \cdot \left[X11 + \frac{Kecp}{X8} + Kesr \cdot X10 \right]. \quad (5.15)$$

5.4.2. Uniformity of coating thickness

The cosine law of emission models the directionality of evaporating molecules and the shape of the vapor plume (Glang 1970). Its variants have been used in several evaporation applications to model coating thickness of simple planar substrates (Schiller et al. 1982; Pulker 1984). In the Schiller' model that is one of the deposition process models explained in Chapter 2, the normalized value for the coating thickness at any point with respect to that at a given point where the deposition rate was calculated. Hill (1988) proposed similar model to it only using vertical distance and radius from center of rotation and measured the uniformity of coating thickness (UNIFORM) with the model. Since EB-PVD is primarily a line-of-sight process, uniform coating is accomplished by continuous rotation in the vapor cloud during the deposition process (Singh and Wolfe

2005). Cho et al. (2005) developed an heuristic for EB-PVD process to find ‘best’ motion plan with the objective of reducing coating thickness variance, namely the uniformity of coating thickness.

In this section, the uniformity of coating thickness is defined as the minimum ratio of coating thickness that the ratio is measured using the model proposed by Hill (1986). Instead of the actual source-to-substrate distance (X13), he used the effective vertical distance (X12) that means a new value for the X13. After fitting the measured curve of the distribution of coating thickness to the calculated curve of that by varying the X13, the virtual source height factor (Kvd) is decided, with which the X12 is obtained by

$$\mathrm{X12} = \mathrm{X13/Kvd} \tag{5.16}$$

From the effective vertical distance (X12) and the maximum radius (X14), UNIFORM can be defined as follows:

$$\mathrm{UNIFORM} = \left[1+\left(\frac{\mathrm{X14}}{\mathrm{X12}}\right)^{2}\right]^{-2} \tag{5.17}$$

where the objective is maximizing the uniformity of coating thickness (UNIFORM).

5.4.3. Collection efficiency of material on substrate

There have been several metrics developed to estimate the collection efficiency of material on substrate (COLLECT) (Hill 1986; Fuke et al. 2005). Hill directly considered both emitted materials and deposited materials; Fuke et al. used the ratio of the area of vapor plume subtended on substrate and total area of vapor plume. In this section, Hill’s approach is applied to define COLLECT of TBC by EB-PVD. Therefore, the COLLECT

is the ratio of mass collected on substrates (X15) and mass emitted by sources (X3). The model for predicting the COLLECT will be derived by two steps: i) determining the X15 from the total volume of coating on all the substrate which can be approximated using the minimum coating thickness (X6) and the uniformity of coating thickness (UNIFORM) in Eq. 5.17 and ii) calculating the ratio of both the X15 and X3. The resulting equation of the COLLECT is given by

$$\begin{aligned} X15 &> \{Kd \cdot [X16 \cdot (Kas \cdot X6)]\}/UNIFORM \\ COLLECT &= X15/X3 \end{aligned} \qquad (5.18)$$

where the objective is maximizing the collection efficiency of material on substrate (COLLECT).

5.4.4. Coating lifetime

The original function of TBC is to increase the life of components which it protects (Bose and DeMasi-Marcin 1997). Thus, optimal TBC can be said to have a long lifetime as well as low density (Schulz et al. 2002). TBC lifetime (LIFE) was tested using the cyclic lifetime, which can be obtained from furnace rig test (Schulz et al. 1997). They found that the microstructure of TBC is one of critical factors to the cyclic lifetime; the effect of rotation speed and surface temperature, which mainly affect the microstructure of TBC, on the cyclic lifetime were investigated. According to them, both diameter and the structure of columnar were main factors of the microstructure of TBC that affected the cyclic lifetime. Therefore, the model for predicting TBC lifetime will be derived by two steps of regression analysis: i) replacing diameter and column by index X17 under 15 and index X18 under 10, respectively, then, estimating the regression models for the

prediction of X17 and X18 from normalized process parameters of pressure, temperature, and rotation speed (X19, X20, and X21, respectively), ii) developing the equation for TBC lifetime from the regression models of X17 and X18. For the simplicity, the effect of vapor pressure on the cyclic lifetime is ignored. The models can be obtained by the least square method (Johnson and Wichern 2002). The resulting equation of TBC lifetime is

$$\begin{aligned} X17 &= -12.37 + 45.44 \cdot X19 + 33.55 \cdot X20 - 19.9 \cdot X21 \\ &\quad - 47.53 \cdot (X19)^2 + 19.25 \cdot (X21)^2 \\ X18 &= 0.478 - 1.85 \cdot X19 + 11.263 \cdot X20 - 0.311 \cdot X21 \\ &\quad + 16.396 \cdot X19 \cdot X21 \\ LIFE &= -274 - 1456 \cdot X17 + 1521 \cdot X18 \end{aligned} \tag{5.19}$$

where R-Sq(adj) = 88.5% for X17, R-Sq(adj) = 58.4% for X18, and the objective is maximizing the TBC lifetime (LIFE). Transforming the arrangement of columns into numerical index caused the low low R-Sq(adj) for X18.

5.4.5. Multi-criteria problem formulation

There are physical limitations of the EB-PVD coater as follows:

$$X_i^{\min} \le X_i \le X_i^{\max},\ i = 1,2,\cdots,24 \tag{5.20}$$

where $X_i^{\min}$ means the minimum value of X_i, and $X_i^{\max}$ means the maximum value of X_i. The physical constraints on various dynamics during the EB-PVD processing, which should be considered into the optimization problem. They are:

- The mass collected on substrate is assumed to be smaller than 50% of the mass emitted by source.
- In a time period, the evaprorate rate should be greater than the deposited mass

- The mass collected on substrate is same the mass calculated from the deposition rate and the total process-time

These physical constraits can be expressed as follows:

$$\begin{aligned} & X15 < 0.5 X3 \\ & Kd \cdot Kas \cdot X16 \cdot X7 < X5 \\ & X4 \cdot X7 = X15 \end{aligned} \tag{5.21}$$

The two normalized process parameters of pressure and rotation speed (X19 and X21, respectively) have the relationship with oritinal variables:

$$\begin{aligned} & X8 = 30 \cdot X19 \\ & X10 = 30 \cdot X21 \end{aligned} \tag{5.22}$$

The optimization problem to select a set of variables of EB-PVD process for the TBC made of YSZ can be formulated as the multi-criteria problem which has the four-criterion related constraints in Eq. 5.12-5.19 and the physical constraints in Eq. 5.20-5.22 as follows:

$$
\begin{aligned}
&\min\ \text{COST} \\
&\max\ \text{UNIFORM} \\
&\max\ \text{COLLECT} \\
&\max\ \text{LIFE} \\
&\text{subject to} \\
&X1 + X2 = \text{COST} \qquad \left[1 + \left(\frac{X14}{X12}\right)^2\right]^{-2} = \text{UNIFORM} \\
&X15/X3 = \text{COLLECT} \quad -274 - 1456 \cdot X17 + 1521 \cdot X18 = \text{LIFE} \\
&Km \cdot X3 < X1 \quad Ke \cdot X4 \cdot \left[X11 + \frac{Kecp}{X8} + Kesr \cdot X10\right] < X2 \\
&X4 \cdot X5 = X3 \qquad X6/X7 \le X4 \\
&Kais \cdot \left[Ker \cdot X8 \cdot \left(\frac{Kmw}{X9}\right)^{1/2}\right] = X5 \\
&\begin{pmatrix} -3.92 + 10.2 \cdot \{1 - 0.3[1 + \text{sign}(X10 - 0.5)]\} \\ + 0.894 \cdot [-5.82 + 0.221 \cdot X11] \end{pmatrix} = X7 \\
&X13/Kvd = X12 \quad \{Kd \cdot [X16 \cdot (Kas \cdot X6)]\} / \text{UNIFORM} < X15 \\
&\begin{bmatrix} -12.37 + 45.44 \cdot X19 + 33.55 \cdot X20 - 19.9 \cdot X21 \\ -47.53 \cdot (X19)^2 + 19.25 \cdot (X21)^2 \end{bmatrix} = X17 \\
&0.478 - 1.85 \cdot X19 + 11.263 \cdot X20 - 0.311 \cdot X21 + 16.396 \cdot X19 \cdot X21 = X18 \\
&X_i^{min} \le X_i \le X_i^{max} \ \text{for all } i \\
&X15 < 0.5X3 \qquad Kd \cdot Kas \cdot X16 \cdot X7 < X5 \qquad X4 \cdot X7 = X15 \\
&30 \cdot X19 = X8 \qquad 30 \cdot X21 = X10 \\
&\text{COST, UNIFORM, COLLECT, LIFE} \ge 0, \text{COLLECT} \le 1
\end{aligned}
\tag{5.23}
$$

Substrate manipulation in the high intensity region of vapor plume can potentially improve the coating uniformity, the coating time, and the amount of material evaporated. However, this may reduce the total amount of the evaporated material that is deposited on the work-piece (Cho, Fuke and Prabhu 2005). Therefore, the optimization problem in Eq. 5.23 has no optimal solution but Pareto optimal solution, or efficient solution.

5.5. Case study for Pareto optimal solution of TBC design

In this section, the multi-criteria problem is will be solved, which includes the ten Inconel IN738 LC substrates 60 mm long in y-axis direction and 20 mm wide in x-axis direction and 2.5 mm thick in z-axis direction which is mounted side by side at a planar holder 300 mm above the surface ingot. The optimization problem in Eq. 5.23 should be simplified to linear problem. To do this, following are the assumptions to the variables in Eq. 5.23:

i. COLLECT can be divided into maximizing COLLECT1 and minimizing COLLECT2
ii. The temperature of melt pool (X9) remains constantly at Kmp+0.35(Kbp -Kmp)
iii. The rotation speed (X10) is greater than 0.5rpm, resulting in that the X21 is greater than 0.0167
iv. The square terms of and interaction term between X19 and X21 in Eq. 5.19 can be negligible
v. The virtual source height factor (Kvd) = 1, resulting in that the effective vertical distance (X13) becomes same with the X12 (=300mm)
vi. The evaporation coefficient becomes 1 for idealized evaporation
vii. Nonlinear functions in Eq. 5.11, 5.12, 5.15, and 5.21 can be approximated as linear functions, as shown in Table 5.3.

The given conditions of variables in Table 5.1 and 5.2 are listed in Table 5.4. The limitations of the variables in Eq. 5.23 are summarized in Table 5.5.

Table 5.3. Approximated linear functions

# of Eq.	Approximated linear function
Eq. 5.11	$10 \cdot X4 + 10 \cdot X5 \geq X3 \geq X4 + X5$
Eq. 5.12	$10^4 X6 \geq X4 \geq 10^2 X6$
Eq. 5.15	$X4 + X11 + 1000X10 - 100X8 \geq X2$ $X2 \geq X4 + KeX11 + 1000Ke \cdot KecpX10 - 100Ke \cdot Kesr \cdot X8$
Eq. 5.21-	$0.05 (X4 + X7) \geq X15 \geq 0.0001 (X4 + X7)$

Table 5.4. Conditions of EB-PVD process for the case study of TBC made of YSZ

Variable	Value	Constraint	Value	Constraint	Value
X9	3249	Km	0.025	Kas	1200
X10	> 0.5	Kais	3117.245	Kmp	2988
X12	300	Ker	0.00044	Kbp	3733.15
X13	300	Kmw	127.6105	Kmps	1588.5
X14	100	Ke	0.045	Kecp	1
X16	10	Kvd	1	Kesr	1
X21	>0.0167	Kd	$6.0*10^{-6}$		

Table 5.5. Limitations of the variables of EB-PVD process

Variable	Unit	X_i^{min}	X_i^{max}	Variable	Unit	X_i^{min}	X_i^{max}
X3	g	10	1200	X11	kW	20	65
X4	sec	1	3600	X15	g	0	1200
X5	g/s	0.01	1	X17		1	15
X6	mm	0.01	2	X18		1	10
X7	mm/s	10^{-6}	0.05	X19		0.0333	1
X8	mmTorr	1	30	X20		0.3	0.7
X10	RPM	0.5	30	X21		0.0167	1

With the assumptions above and the given conditions in Table 5.3, 5.4, and 5.5, the optimization problem in Eq. 5.23 is simplified in Eq. 5.24, where an inequality can be converted to an equation by adding a nonnegative slack variable.

$$
\begin{aligned}
&\min \mathrm{COST} \\
&\max\ \mathrm{COLLECT1} \\
&\min\ \mathrm{COLLECT2} \\
&\max\ \mathrm{LIFE} \\
&\text{subject to} \\
&\mathrm{X1}+\mathrm{X2}=\mathrm{COST} \quad \mathrm{COLLECT1}=\mathrm{X15} \quad \mathrm{COLLECT2}=\mathrm{X3} \\
&-274-1456\cdot\mathrm{X17}+1521\cdot\mathrm{X18}=\mathrm{LIFE} \qquad 0.09\mathrm{X6}<\mathrm{X15} \\
&0.03\cdot\mathrm{X3}<\mathrm{X1} \quad \mathrm{X5}+\mathrm{X4}\le\mathrm{X3}\le 10(\mathrm{X5}+\mathrm{X4}) \\
&\mathrm{X4}+0.045\cdot(\mathrm{X11}+1000\mathrm{X10}-100\mathrm{X8})<\mathrm{X2} \\
&\mathrm{X2}<\mathrm{X4}+\mathrm{X11}+1000\mathrm{X10}-100\mathrm{X8} \\
&10^2\cdot\mathrm{X6}<\mathrm{X4}<10^4\cdot\mathrm{X6} \quad 0.3\cdot\mathrm{X8}=\mathrm{X5} \quad -5+0.2\cdot\mathrm{X11}=\mathrm{X7} \\
&-12.37+45.44\cdot\mathrm{X19}+33.55\cdot\mathrm{X20}-19.9\cdot\mathrm{X21}=\mathrm{X17} \\
&0.478-1.85\cdot\mathrm{X19}+11.263\cdot\mathrm{X20}-0.311\cdot\mathrm{X21}=\mathrm{X18} \\
&30\cdot\mathrm{X19}=\mathrm{X8} \quad 30\cdot\mathrm{X21}=\mathrm{X10} \quad \mathrm{X15}<0.5\mathrm{X3} \quad 0.07\cdot\mathrm{X7}<\mathrm{X5} \\
&0.0001(\mathrm{X4}+\mathrm{X7})\le\mathrm{X15}\le 0.05(\mathrm{X4}+\mathrm{X7}) \\
&\mathrm{X}_i^{\min}\le\mathrm{X}_i\le\mathrm{X}_i^{\max}\ \text{for all i} \\
&\mathrm{COST},\mathrm{COLLECT1},\mathrm{COLLECT2},\mathrm{LIFE},\mathrm{X}_i\ge 0
\end{aligned}
\tag{5.24}
$$

Since the uniformity of coating thickness (UNIFORM) is fixed to be 0.81, Eq. 5.24 includes four criteria in it. There are assumed three DMs, among whom DM_1 deals with only COST (f_1) , DM_2 deals with COLLECT1 (f_2) and COLLECT2 (f_3), and DM_3 deals with only LIFE (f_4). In the following, the proposed heuristic is set up within Matlab and an interface (Ferris 1998) is used to pass the set of weight factors to GAMS where P_λ problem is solved and the efficient solution is provided. Let $k_i = 0.005$ for all i and $\tau = 50$. Therefore, if there is no improvement in the global merit over 50 iterations the heuristic stop. $f_i^{\min}$ are 7.5, 9×10^{-4}, 10, and 147 for i=1,…,4, respectively and $f_i^{\max}$ are 369, 60, 1200, and 6980 for i=1,…,4, respectively. The objective function of P_λ problem is fomulated with the normalized crteria with their $f_i^{\max}$ as follows:

$$
\begin{aligned}
&\max \mathrm{Z}=\lambda_1 Z_1+\lambda_2 Z_2+\lambda_3 Z_3+\lambda_4 Z_4 \\
&Z_1=\frac{\mathrm{COST}}{f_1^{\max}}, Z_2=\frac{\mathrm{COLLECT1}}{f_2^{\max}}, Z_3=\frac{\mathrm{COLLECT2}}{f_3^{\max}}, Z_4=\frac{\mathrm{LIFE}}{f_4^{\max}}\cdot
\end{aligned}
\tag{5.25}
$$

where $0 \le Z_i \le 1$, i=1,…,4. To experiment the effect of various membership functions on

the performance of this heuristic, it is assumed that DM_1 select the linear type, DM_2 the quadratic type, and DM_3 the exponential type for $\mu_{Z_i}(\mathbf{x})$ as shown in Table 5.6, where $f_i^{\min}$ and $f_i^{\max}$ is transformed into $Z_i^{\min}=0$ and $Z_i^{\max}=1$, respectively.

Table 5.6. Membership functions selected for the experiment

i	Membership function μZi(x)	Graph of μfi(x)
1	$\mu_{Z_1}(\mathbf{x})=\begin{cases}1, & \text{if } Z_1(\mathbf{x})<0.2\\ \dfrac{(0.8-Z_1(\mathbf{x}))}{0.6}, & \text{if } 0.2\le Z_1(\mathbf{x})\le 0.8\\ 0, & \text{if } f_1(\mathbf{x})>0.8\end{cases}$	
2	$\mu_{Z_2}(\mathbf{x})=\begin{cases}1, & \text{if } Z_2(\mathbf{x})>0.9\\ \left[\dfrac{Z_2(\mathbf{x})}{0.9}\right]^2, & \text{if } 0\le Z_2(\mathbf{x})\le 0.9\\ 0, & \text{if } Z_2(\mathbf{x})<0\end{cases}$	
3	$\mu_{Z_3}(\mathbf{x})=\begin{cases}1, & \text{if } Z_3(\mathbf{x})<0\\ [1-Z_3(\mathbf{x})]^2, & \text{if } 0\le Z_3(\mathbf{x})\le 1\\ 0, & \text{if } Z_3(\mathbf{x})>1\end{cases}$	
4	$\mu_{Z_4}(\mathbf{x})=\begin{cases}1, & \text{if } Z_4(\mathbf{x})>1\\ 1-e^{-5\left\{\frac{Z_4(\mathbf{x})-0.5}{0.5}\right\}}, & \text{if } 0.5\le Z_4(\mathbf{x})\le 1\\ 0, & \text{if } Z_4(\mathbf{x})<0.5\end{cases}$	

Let the thresholds for each objective function be [0.5, 0.5, 0.5, 0.5], determined by the 3 DMs. To start the iteration of searching the "best" set of weight factors, let

$\lambda_i=1/4$ for all i since $p=4$ and $G_{best}^0=1$ which means the worst scenario. These two values are temporary and will be updated during the heuristic. Figure 5.3 summarizes the various results, such as (a) the weight factors, (b) the value of objective function, (c) the

membership value, and (d) the best global goal. DMs changed the threshold of the objective function thrice without changing the membership function as seen in Table 5.7.

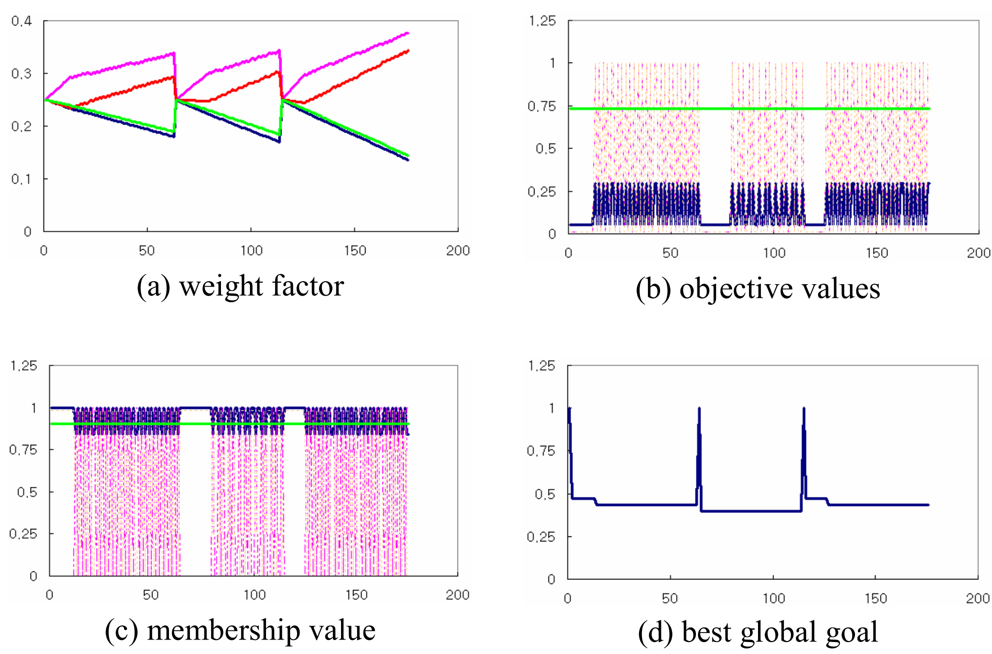

Figure 5.3. The results from numerical example of the proposed algorithm

Table 5.7. Best value with respect to interview with DMs

# of Interview / Value	1	2	3
Threshold	[0.5 0.5 0.5 0.5]	[0.5 0.5 **0.8** 0.5]	[0.5 **0.8** 0.8 0.5]
best weight factors	[0.23 0.29 0.23 0.24]	[0.25 0.25 0.25 0.25]	[0.23 0.30 0.24 0.23]
best objective function	[0.30 1.00 1.00 0.73]	[0.05 0.01 0.01 0.73]	[0.30 1.00 1.00 0.73]
best membership value	[0.84 1.00 0.00 0.90]	[1.00 0.00 0.98 0.90]	[0.84 1.00 0.00 0.90]
best global goal	0.435	0.396	0.435

X-axis in Fig. 5.3 represents the number of iteration of the heuristic. As can be noticed in the figure, there were two interactions with DMs, when they change the threshold based on the given efficient solution and the membership value. During the first running of the heuristic, the weight factors, λ_1, λ_2, λ_3 and λ_4, were updated based on the deviation of the membership value from the threshold. As the weight factors were changed, the values of objective functions were calculated by solving P_λ problem by GAMS. The membership values of them were derived from the membership functions in Table 5.6, respectively, plotted in Fig.5.3(c). From the membership value shown in Fig. 5.3(c), the global goal for the present efficient solution was calculated and compared with the present best global goal. If there was any improvement in the global goal, this value would be replaced into the new best global goal. Otherwise, the present best global goal would last until the improvement occurred. The change of the best global goal was plotted in Fig. 5.3(d), where the first value of the best global goal was *1* and it decreased as the iteration proceeded. If there was no improvement in the best global goal over 50 iterations, the algorithm stopped and provided the result, including the value of the objective function and the membership value, as shown in Table 5.7. According to Table 5.7, the best global goal was 0.396 in second interview, where the best value of objective function was [0.05 0.01 0.01 0.73] which corresponds to COST = 19.94, COLLECT (=COLLECT1/COLLECT2) = 0.05 (=0.48/9.6), and LIFE = 5119. The decision variables of the best value of objective function are listed up in Table 5.8 where includes the given value in Table 5.4.

Table 5.8. Value of variables for the best value of objective functions

Variable	Description	Value
X1	Cost of Material	0.3
X2	Cost of Energy	19.643
X3	Mass emitted by source (g)	10
X4	Total process-time (s)	9.728
X5	Evaporation rate (g/s)	0.272
X6	Minimum thickness (mm)	0.01
X7	Deposition rate (mm/s)	0.05
X8	Vapor pressure (mmTorr)	1
X10	Rotation speed (RPM)	0.501
X11	EB power (kW)	25.787
X15	Mass collected on substrates (g)	0.489
X17	Index of Diameter	1
X18	Index of Columnar	4.503
X19	Pressure/30	0.033
X20	$\frac{\text{Substrate temperature}}{\text{Melting temperatuer of substrate}}$	0.363
X21	RPM/30	0.017

5.6. Summary

In this Chapter, a methodology is developed to derive the best compromise solution of MOLP problems when multiple DMs involve in the decision-making. A weighted sum of objective functions is assumed as a utility function, resulting in P_λ problem. The interactive fuzzy method is combined with a heuristic based on an iterative computing, called as DATC, which is originated to find “best” scheduling using the feedback control algorithm. The membership function with respect to the fuzzy goal for each of the objective functions and its threshold that represents the minimum level of

acceptance of the solution are decided by multiple DMs. The heuristic can automatically search the "best" weight set for the linear, additive utility function in the whole weight space by using membership function and threshold. It penalizes both under- and over-achievement in the objective functions. In the proposed algorithm, multiple DMs will be interviewed to decide whether they will change the membership function and/or the threshold based on the selected solution until the "best" compromise solution is selected from the efficient solution set.

For the case study, the complicated optimization problem for the EB-PVD process was suggested with the four criteria: cost (COST), uniformity of coating thickness (UNIFORM), collection efficiency of material on substrate (COLLECT), and lifetime (LIFE). To apply the heuristic the nonlinear optimization problem was simplified with the given data. The selected decision variables with respect to the best global goal are expected to be the guide line for the future process planning to accelerate the product development.

Chapter 6

Simulation-based design of EB-PVD process controller

In this Chapter, a simulation-based design of EB-PVD process controller is presented. Using simulation, a simplified model of the EB-PVD process is developed to relate current input to the EB gun and the coating thickness. This model is used to design and simulate a real-time PID controller. For simulating controlled dynamics, disturbance in input power is introduced. Simulation results are provided to indicate the controller performance. The controller uses real-time feedback from quartz-crystal microbalance (QCM) sensors. For the implementation of spatially distributed QCM sensors, the relationship between the coating thickness and the measured thickness by QCM is discussed.

6.1. Development of feedback controller

The closed-loop system considered for EB-PVD is shown in Fig. 6.1, in which a feedback control loop is constructed as a controller receives the outputs, $\boldsymbol{G}$, from the EB-PVD process and generates a new set of inputs, $\boldsymbol{u}$, to manipulate the EB-PVD process to reach the given objectives, $\boldsymbol{G_d}$, a priori, or reference points.

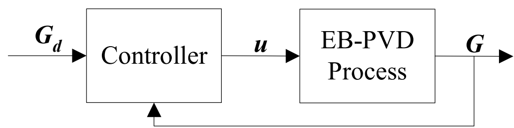

Figure 6.1. Block diagram for closed-loop process control

The success of process controller development for nanostructured coatings depends on the acquisition of data about the EB-PVD process and sensor capabilities. Due to the complexity of the EB-PVD process, a controller model of EB-PVD process is limited to off-line simulation because the intensive computational requirement would prevent real-time control. In order to implement a real-time control, a process model require simplification which can be achieved, among other way, by reducing parameters of interest or by applying a lumped-parameter approach (Koomsap, 2001). Therefore, in this Chapter, the EB-PVD process will be simplified as single-input-single-output (SISO) system.

6.1.1. Selection of system output and control parameter

After the deposition of vapor particles occurs on the surface of the substrate, the nucleus grows and develops a distinct columnar microstructure in the EB-PVD process (Maissel and Glang, 1970; Wolfe, 2001; Yamaguchi et al., 2003). When the coating grows, it incorporates defects which effect on the thermal properties of the coating (Maissel and Glang, 1970). That is, the columnar structure of crystalline shows the gap between columns (intercolumnar porosity) and finer pores and gaps in a column (intracolumnar porosity) (Yamaguchi et al., 2003). However, the availability of sensors to

measure the real time states of the microstructure of coating has been one of the obstacles in the implementation of feedback control system for nanostructured coating processes. That is, although the development of the state-of-art sensors has been reported for in situ measurement during the EB-PVD process, those sensors are not usually available in the EB-PVD coater. Therefore, the in-line measurements for the control of the EB-PVD process are based on the availability of sensors. This situation forces the implementation of conventional sensors like thermocouples and quartz crystal microbalances (QCM). Controlling the thickness of the coating is of paramount importance in any coating process (Bose and DeMasi-Marcin, 1997) and the sensor to measure, like QCM, the thickness is available to us. Thus, this microstructure feature, i.e. thickness of coating, is selected as the output of the EB-PVD process $\boldsymbol{G}$ in Fig. 6.1. Hence, the goal-state microstructure, or the objective $\boldsymbol{G_d}$, also has the same element as $\boldsymbol{G}$ as shown in Fig. 6.1.

Since the EB-PVD process starts as EB guns emit the streams of electrons, the whole states of the EB-PVD process are governed by the power of EB. Moreover, it is relatively easy to manipulate the power of EB by the well-known control techniques like PID control. There are three variables to decide the amount of the EB power: input current flowing through the cathode in an EB gun A, input potential difference across it V, and acceleration voltage applied to the EB gun U_B. The input current A is chosen as the input of the EB-PVD process $\boldsymbol{u}$ in Fig. 6.1 among the three variables, which will be manipulated by a feedback controller. The variance of input values of the three variables is considered as the main disturbance to the EB-PVD process.

6.1.2. Process modeling

In step-response modeling, only the experimental, time-domain response of the process to a step input is required to obtain a process model (Bollinger and Duffie, 1988). A step-response test can be carried out relatively quickly and is relatively easy to analyze as long as a high-order dynamic model is not required. The digital EB-PVD simulator is used to experiment the step-response test in the ideal situation which has no noise in the three variables A, B, and U_B. YSZ is selected as an ingot material. Time step T is set to be 0.05s and the simulation duration is set to be 1000s. As a step input M, input current A is fixed at 25A. The thickness of coating is calculated at a point (0, 200, 500) when the center of ingot surface is set to be the geometric origin. The step response of EB-PVD is shown in Fig. 6.2. In Fig. 6.2(a), the EB-PVD process shows a delay before it reaches an approximated integration process after 200 sec, where the step response linearly increases with time. The delay time D was 6.45s as seen in Fig. 6.2(a), which means that a discrete index d for the delay time is 130. In Fig. 6.2(b), the step response of EB-PVD can be approximated as a line, namely the integration process up to 1000s. Thus, the EB-PVD process can be approximated as a first-order process with integration. The slope of step response $dG/dt|_{ss}$ shown in Fig. 6.2(b) was 1.0814×10^{-04} (mm/s). The process gain k can be obtained as follows:

$$k = \frac{\left.\frac{dG}{dt}\right|_{ss}}{M} \tag{6.1}$$

By Eq. 6.1, the process gain of the EB-PVD was calculated to be 4.3256×10^{-06}.

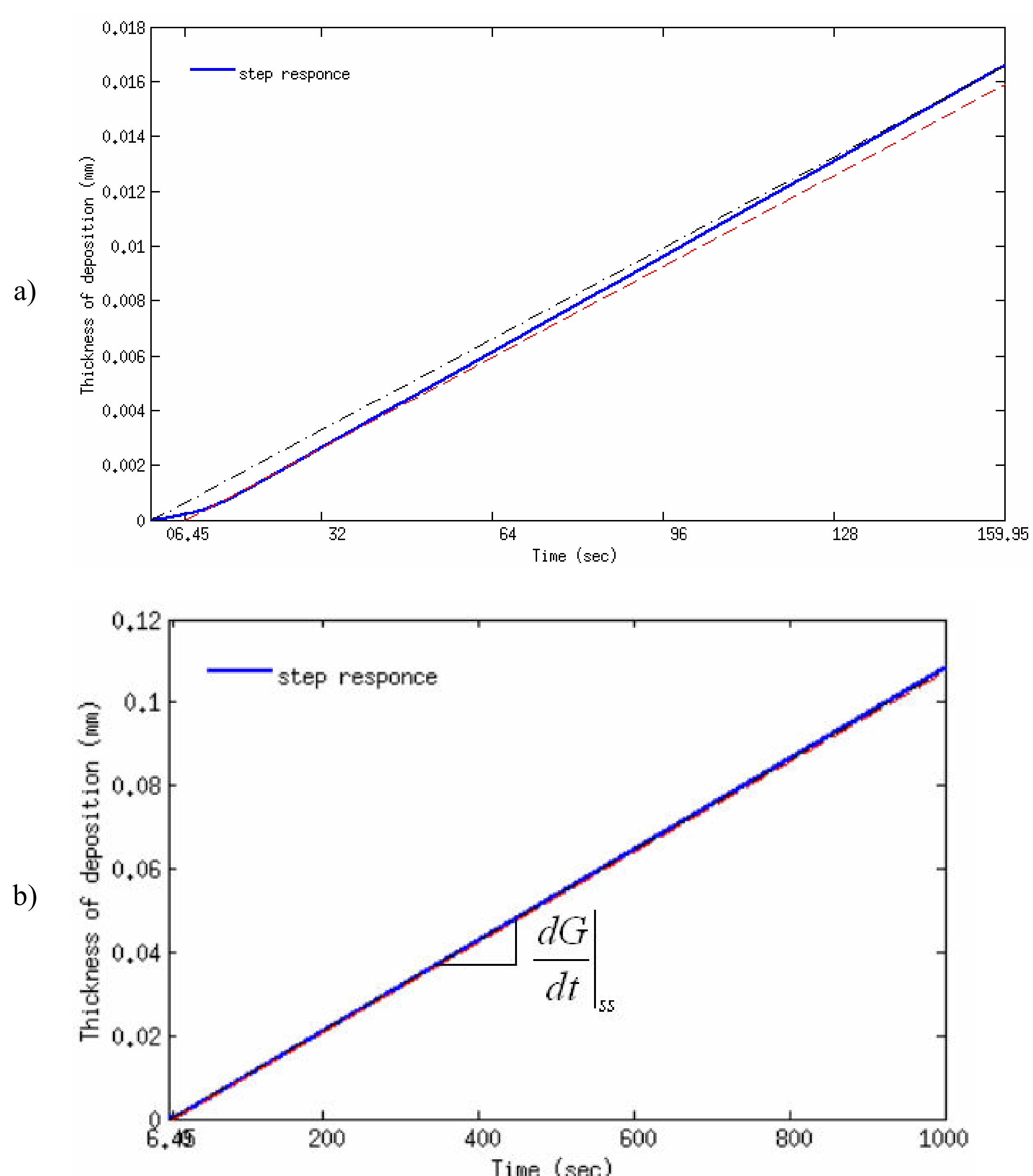

Figure 6.2. Step response of first-order process with integration: a) t = 200s, b) t = 1000s

The continuous and discrete first-order with integration can be modeled respectively as follows:

$$\frac{dG(t)}{dt} = k \cdot u(t - D) \tag{6.2}$$

$$G_n = G_{n-1} + k \cdot T \cdot u_{n-1-d} \tag{6.3}$$

where G is the output of the EB-PVD process, i.e. the thickness of coating, k is the process gain of 4.3256×10^{-06}, D is the delay time of 6.45s, T is the time step of 0.05s, d is the discrete index of 130 corresponding to the delay time, and u is the input to the EB-PVD process, i.e. the input current A to the cathode in the EB gun.

6.1.3. Open-loop response to the change and disturbance of manipulated variable

To determine the open-loop response to the change and disturbance of manipulated variable, input current A, two experiments are designed based on the simulation in the previous section. First, step changes in the input current A (±10A) are introduced at t=400s. Second, step disturbance in the three variables of the EB-gun, A, V, and U_B, (0.3) is introduced at t=400s.

Figure 6.3 shows the open-loop response of the thickness of coating with respect to step changes in the input current A (±10A) at t=400s, which means that the thickness of coating can be controlled by manipulating the input current A.

Figure 6.4 shows the response of thickness of coating with respect to step disturbance in three variables of the EB-gun, A, V, and U_B, (0.3). The disturbance in the system results in the change in the thickness of coating. Therefore, the feedback controller for the EB-PVD process needs to correct the effect of the disturbance on the coating thickness.

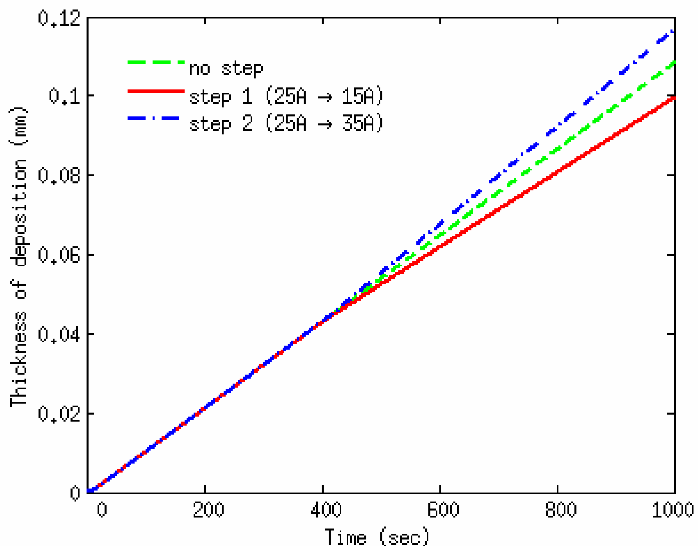

Figure 6.3. Response of thickness of coating with respect to step change in input current

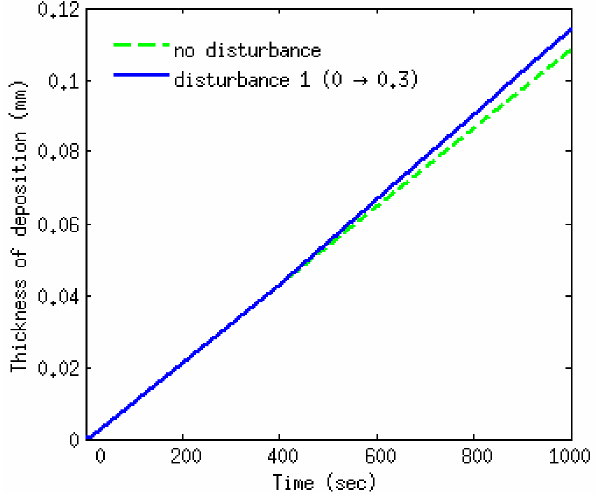

Figure 6.4. Response of thickness of coating with respect to step disturbance in the three variables of the EB-gun, A, V, and U_B

6.1.4. Design of feedback controller

An EB-PVD coater has physical limitations on the input current A:

$$A_{\min} \le A \le A_{\max} \tag{6.4}$$

where A_{min} is set to be 0A and A_{max} is set to be 65A.

The trajectory of the thickness of coating in the ideal situation is used to select a reference trajectory $\boldsymbol{G_d}$ in Fig. 6.1, which was produced when the input current A was set to be 25A. Two thickness set point is selected with the thickness of coating at t=600s. Figure 6.5 shows the reference trajectory with the thickness set points of 0.065mm at t=600s.

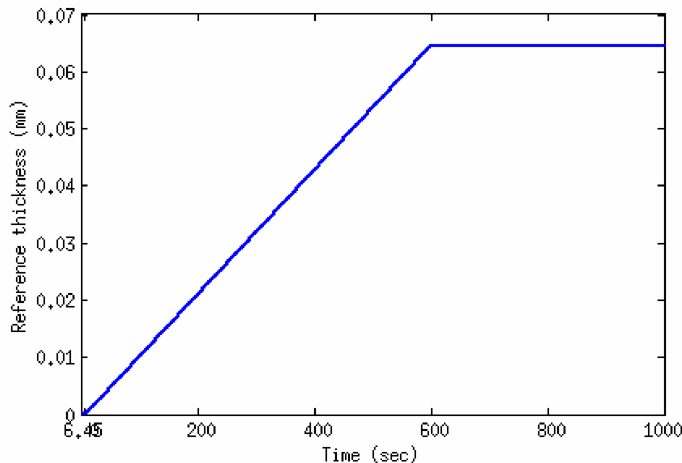

Figure 6.5. A reference trajectory with the thickness set-point of 0.0656mm at t=600s

The proportional-integral-derivative (PID) controller can be applied to this process control unless it destabilizes the system, results in a steady state error, or violates the physical constraints. The input current A, namely $\boldsymbol{u}$ in Fig. 6.1, is computed in the discrete form as follows:

$$u_{n+1} = u_n + \Delta u_n \tag{6.5}$$

$$\Delta u_n = K_o \cdot e_n + K_1 \cdot e_{n-1} + K_2 \cdot e_{n-2} \tag{6.6}$$

$$K_0 = K_p + K_i T + K_d / T$$
$$K_1 = -K_p - 2K_d / T \quad (6.7)$$
$$K_2 = K_d / T$$

where K_p is the controller proportionality gain, K_i is the integral controller gain, and K_d is the derivative controller gain.

The closed-loop EB-PVD process that employs the PID feedback controller has been simulated. The controller gains K_p, K_i, and K_d are set to be -176.68, -9.41, and -53.3162, respectively. The controller is activated at t=400s. The disturbance in the input current, input voltage and acceleration voltage (0.3) is introduced in the period from t=400s to t=500s.

Figure 6.6 shows the thickness of coating with the thickness set point of 0.0656mm at 600s. In the closed-loop deposition controlled by the PID controller, the thickness of coating has been controlled at the desired value. In some simulation run, a small steady state error in the thickness of coating was observed after the input current *A* became 0. It is obvious that when the overshoot occurs the closed-loop system can not be correct it because all gain parameters are same negative sign. To solve the overshoot problem, the stop criteria need to be added to the closed-loop process control scheme shown in Fig. 6.1.

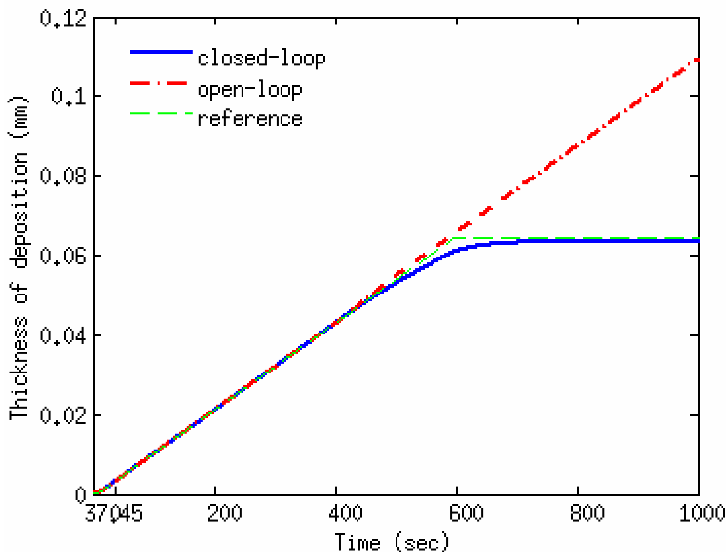

Figure 6.6. Thickness of coating with the thickness set point of 0.0656mm at 600s

6.2. Implementation of spatially distributed QCM sensors

The QCM read the change in crystal thickness (Δt) given by Eq. 3.27. These thicknesses of the deposition monitored by the QCMs become the output of the EB-PVD process ***G*** in Fig. 6.1. Since the attachment of a QCM to the surface of substrate is difficult, it prevents the direct measurement of the thickness of coating. Therefore, the transformation of the thickness measured by thickness to the thickness of coating needs to be studied. The inverse power function of source to substrate distance is of the following form (Fancey and Matthews, 1993)

$$t_f = ks^{-m} \tag{6.8}$$

where t_f is the coating thickness on a substrate surface positioned directly above and facing the source, s is the source to substrate distance, k is a constant, and m is the index in the range -2.1 to 3.6. Using this function, the thickness dso_i can be calculated as

follows.

$$dso_i = dso_{QCM}\left(\frac{z_i}{Z}\right)^m \tag{6.9}$$

Using the Schiller' model described by Fuke et al. (2005), the thickness ds_i can be calculated as follows.

$$ds_i = dso_i\left(1+\left(\frac{r_i}{z_i}\right)^2\right)^{-\frac{n+3}{2}} \tag{6.10}$$

With Eq. 6.8, the thickness dso_{QCM} can also be calculated from Δt measured with a QCM. The schematic description of this calculation is shown in Fig. 6.7.

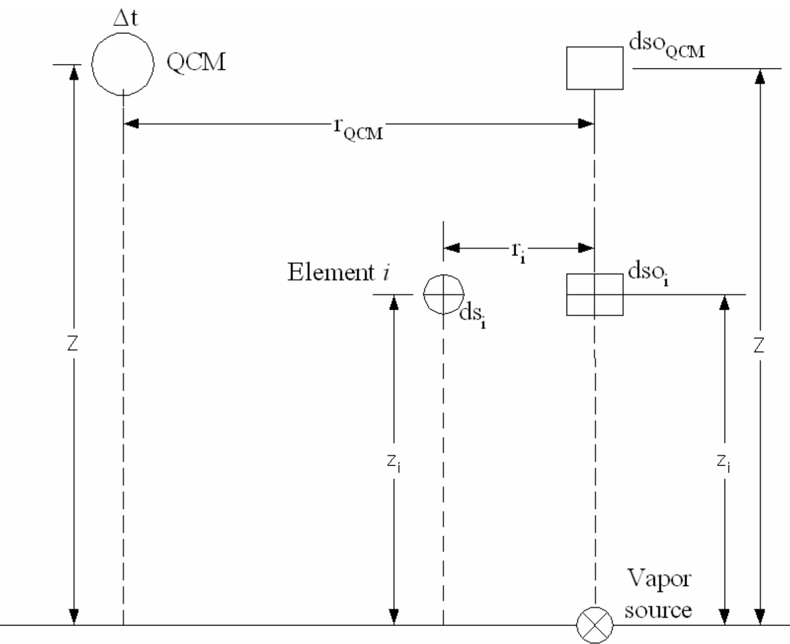

Figure 6.7. Schematic description of calculation of the deposition thickness ds_i from the thickness change in QCM

Now, from the in-situ thickness measurement from multiple QCMs installed inside the EB-PVD chamber, the thickness of coating at any point can be estimated.

6.3. Summary

The complicated EB-PVD process was simplified to the first-order process with integration using step-response modeling, which can be approximated as single-input-single-output (SISO) system. Based on the proposed metamodel, a closed-loop process control was applied to the EB-PVD process. The PID controller was chosen to correct the deviation of the thickness of coating from the reference trajectory. In the simulation experiments, there was observed small steady-state error so that the controller might be improved by continuously updating the controller gain parameters.

Chapter 7

Conclusion

This research has provided a unified dynamic computational model and digital simulation tool for the EB-PVD process. The unified model includes three dynamic models: machine dynamic model (MDM), substrate kinematics model (SKM), and deposition process model (DPM). First, MDM has been developed to predict the complex dynamics during the evaporation with reduced-ordered models. Second, SKM has been developed to efficiently compute the kinematics of substrate and manipulator motion. Third, three kinds of DPM have been developed to predict the coating thickness in two levels, macro-level in micrometers and micro-level in nanometers. The micro-level DPM based on level set method enables the estimation of the microstructure of a coating as well as the prediction of the coating thickness. Three dynamic models have been combined to construct the unified model that is implemented in Matlab to develop a digital simulation tool.

A MCDM technique has also been developed for collaborative EB-PVD process parameter optimization. The developed simulator has been used to design and simulate a real-time PID controller. Anticipated benefits of this research are the development of a scientific basis through reduced-order mathematical models and efficient computational models for controlling nanostructured coating processes using EB-PVD. This can be expected to lead to systematically engineered processes with high repeatability and low variance instead of the current “trial and error/ recipe-based methods” used in industry.

7.1. Summary of conclusions

In summary, the following conclusions have been drawn.

1. The unified dynamic computational model based on the proposed finite element models allows us to calculate the geometric distribution of vapor plume and to predict coating thickness and its distribution. The computational model is generic and can be used to simulate the EB-PVD process for any 3D shaped substrate.
2. The kinematic motion of a substrate was mathematically formulated, and a discrete state space model for the SKM was developed. The proposed SKM allows the analysis of the highly complex motion of substrate and help concurrent engineering for the design of holder. The matrix formation reduces the computational effort over 70% compared to the sequential formulation.
3. Generic insight from traditional deposition models has led to develop the speed function F of the EB-PVD process, which is critical to solve the level set equation. The level set method allows us to characterize the evolution of coating surface multi-level. Up to 50 nanometer level, the proposed model can characterize the surface evolution and columnar structure, which agrees well with published experimental results. The underlying partial differential equations of the level set method have been solved using numerical techniques for over ten hours on a cluster of 132 compute nodes of 2.4~2.6 GHz.

4. Selection of the best compromise solution based on collaboration of multiple decision makers has been pursued by MCDM algorithm that combines fuzz-logic approach with a continuous variable control approach to enable interactive optimization. The optimization problem for the EB-PVD has been developed as highly nonlinear programming. The simplified linear programming in the reduced parameter window has been solved to generate the efficient solution set. The selected decision variables with respect to the best global goal are expected to be the guide line for the future process planning to accelerate the product development.
5. The complicated EB-PVD process was simplified to the first-order process with integration using step-response modeling, which can be approximated as single-input-single-output (SISO) system. Based on the proposed metamodel, a PID controller was applied to the EB-PVD process to correct the deviation of the thickness of coating from the reference trajectory.

7.2. Future work

Based on the results obtained from this research, the recommendations for future work are as follows:

1. The level set method was developed using the ray-casting algorithm that only can check macro-shadowing effect. Thus, new line-of-sight inspecting algorithm can be expected to increase the resolution of the

simulation result in nano-level by inspecting micro-shadowing in the computation grid.

2. The deposition process model (DPM) was developed in two levels: macro-level in micrometers using the two traditional deposition models and micro-level in nanometers using the level set method. The macro-level DPM can produce consistent results of the entire region of surface. On the other hand, the micro-level DPM can produce comparable results of the local, interested region of surface. Therefore, it would be beneficial to combine those two DPMs in a multi-level simulation where coating thicknesses can be simultaneously predicted in both macro-level and micro-level.
3. The process parameter of the EB-PVD naturally interact each other. Thus, when one manipulated variable changes, it not only changes a corresponding controlled variable but also affects other controlled variables. Therefore, when the EB-PVD process is considered as multi-input-multi-output (MIMO), the real-time control of the EB-PVD process will be more successful.
4. Faster, parallel computing algorithm for optimization can be expected to realize the model predictive control using the proposed unified model because it can substantially improve computation ability. Moreover, the proposed unified model is also computationally efficient. Then, robust deposition control in nano-level can be achieved.

5. The experimental results from DOE will include the contribution by each main factor, the variance explained by the factors, and the interaction between the main factors. With statistical analysis, we can gain insights into the factors that have significant effect on the deposition process. Experimental results will also allow us to calibrate and tune the computational models, thereby improving the predictability of a digital simulator.

Bibliography

Adalsteinsson, D. and J. A. Sethian (1995a). "A Level Set Approach to a Unified Model for Etching, Deposition, and Lithography I: Algorithms and Two-Dimensional Simulations." Journal of computational physics **120**(1): 128-144.

Adalsteinsson, D. and J. A. Sethian (1995b). "A Level Set Approach to a Unified Model for Etching, Deposition, and Lithography II: Three-Dimensional Simulations." Journal of computational physics **122**(2): 348-366.

Anand, M. B., H. Shibata and M. Kakumu (1998). "Multiobjective optimization of VLSI interconnect parameters." IEEE transactions on computer-aided design of integrated circuits and systems **17**(12): 1252.

Anklam, T. M., L. V. Berzins, D. G. Braun, C. Haynam, T. Meier and M. A. McClelland (1995). "Evaporation rate and composition monitoring of electron beam physical vapor deposition process." Surface & coatings technology **76-77**(1-3 pt 2): 681-686.

Arenas Parra, M., A. Bilbao Terol and M. V. Rodriguez Uria (2001). "A fuzzy goal programming approach to portfolio selection." European journal of operational research **133**(2): 287-297.

Arthur, J. L. and A. Ravindran (1980). "PAGP, A Partitioning Algorithm for (Linear) Goal Programming Problems." ACM transactions on mathematical software **6**(3): 378-386.

Azad, F. H. (1998). "Dynamic model for simulation of heat transfer, vaporization, vapor transport, and deposition in EB-PVD process." Proceedings of the 1997 Thermal Barrier Coating Workshop: 157-169.

Bellman, R. and L. A. Zadeh (1970). "Decision making in a fuzzy environment." Management science **17**(4): 141-164.

Bernier, J. S., W. C. S. Weir, M. Fontecchio, R. D. Sisson Jr. and S. Bose (2002). Deposition rates of EB-PVD TBC's on cylindrical surfaces. 26th Annual Conference on Composites, Advanced Ceramics, Materials, and Structures: B, Cocoa Beach, FL, United States, American Ceramic Society.

Berzins, L. V., T. M. Anklam, F. Chambers, S. Galanti, C. A. Haynam and E. F. Worden (1995). "Diode laser absorption spectroscopy for process control - sensor system design methodology." Surface & coatings technology **76**(1): 675-680.

Bollinger, J. G. and N. A. Duffie (1988). Computer control of machines and processes. Reading, Mass., Addison-Wesley.

Bose, S. and J. DeMasi-Marcin (1997). "Thermal barrier coating experience in gas turbine engines at Pratt & Whitney." Journal of thermal spray technology **6**(1): 99-104.

Carvalho, S., E. Ribeiro, L. Rebouta, J. Pacaud, P. Goudeau, P. O. Renault, J. P. Riviere and C. J. Tavares (2003). "PVD grown (Ti,Si,Al)N nanocomposite coatings and (Ti,Al)N/(Ti,Si)N multilayers: Structural and mechanical properties." Surface & coatings technology **172**(2-3): 109-116.

Chase, M. W. (1986). JANAF thermochemical tables. New York, NY, American Chemical Society and the American Institute of Physics for the National Bureau of Standards.

Cho, S., I. Fuke and V. Prabhu (2005a). "Motion Planning for Coating Process Optimization in Electron Beam Physical Vapor Deposition." Surface Engineering **21**(4): 279-289.

Cho, S., S. Lewis, V. Prabhu and I. Fuke (2005b). "Intelligent automation of electron beam physical vapour deposition." Surface Engineering **21**(1): 17-26.

Chung, Y.-W. and W. D. Sproul (2003). "Superhard coating materials." MRS bulletin **28**(3): 164-168.

Coronell, D. G., E. W. Egan, G. Hamilton, A. Jain, R. Venkatraman and B. Weitzman (1998). "Monte Carlo simulations of sputter deposition and step coverage of thin films." Thin solid films **333**(1): 77-81.

Craig, J. J. (1989). Introduction to Robotics: Mechanics and Control. Reading, MA, Addison-Wesley Publishing Company.

Dave, V. R., J. E. Matz, T. W. Eagar and D. L. Goodman (1995). High energy electron beam (HEEB)-solid interaction model for EB deposition and shock processing. 2nd International Conference on Beam Processing of Advanced Materials, Cleveland, Ohio; USA.

Fancey, K. S. and A. Matthews (1993). "Coating thickness fall-off with source to substrate distance in PVD processes." Surface & coatings technology **59**(1): 113-116.

Ferris, M. C. (1998). MATLAB and GAMS: Interfacing Optimization and Visualization Software. Mathematical Programming Technical Report 98-19. Madison, Computer Sciences Department, University of Wisconsin**:** 1-20.

Fuke, I., V. Prabhu and S. Baek (2005). "Computational Models for Predicting Coating Thickness in Electron Beam Physical Vapor Deposition." Journal of Manufacturing Processes **7**(2): 140-152.

Gallivan, M. A. and R. M. Murray (2004). "Reduction and identification methods for Markovian control systems, with application to thin film deposition." International journal of robust and nonlinear control **14**(2): 113-132.

Gell, M. (1995a). "Application opportunities for nanostructured materials and coatings." Materials Science and Engineering A **204**: 246-251.

Gell, M. (1995b). Potential for nanostructured materials in gas turbine engines. Proceedings of the 2nd International Conference on Nanostructured Materials, Stuttgart, Ger, Pergamon Press Inc, Tarrytown, NY, USA.

Geoffrion, A. M. (1967a). "Strictly Concave Parametric Programming, Part I: Basic Theory." Management Science **13**(3): 244-253.

Geoffrion, A. M. (1967b). "Strictly Concave Parametric Programming, Part II: Additional Theory and Computational Considerations." Management Science **13**(5): 359-370.

Glang, R. (1970). Evaporation Theory. Handbook of Thin Film Technology. L. I. Maissel and R. Glang, McGraw-Hill, Inc.**:** 26-36.

Gleiter, H. (1992). "Materials with ultrafine microstructures: retrospectives and perspectives." Nanostructured materials **1**(1): 1.

Gower-Hall, A. E., D. S. Boning, P. Rosenthal and A. Waldhauer (2002). "Model-based uniformity control for epitaxial silicon deposition." Semiconductor Manufacturing, IEEE Transactions on **15**(3): 295-309.

Graper, E. B. (1973). "Distribution and Apparent Source Geometry of Electron-Beam-Heated Evaporation Sources." Journal of vacuum science and technology **10**(1): 100-103.

Gyugyi, P. J., Y. M. Cho, G. Franklin, T. Kailath and R. H. Roy (1992). Model-based control of rapid thermal processing systems. First IEEE Conference on Control Applications (Cat.No.92CH3000-7), Dayton, OH, USA, IEEE.

Halnan, W. K. and D. Lee (1983). Electron beam physical vapor deposition process for coating gas turbine airfoils. High-Temperature Protective Coatings. Proceedings of a Symposium held at the 112th AIME Annual Meeting, Atlanta, Ga, USA, Metallurgical Soc of AIME, Warrendale, Pa, USA.

Hansen, U., S. Rodgers and K. F. Jensen (2000). "Modeling of metal thin film growth: Linking angstrom-scale molecular dynamics results to micron-scale film topographies." Physical review **62**(4): 2869-2878.

Hass, D. D. (2000). Directed Vapor Deposition of Thermal Barrier Coatings. Materials Science and Engineering, University of Virginia. **Doctor of Philosophy:** 281.

Hawkeye, M. and M. Brett (2005). "Optical Nanostructures Fabricated with Glancing Angle Deposition." Vacuum Technology & Coating(November): 46-53.

Hill, R. J., Ed. (1986). Physical vapor deposition. Berkeley, Calif., Airco Temescal.

Ho, W. K., L. L. Lee, A. Tay and C. Schaper (2002). "Resist film uniformity in the microlithography process." IEEE transactions on semiconductor manufacturing **15**(3): 323-330.

Ho, W. K., A. Tay, L. L. Lee and C. D. Schaper (2004). "On control of resist film uniformity in the microlithography process." Control engineering practice **12**(7): 881-889.

Holubar, P., M. Jilek and M. Sima (2000). "Present and possible future applications of superhard nanocomposite coatings." Surface and Coatings Technology **133-134**: 145-151.

http://www.electro-optical.com. "Material Emissivity Properties." from http://www.electro-optical.com/bb_rad/emissivity/matlemisivty.htm.

Ikonen, E. and K. Najim (2001). "Non-linear process modelling based on a Wiener approach." Proceedings of the Institution of Mechanical Engineers. Part I, Journal of systems and control engineering **215**(1): 15.

Jang, B.-K., M. Yoshiya and H. Matsubara (2005). "Influence of number of layers on thermal properties of nano-structured zirconia film fabricated by EB-PVD method." Nippon Kinzoku Gakkaishi **69**(1): 56-60.

Jang, B. K. and H. Matsubara (2005). "Influence of rotation speed on microstructure and thermal conductivity of nano-porous zirconia layers fabricated by EB-PVD." Scripta materialia **52**(7): 553-558.

Johnson, R. A. and D. W. Wichern (2002). Applied Multivariate Statistical Analysis. Upper Saddle River, N.J., Prentice Hall.

Jones, J. G. and A. A. Voevodin (2004). "Magnetron sputter pulsed laser deposition: technique and process control developments." Surface & coatings technology **184**(1): 1-5.

Junker, S. T., R. W. Birkmire and F. J. Doyle (2004). "Manufacture of Thin-Film Solar Cells: Modeling and Control of $Cu(InGa)Se_2$ Physical Vapor Deposition onto a Moving Substrate." Industrial & engineering chemistry research **43**(2): 566-576.

Koomsap, P. (2001). Intelligent control of laser-based manufacturing processes and systems. Industrial engineering. University Park, PA, USA, Penn State. **Ph.D:** 168.

Koopmans, T. C. (1951). Activity analysis of production and allocation: proceeding of a conference. New York, NY, Wiley.

Langmuir, I. (1913). "The Vapor Pressure of Metallic Tungsten." Physical Review **2**(5): 329–342.

Lewis, A. S., S. D. Brown and R. L. Tutwiler (2000). "Unified control approach for an electron beam physical vapour deposition process." International journal of robotics & automation **15**(3): 145-151.

Li, Q. and O. A. Palusinski (2003). "Application of multiobjective optimization in selection of printed wiring boards." IEEE transactions on advanced packaging **26**(4): 425-432.

Lin, C.-C. (2004). "A weighted max-min model for fuzzy goal programming." Fuzzy sets and systems **142**(3): 407-420.

Lugscheider, E., C. Barimani and G. Dopper (1998). "Ceramic thermal barrier coatings deposited with the electron beam-physical vapour deposition technique." Surface & coatings technology **98**(1): 1221-1227.

Mahan, J. E. (2000). Physical vapor deposition of thin films, John Wiley & Sons, Inc.

Mahapatra, N. K. and M. Maiti (2005). "Decision process for multiobjective, multi-item production-inventory system via interactive fuzzy satisficing technique." Computers & mathematics with applications **49**(5-6): 805-821.

Maissel, L. I. and R. Glang, Eds. (1970). Handbook of Thin Film Technology, McGraw-Hill, Inc.

Malakooti, B. and A. Ravindran (1985). "Experiments with an interactive paired comparison simplex method for molp problems." Annals of operations research **5**(6): 575-597.

Matsumoto, M., N. Yamaguchi and H. Matsubara (2004). "Low thermal conductivity and high temperature stability of ZrO_2-Y_2O_3-La_2O_3 coatings produced by electron beam PVD." Scripta materialia **50**(6): 867-871.

Munz, W.-D. (2003). "Large-scale manufacturing of nanoscale multilayered hard coatings deposited by cathodic arc/unbalanced magnetron sputtering." MRS bulletin **28**(3): 173-179.

Narasimhan, R. (1980). "Goal programming in a fuzzy environment." Decision sciences **11**(2): 325-336.

Nastac, L., F. R. Dax and W. Hanusiak (2004). "Methodology for modeling the EB-PVD coating process." J. Phys. IV France **120**: 307-314.

Ni, D. and P. D. Christofides (2005). "Multivariable Predictive Control of Thin Film Deposition Using a Stochastic PDE Model." Industrial & engineering chemistry research **44**(8): 2416-2427.

Norquay, S. J., A. Palazoglu and J. A. Romagnoli (1998). "Model predictive control based on Wiener models." Chemical engineering science **53**(1): 75-84.

NRC (1996). Coatings for High-Temperature Structural Materials: Trends and Opportunities. Washington, D.C., National Academy Press.

Osher, S. and J. A. Sethian (1988). "Fronts propagating with curvature-dependent speed: Algorithms based on Hamilton-Jacobi formulations." Journal of computational physics **79**(1): 12-49.

Powell, A., P. Minson, G. TRAPAGA and U. PAL (2001). "Mathematical Modeling of Vapor-Plume Focusing in Electron-Beam Evaporation." Metallurgical And Materials Transactions A **32A**.

Prabhu, V. V. (1995). Real-time distributed arrival time control of heterarchical manufacturing systems. Mechanical engineering. Wisconsin, US, The University of Wisconsin - Madison. **Ph.D.:** 123.

Pulker, H. K. (1984). Coatings on Glass. New York, Elsevier.

Qin, Y., C. Dong, X. Wang, S. Hao, A. Wu, J. Zou and Y. Liu (2003). "Temperature profile and crater formation induced in high-current pulsed electron beam processing." Journal of vacuum science & technology. A, An international journal devoted to vacuum, surfaces, and films **21**(6): 1934-1938.

Ravindran, A., D. T. Phillips and J. J. Solberg. (1987). Operations research: principles and practice. New York, Wiley.

Renaud, G., M. Ducruet, O. Ulrich and R. Lazzari (2004). "Apparatus for real time in situ quantitative studies of growing nanoparticles by grazing incidence small angle X-ray scattering and surface differential reflectance spectroscopy." Nuclear instruments & methods in physics research. Section B, Beam interactions with materials and atoms **222**(3): 667-680.

Rigney, D. V., R. Viguie, D. J. Wortman and D. W. Skelly (1997). "PVD thermal barrier coating applications and process development for aircraft engines." Journal of thermal spray technology **6**(2): 167-175.

Roco, M. C., R. S. Williams and P. A. Dordrecht, Eds. (2000). Nanotechnology Research Directions. Boston, Kluwer Academic Publishers.

Sakawa, M., H. Yano and T. Yumine (1987). "An interactive fuzzy satisficing method for multiobjective linear-programming problems and its application." IEEE transactions on systems, man, and cybernetics **17**(4): 654-661.

Schiller, S., U. Heisig and S. Panzer (1982). Electron beam technology. New York, John Wiley & Sons.

Schulz, U., K. Fritscher, H. J. Ratzer-Scheibe, W. A. Kaysser and M. Peters (1997). "Thermocyclic Behaviour of Microstaructurally Modified EB-PVD Thermal Barrier Coatings." Materials Science Forum **251-254**: 957-964.

Schulz, U., J. Munzer and U. Kaden (2002). Influence of deposition conditions on density and microstructure of EB-PVD TBCs. 26th Annual Conference on Composites, Advanced Ceramics, Materials, and Structures: B, Cocoa Beach, FL, United States, American Ceramic Society.

Schulz, U., S. G. Terry and C. G. Levi (2003). "Microstructure and texture of EB-PVD TBCs grown under different rotation modes." Materials Science and Engineering A: 1-11.

Sethian, J. A. (1999). Level set methods and fast marching methods: evolving interfaces in computational geometry, fluid mechanics, computer vision, and materials science. Cambridge, New York, Cambridge University Press.

Sethian, J. A. and J. Strain (1992). "Crystal growth and dendritic solidification." Journal of computational physics **98**(2): 231-253.

Shackelford, J. F. and W. Alexander (2001). CRC materials science and engineering handbook. Boca Raton, FL, CRC Press.

Shi, L. P., X. D. He and Y. Li (2004). "Theory deposition model and influencing factors during process of preparing micro-layer laminate by EBPVD." ACTA METALLURGICA SINICA **17**(3): 283-287.

Shin, W. S. and A. Ravindran (1991). "Interactive multiple objective optimization: survey. I. Continuous case." Computers & operations research **18**(1): 97-114.

Simon, D. and U. Pal (1999). "Mathematical modeling of a melt pool driven by an electron beam." Metallurgical and materials transactions. B, Process metallurgy and materials processing science **30**(3): 515-525.

Singh, J. and D. E. Wolfe (2003). "Nano-grained net-shaped fabrication of Re components by EB-PVD." Materials and manufacturing processes **18**(6): 915-927.

Singh, J. and D. E. Wolfe (2005). "Nano and macro-structured component fabrication by electron beam-physical vapor deposition (EB-PVD)." Journal of materials science **40**(1): 1-26.

Singh, J. J. (1996). "Ion-beam assisted, electron-beam physical vapor deposition." Advanced materials & processes **150**(6): 27-28.

Smith, G. D. (1985). Numerical solution of partial differential equations: finite difference methods. New York, Oxford University Press.

Suryanarayana, C. (1995). "Nanocrystalline materials." International materials reviews **40**(2): 41-64.

Terry, S. G. (2001). Evolution of microstructure during the growth of thermal barrier coatings by electron-beam physical vapor deposition. Material Department. Santa Barbara, University of California, Santa Barbara. **Ph.D:** 197.

Touloukian, Y. S. (1970-79). Thermophysical properties of matter. New York, NY, IFI/Plenum.

Vancheeswaran, R., D. G. Meyer and H. N. G. Wadley (1997). "Optimizing the consolidation of titanium matrix composites." Acta materialia **45**(10): 4001-4018.

Wark, K. (1966). Thermodynamics, McGraw-Hill, Inc.

Wolfe, D. E. (2001). Synthesis and characterization of TiC, TiBCN, TiB2/TiC and TiC/CrC Multilayer coatings by reactive and ion beam assisted, electron beam-physical vapor deposition (EB-PVD). Materials Science and Engineering. University Park, The Pennsylvania State University. **Doctor of Philosophy:** 270.

Wolfe, D. E., M. B. Movchan and J. Singh (1996). Architechture of functionally graded ceramic/metallic coatings by electron beam-physical vapor deposition. the Annual

Meeting of the Minerals, Metals & Materials Society, Orlando, FL, USA, TMS, Warrendale, PA, USA.

Wolfe, D. E. and J. Singh (1999). "Microstructural evolution of titanium nitride (TiN) coatings produced by reactive ion beam-assisted, electron beam physical vapor deposition (RIBA, EB-PVD)." JOURNAL OF MATERIALS SCIENCE **34**: 2997-3006.

Yamaguchi, N., K. Wada, K. Kimura and H. Matsubara (2003). "Microstructure modification of yttria-stabilized zirconia layers prepared by EB-PVD." Journal of the Ceramic Society of Japan **111**(1300): 883-889.

Yoshida, T. (2004). NEDO Nano Coating Project: Outline and Achievements. International Conference on MEMS, NANO and Smart Systems (ICMENS'04), IEEE.

Zionts, S. and J. Wallenius (1976). "An interactive programming method for solving the multiple criteria problem." Management science **22**(6): 652-663.

VITA

Seungyup Baek

Seungyup Baek was born in Korea in 1970. He received his B.S. and M.S. degree at Seoul National University, Korea, in 1993 and 1995, respectively, both in metallurgical engineering. During his M.S. study his major research interest was in the area of alloy design, especially aluminum casting alloy. After he finished his M.S. study, he joined Institute of Advanced Engineering (IAE), Yongin, Korea. For six years in Production System Laboratory of IAE, he mostly worked in the development of environment-friendly vehicle for next generation. Then, he moved to GM Daewoo Motor Co. (GMDW), Incheon, Korea. For two years in Production technology Laboratory of GMDW, he mostly worked in the area of information strategic planning (ISP) and engineering data management (EDM). In 2003 Fall, he enrolled in the Ph.D. program in Industrial Engineering at the Pennsylvania State University. During his Ph.D. study he was employed as a research assistant in the Department of Industrial Engineering under the supervision of Dr. Vittaldas Prabhu. His current primary research interest is in the area of *direct digital manufacturing* in the context of nanotechnology using mathematical and computational models and *multi-criteria decision making* in the context of complex systems using optimization heuristics.